Towards MRI-guided radiotherapy for pediatric patients with abdominal tumors

Filipa Guerreiro

Towards MRI-guided radiotherapy for pediatric patients with abdominal tumors

Filipa Borges Ferreira Guerreiro

Cover description
"The girl with the balloon" designed by Francisco Fernandes. The cover idea was based upon the difference of the low imaging contrast (CT / CBCT) provided by conventional radiotherapy treatments (represented by the girl under the darkness on the back cover) and the high imaging contrast provided by MRI-guided radiotherapy treatments (shown by the girl under the sun on the cover of the thesis).

Towards MRI-guided radiotherapy for pediatric patients with abdominal tumors
PhD Thesis, Utrecht University, The Netherlands

Filipa Borges Ferreira Guerreiro, 2019

Manuscript:
Layout: F. Guerreiro
Typesetting: LaTeX 2_ε
Printed by: ProefschriftMaken
ISBN: 978-90-393-7181-7

Copyright:
© F. Guerreiro
© Taylor & Francis (Chapter 2 and 3)
© Elsevier (Chapter 4)
© IOP Publishing Ltd (Chapter 5)

Financial support for publication of this thesis was kindly provided by RaySearch Laboratories and Elekta.

Towards MRI-guided radiotherapy for pediatric patients with abdominal tumors

Op weg naar MRI-geleide radiotherapie voor pediatrische patiënten met abdominale tumoren

(met een samenvatting in het Nederlands)

Proefschrift

ter verkrijging van de graad van doctor aan de
Universiteit Utrecht
op gezag van de rector magnificus, Prof. dr. H.R.B.M. Kummeling,
ingevolge het besluit van het college voor promoties
in het openbaar te verdedigen
op vrijdag 8 november 2019 des middags te 2.30 uur

door

Filipa Borges Ferreira Guerreiro

geboren op 23 juni 1992
te Lissabon, Portugal

Promotor:	Prof. dr. B.W. Raaymakers
Copromotoren:	Dr. E. Seravalli Dr. G.O. Janssens

First, think.
Second, dream.
Third, believe.
And finally, dare.

Walt Disney

Contents

1	Introduction	11
2	Intra- and inter-fraction uncertainties during IGRT for Wilms' tumor	23
3	Potential benefit of MRI-guided IMRT for flank irradiation in pediatric patients with Wilms' tumor	39
4	Evaluating the benefit of PBS vs. VMAT dose distributions in terms of dosimetric sparing and robustness against inter-fraction anatomical changes for pediatric abdominal tumors	57
5	Feasibility of MRI-only photon and proton dose calculations for pediatric patients with abdominal tumors	73
6	Discussion	95
7	Summary	113
8	Samenvatting	117
Bibliography		121
Publications		137
Acknowledgements		139
Curriculum Vitae		143

Acronyms

3D Three-Dimensional
4D Four-Dimensional
4D-CT Four-Dimensional Computed Tomography
AP Anterior-Posterior
CBCT Cone-beam Computed Tomography
CC Craniocaudal
CT Computed Tomography
CTV Clinical Target Volume
DVH Dose-Volume Histogram
GTV Gross Tumor Volume
HU Hounsfield Unit
IGRT Image-Guided Radiation Therapy
IMPT Intensity-Modulated Proton Therapy
IMRT Intensity-Modulated Radiation Therapy
ITV Internal Target Volume
LR Left-Right
Linac Linear accelerator
MC Monte Carlo
MRI Magnetic Resonance Imaging
MV MegaVoltage
NBL Neuroblastoma
NT Normal Tissue
OAR Organ At Risk
PBS Pencil Beam Scanning
PTV Planning Target Volume
RT Radiation Therapy
sCT synthetic Computed Tomography
SPR Stopping Power Ratio
TB Tumor Bed
VMAT Volumetric Modulated Arc Therapy
WT Wilms' Tumor

CHAPTER 1

Introduction

1.1 Abdominal cancer in children

Cancer is a leading cause of death in children and approximately 300 000 children aged up to 18 years old are annually diagnosed with cancer in the world (Steliarova-Foucher et al., 2017). Differently to cancer in adults, pediatric tumors are mainly developed by early mutations or through the presence of genetic predisposition and not commonly due to lifestyle-related causes (Spector et al., 2015). The most common types of childhood cancers include hematological (i.e leukemia, lymphoma), brain and solid tumors (i.e Wilms' tumor (WT), neuroblastoma (NBL)).

WT and NBL belong to the most frequent abdominal tumors in pediatric patients (Maris et al., 2007; Brok et al., 2016). WT is a malignancy of the kidney while NBL most frequently starts in the adrenal and retroperitoneal regions but can also occur in the thorax, pelvis and neck regions. Due to the use of a multimodality treatment comprising surgery, chemotherapy and radiotherapy, the survival rates for these patients have increased over the past few decades up to 90% for WT and 60% for NBL (Pritchard-Jones et al., 2015; Ladenstein et al., 2017).

In the Netherlands, around 550 children are diagnosed with cancer per year and approximately one-third of them ($\sim$ 200 patients) receive radiotherapy treatment. In the sub-group of patients that receive radiotherapy, 7% of the cases are hematological cancer, 44% brain tumors and 49% solid tumors (institutional data).

1.2 Radiotherapy concept

Radiotherapy, also known as radiation therapy (RT), involves the use of ionizing radiation to damage and ultimately kill malignant tumor cells. The main goal is to deliver high radiation dose levels to the tumor volume while keeping the dose to the normal tissue (NT) as low as possible (Khan and Gibbons, 2014). To allow for the NT to recover from the radiation dose, radiotherapy treatments are commonly delivered in several fractions (fractionation).

The use of radiotherapy has been reported to improve the survival rates of several childhood cancers (Jereb et al., 1994; Gillis et al., 2007; O'Leary et al., 2008). Nevertheless, the sub-group of patients that receive radiotherapy is at increased risk of developing NT toxicity and secondary malignancies (Oeffinger et al., 2006; Robinson and Hudson, 2014). For WT and NBL patients, renal failure, scoliosis and metabolic syndrome are three of the most frequent radiation-induced complications (Rate et al., 1991; Ritchey et al., 1996; Sasso et al., 2010; van Waas et al., 2012). As children are reported to be more sensitive to radiation than adults (Hall and Phil, 2006), delivering adequate target dose levels during radiotherapy treatment is as important as sparing the long-term functions of the adjacent organs at risk (OARs).

During treatment, the ionizing radiation can be delivered by different means. In brachytherapy, the radiation source is placed inside the body near or in the tumor itself. In external beam radiotherapy, the radiation initiates from a source outside of the patient body by the use of photon X-rays or charged particles (i.e protons) (*Figure 1.1*).

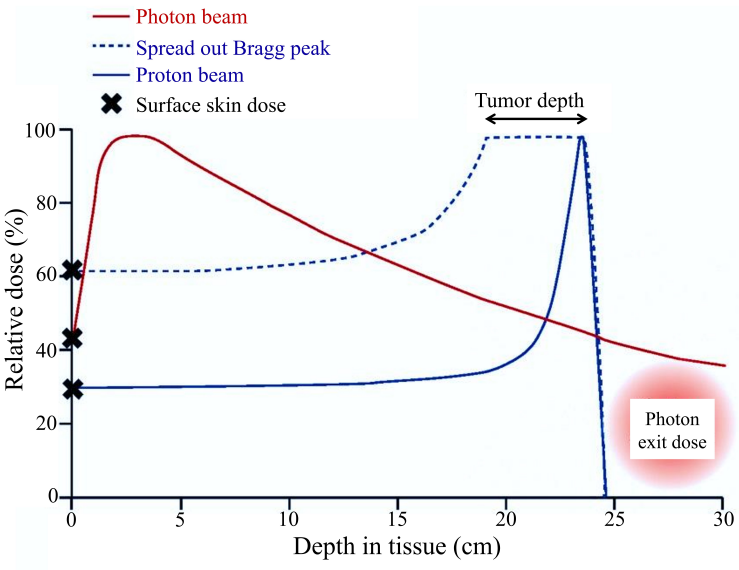

Figure 1.1 Percentage dose-depth profile for a photon (red) and a proton (blue) beam [adapted from (Leeman et al., 2017)].

1.2.1 Photon therapy

Currently, radiotherapy is mainly delivered by megavoltage (MV) X-rays generated by a linear accelerator (linac) (Thwaites and Tuohy, 2006). X-rays are high-energy photons produced by electron energy transitions between atomic shells. As photons have no mass, they present lower chances of interaction with matter compared to charged particles (Nickoloff, 2015). A photon beam propagating through air is governed by the

inverse square law: the photon energy is inversely proportional to the square of the distance away from the radiation source (Podgorsak, 2005). A photon beam propagating through matter is not only affected by the inverse square law but also by the attenuation and scattering processes occurring along the beam path. Within the clinical photon energy range (6 - 20 MV), the Compton Effect is the most predominant photon-matter interaction (Podgorsak, 2005). In this process, a photon collides with an orbiting electron, thus not tightly bound to an atom, resulting in the scattering of both photon and secondary electron particles. The generated secondary electrons are responsible for the dose deposition in the patient. From the relatively large amount of secondary electrons that are first released, a dose buildup region is formed (Podgorsak, 2005). After this dose buildup, the photon radiation shows an exponential decay of energy deposition with increasing depth in the tissue as a result of the beam attenuation (*Figure 1.1*).

1.2.1.1 Treatment preparation

During treatment preparation, a computed tomography (CT) image is acquired with the patient in treatment position (Hsieh et al., 2015). A radiation oncologist is responsible to delineate the gross tumor volume (GTV) together with the surrounding OARs. To guarantee target coverage and OARs sparing, safety margins are employed to compensate for uncertainties related to the location of these structures during treatment. Regarding the target, the GTV is expanded to a clinical target volume (CTV) to include the volume of suspected microscopic disease (Podgorsak, 2005). Depending on the tumor location, an internal target volume (ITV) can be defined around the CTV to account for the patient breathing motion.

During treatment preparation and / or delivery, geometric inaccuracies and intra- and inter-fraction uncertainties can lead to the occurrence of systematic and random errors that will reduce the overall treatment accuracy (van Herk et al., 2000; van Herk, 2004). There are three main sources of uncertainty that contribute to the generation of these errors: (1) delineation (systematic), (2) motion (systematic and random) and (3) patient set-up (systematic and random) uncertainties. Delineation uncertainties are caused by inter-observer variability and by differences between imaging modalities (i.e soft-tissue contrast, image resolution). Motion uncertainties arise from displacements of the target and OARs either caused by breathing (intra-fraction) or by day-to-day variations (inter-fraction). Patient set-up uncertainties result from patient positioning differences during treatment delivery (intra-fraction) or in between days (inter-fraction). To account for these systematic and random errors and to prevent that the target coverage is not maintained throughout the treatment, a safety margin is used around the CTV or ITV to create the planning target volume (PTV) (van Herk et al., 2000). Subsequently, the planning-CT, the PTV and OARs contours are imported to the treatment planning system (TPS) to optimize the RT plan.

The photon dose distribution is calculated making sure that the prescribed dose is delivered to the PTV while the doses to the OARs are within clinical tolerances. Computation of the dose is possible due to the Hounsfield unit (HU) conversion to electron density values extracted from the planning-CT (Chernak et al., 1975).

1.2.1.2 Treatment delivery

After optimization, the RT plan is transferred to the linac to be delivered to the patient in multiple fractions. Nowadays, the linac is equipped with a multileaf collimator (MLC), attached to the linac head, capable of blocking radiation with multiple pairs of individual moving leaves. Photon delivery is mostly done by using three-dimensional conformal RT (3D-CRT), intensity-modulated RT (IMRT) or volumetric modulated arc therapy (VMAT).

In 3D-CRT, all beams parameters (i.e number, direction, weights) are specified manually by the treatment planner by means of trial and error (Zelefskya et al., 1998). Thus, an individual weight is optimized per beam by using fixed MLC shapes. The inability to exclude a sufficient NT volume from the target dose region presents a limitation of this technique. With the use of more advanced photon delivery techniques, such as IMRT and VMAT, conformal dose gradients can be delivered to complex target volumes enabling the reduction of the NT volume irradiated at target dose levels.

With IMRT, the intensity of each photon radiation field is allowed to vary by using multiple MLC shapes per beam (Bortfeld, 2006). This is possible by generating the IMRT plan using an inverse optimization that automatically adjusts the MLC shapes and the beams weights according to the target and OARs objectives / constraints. While with IMRT, beams are delivered using multiple fixed gantry angles with VMAT, radiation is delivered in a single or multiple arcs using a 360° rotating gantry (Otto, 2008). Compared to IMRT, arching the gantry around the patient (1) enables performing dose delivery in all directions and in a shorter treatment time and (2) allows for an improvement in dose conformity and NT sparing.

1.2.2 Proton therapy

The advantages of proton compared to photon therapy were first outlined by (Wilson, 1946). Although with IMRT and VMAT more conformal photon dose distributions can nowadays be achieved, the physics of photons make it impossible to avoid the exit dose downstream from the target (*Figure 1.1*), which is considered the main limitation of photon therapy.

Compared to photons, protons are heavy and positively charged particles that deposit small amounts of energy when travelling through the tissue (Paganetti, 2012). Their energy loss is governed by the *Bethe-Bloch* equation which gives the charged particles stopping power (SP) per unit length (Bethe, 1930; Bloch, 1933). Unlike photons, protons travel a finite range in the patient body proportional to their initial energy. Depending

on their energy, protons interact with the matter through Coulomb interactions with the atomic electrons and / or nucleus, nuclear reactions and Bremsstrahlung (Newhauser and Zhang, 2015). At clinical proton beam energies (70 - 250 MV), protons mostly experience inelastic Coulomb interactions with the orbiting atomic electrons (Lomax, 2009). In this interaction, an atomic excitation or ionization and a small trajectory deflection of the incident proton particle occur. While setting free the orbiting electrons, these secondary particles will go on ionizing other neighboring atoms (Lomax, 2009). During this process, as the mass of a proton is much higher than the mass of an electron, protons lose small amounts of energy and start to slow down, depositing the bulk of their energy at the very end of their path, the so-called Bragg peak (Newhauser and Zhang, 2015). For this reason, tissues beyond the proton range are not irradiated (*Figure 1.1*). The proton range is commonly defined as the 80% distal dose point of the Bragg peak where 50% of the protons have stopped (Paganetti, 2012).

1.2.2.1 Treatment preparation

Similarly to photon therapy, during proton therapy a planning-CT is acquired for each patient. Nevertheless, due to the significant differences in photon and proton dose deposition (*Figure 1.1*), many of the treatment planning techniques used in photon therapy (i.e PTV-based RT plan optimization) are not extensible to protons (Mohan and Grosshans, 2017). In proton therapy, SP ratios (SPRs) relative to water are derived from the planning-CT to estimate the Bragg peak position in the patient. Thus, accurate SPRs determination is essential for the proton beam range computation and consequently for precise RT dose calculation. Proton range computation is however uncertain mainly due to (1) the conversion of the planning-CT HUs to SPRs and (2) the large dependence of the proton range on the patient anatomy.

The conversion between HUs and SPRs (1) is usually performed by applying a calibration curve, referred to as a Hounsfield Look-Up-Table (HLUT). The most popular method of determining the HLUT is the stoichiometric calibration method developed by (Schneider et al., 1996). Nonetheless, this methodology was proven to be strongly dependent on the CT scanner, on the CT reconstruction parameters and on the specific HLUT definition details (Taasti et al., 2018). In literature, the range uncertainty introduced by the estimation of SPRs derived from a single CT and calibration curve was reported to be up to 3.5% (Moyers et al., 2009). More recently, dual energy x-ray CT (DECT) has been introduced in clinic for a more accurate SPRs estimation. (Yang et al., 2010) demonstrated that by obtaining photon attenuation coefficients from two different x-ray spectra, the electron density and the effective atomic number of human tissues could be calculated and further used for an accurate SPRs estimation. In addition, the proton finite range and sharp distal dose fall-off make proton dose distributions highly sensitive to differences in CT densities along the beam direction (i.e patient intra- and inter-fraction anatomical variations) (2). These potential differences can severely impact the delivered dose as changes in the proton path length result in displacements of the Bragg peak location (Lomax, 2008a,b).

Range uncertainties generated by either (1) or (2) do not only cause an under-dosage at the target edge but lead to the occurrence of both hot and cold spots inside and outside the target volume (Unkelbach and Paganetti, 2018). Consequently, the conventional photon practice of assigning CTV-to-PTV margins is not enough to compensate for these effects (Lomax, 2008b; Albertini et al., 2011; Liu et al., 2012; Unkelback and Paganetti, 2018). Robust proton treatment planning is currently used to mitigate the effect of both range and set-up uncertainties (Unkelbach et al., 2007; Fredriksson et al., 2011; Unkelbach and Paganetti, 2018). During robust proton RT plan optimization, set-up uncertainties are modeled by making translational shifts of the RT plan isocenter and range uncertainties by scaling the planning-CT density.

1.2.2.2 Treatment delivery

During treatment delivery, proton beams are generated using a cyclotron (Schillo et al., 2001) or a synchrotron (Smith et al., 2009). After acceleration, the proton beam is guided through the beam line until the treatment gantry and delivered to the patient either using passive scattering (PS) or pencil beam scanning (PBS).

In PS, a proton beam is scattered over a larger area to adequately cover the entire target volume using patient-specific beam modifying devices (i.e range modulators). In PBS or spot scanning, each proton beam is divided into thin beamlets that are magnetically scanned to confine the beamlets Bragg peaks, commonly named as spots, within the target volume (Paganetti, 2012). Radiation dose is deposited layer-by-layer by modulating the energy and weights of the different spots which are combined to get the desired target coverage (Trofimov and Bortfeld, 2003). Two main optimization methods are used to select the spots position, energy and weight: single field uniform dose (SFUD) and multi field uniform dose (MFUD). In SFUD, the spots of each proton beam are optimized individually. In MFUD, usually referred to as intensity-modulated proton therapy (IMPT) (Lomax et al., 1999), spots from all proton beams are optimized together resulting in highly inhomogeneous dose distributions per beam. Ultimately, the doses from each beam are summed up to create the desired target dose. Compared to SFUD, a better NT sparing can be achieved with MFUD due to the higher level of beam modulation (Lomax et al., 2001; Quan et al., 2013). Nevertheless, owing to its large dose gradients from each individual beam, MFUD plans are more sensitive to set-up and range uncertainties than SFUD plans (Albertini et al., 2011). In clinic, this is currently compensated by using robust planning as described in *section 1.2.2.1*.

Despite PS provides a simple method for proton irradiation, it is commonly associated with a limited level of beam modulation and neutron contamination (Schneider and Hälg, 2015). In addition, the elimination of patient-specific mechanical devices saves the extra time required for their fabrication and insertion during treatment (Mohan and Grosshans, 2017). Consequently, the use of PS has been declining and been replaced by PBS, which provides greater flexibility and most importantly the delivery of IMPT.

1.3 Radiotherapy for children with abdominal tumors in the Netherlands

Since June 2018, the coordination of the oncological treatment of pediatric tumors has been centralized at the Princess Máxima Center (PMC) for Pediatric Oncology in Utrecht. The radiotherapy treatment with photons is provided by the radiotherapy department of the University Medical Center Utrecht (UMCU), while proton therapy is provided by the radiotherapy department of the University Medical Center Groningen (UMCG). In total, around 200 children are treated annually with radiotherapy in the Netherlands. Children with abdominal cancer, either with WT or NBL, represent about 20% (~ 30 to 40 patients) of the total number of irradiated patients (institutional data) (*Figure 1.2*).

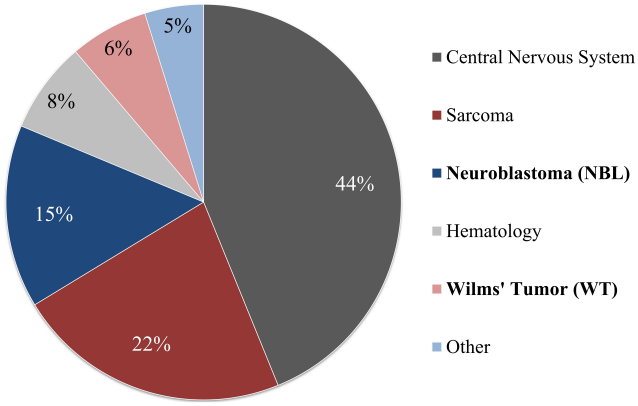

Figure 1.2 Circle chart denoting the percentage of pediatric patients treated for several indications at the radiotherapy department of UMCU (institutional data).

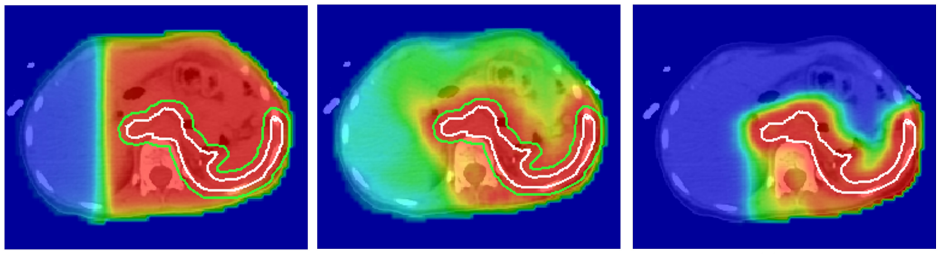

Figure 1.3 Transversal slices of (a) AP-PA (b) VMAT and (c) IMPT dose distributions for one WT patient (prescribed dose = 14.4 Gy). The PTV is shown in green and the ITV in white. The 95% isodose is shown in red.

Conventionally, two opposed anteroposterior-posteroanterior (AP-PA) photon fields have been used to cover abdominal target volumes (Gross and Neuhauser, 1950; de Kraker et al., 2001; SKION, 2015) (*Figure 1.3*). A known disadvantage of this technique is the large volume of NT receiving target dose levels. Based on single institutional experience and international trials (SKION, 2015; van den Heuvel-Eibrink et al., 2017), all WT and NBL patients in the Netherlands are currently treated with VMAT at the radiotherapy department of UMCU (*Figure 1.3*). Due to the unique dose-deposition pattern characterized by the low entrance dose and rapid dose fall-off (Lomax, 1999), IMPT treatments (*Figure 1.3*) have also become more widely available in the last few years to treat several indications in pediatric patients (Journy et al., 2019).

In the Netherlands, for pediatric patients, with the exception of craniospinal irradiation, referral for proton therapy is done after photon - proton plan comparison. Currently, around one-fourth (~ 50 patients) of the Dutch pediatric radiotherapy cohort is treated with protons at the radiotherapy department of UMCG. A disadvantage introduced by this planning comparison is the delay in the start of the treatment delivery which is not always acceptable for certain types of more aggressive tumors. For assessing the efficacy of using proton in alternative to photon therapy, (Langendijk et al., 2013; Widder et al., 2016) have developed a promising model-based approach. The main purpose is to select patients that will better benefit from proton compared to photon therapy in terms of NT complication probability (NTCP) reduction between techniques. NTCP models to predict patient-specific benefits with proton therapy are currently not available for children. Nevertheless, they would potentially aid physicians to make better informed referral decisions.

1.4 Image-guided radiotherapy

Image-guided RT (IGRT) stands for the use of imaging during radiotherapy to improve the overall treatment precision and accuracy. IGRT can be mainly reflected in the delineation and delivery stages of the radiotherapy workflow.

1.4.1 Delineation

Nowadays, target and OARs definition is commonly done by using CT imaging. Nevertheless, various imaging modalities have been added to the treatment preparation stage to improve the delineation of these structures such as magnetic resonance imaging (MRI) and positron emission tomography (PET). Due to the better soft-tissue contrast provided by MRI these images are mainly used for the determination of the extent of the tumor while PET images are mainly needed to provide additional physiological and metabolic information. Moreover, four-dimensional (4D)-CT and 4D-MR images can give important information regarding the breathing motion of the patient which is essential for the safety margins definition (Pai Panandiker et al., 2012; Kannan et al., 2017; Uh et al., 2017).

1.4.2 Delivery

On each treatment fraction, it is crucial to match the patient daily anatomy with the anatomy on the planning-CT. Nowadays, patients are positioned in the treatment room based on lasers and skin markers. During IGRT, the reproducibility of the correct patient treatment position is currently assured by means of on-board imaging devices. Most of photon IGRT treatments are performed using online cone-beam CT (CBCT) guidance (Jaffray et al., 2002). In proton IGRT treatments, planar x-ray imaging has been conventionally used for the last few decades (Flanz and Smith, 2009) but at the present time CBCT imaging is becoming more widely available (Park et al., 2009). To correct the patient position, automatic couches allowing rigid translations and if available rotations up to a certain maximum degree are currently employed. In addition, immobilization devices (i.e thermoplastic masks, knee supports, vacuum mattress) and general anesthesia (GA) can be used to limit the magnitude of treatment uncertainties. For children younger than 5 years, due to limited patient compliance, GA is commonly used during both treatment preparation and delivery (Fortney et al., 1999; Evans and Chisholm, 2008).

Despite CBCT imaging offers adequate bone contrast for patient position verification, the deformation and exact position of the tumor and OARs might be unnoticed due to the poor soft-tissue contrast. MRI yields superior soft-tissue visualization allowing for the identification of organ motion and physiological changes without giving extra radiation to the patient (Lagendijk et al., 2014). The inherent characteristics of MRI make it the logical choice to improve IGRT treatments. In the last decade, photon MRI-guided systems for real-time IGRT (Mutic and Dempsey, 2014; Raaymakers et al., 2017) have been introduced into the clinic with the goal of reducing treatment safety margins, due to the better soft-tissue visualization, online plan adaptation and motion tracking during irradiation (Lagendijk et al., 2014; Kontaxis et al., 2105a,b; Stemkens et al., 2016).

1.5 MRI in radiotherapy

1.5.1 MRI-only treatment planning

As described in *section 1.4.1*, the use of MRI to aid the target delineation has been growing in the last few years. Currently, a rigid registration between the CT and MR images is done to allow transferring MRI delineations to the planning-CT (Khoo and Joon, 2006). Potential registration errors will introduce a spatial systematic uncertainty in the treatment (Nyholm et al., 2009). A solution to remove this uncertainty is to replace the use of CT during both delineation and dose planning by MRI. Still, the performance of dose calculations when using MR images presents an important limitation. The MRI voxel intensity depends on the proton density and the nuclear magnetic relaxation (Brown et al., 2014). As MRI gives no direct information of the tissue attenuation properties needed for the dose calculation, the commonly named pseudo CT or synthetic CT (sCT) images, generated from the patient's MRI, are currently used for this purpose.

Up to now, four different sCT generation approaches have been reported in literature: bulk-density override, atlas-based, voxel-based and more recently introduced deep learning methods (Edmund and Nyholm, 2017; Johnstone et al., 2018). Bulk-density override has been studied for over a decade with either manual or automatic contour segmentation followed by bulk assignments of electron density values (Lee et al., 2003; Stanescu et al., 2008). For the atlas-based methods, the aim is to create an MRI - CT atlas and make a direct conversion of MRI intensity into HU values by registering the patient's MRI to the atlas (Dowling et al., 2012, 2015; Uh et al., 2014; Guerreiro et al., 2017). Voxel-based methods mainly use the MRI contrast, independently of the voxels spatial location, to provide a direct conversion of MRI intensity into HU values (Hsu et al., 2013; Edmund et al., 2014; Korhonen et al., 2014). Finally, deep learning methods provide a fast sCT generation by using either convolutional neural networks (CNN) (Han, 2017; Dinkla et al., 2018) or conditional generative adversarial networks (cGAN) (Maspero et al., 2018).

1.5.2 MRI-guided delivery

Considering the importance of obtaining sufficient target coverage while at the same time reducing the NT dose, (Lagendijk and Bakker, 2000) presented first the idea of combining a linac with a diagnostic MRI scanner for online MRI-guidance during photon delivery. MRI-linac devices (Fallone, 2014; Keall et al., 2014; Mutic and Dempsey, 2014; Raaymakers et al., 2017) enable the patient anatomy visualization in the pre-beam phase, prior to radiation delivery, and more importantly in the beam-on phase, during radiation delivery. Pre-beam images can be used for patient positioning, daily plan adaptation and motion characterization (Kontaxis et al., 2015b, 2017a; Stemkens et al., 2015). Beam-on images can be further used for motion mitigation (i.e gating, tracking) (Glitzner et al., 2015a,b; Stemkens et al., 2016) and ultimately for intra-fraction re-planning (Kontaxis et al., 2015a, 2017b). These strategies allow for patient-specific safety margins to be created and updated during treatment and potentially for the use of smaller expansions as there is a greater confidence in the exact target location with MRI.

At the UMCU, an MRI-linac featuring a diagnostic high-field 1.5 T MRI scanner (Philips, Best, The Netherlands) in combination with a 7 MV Flattening Filter Free (FFF) linac (Elekta AB, Stocholm, Sweden) able to rotate 360° around the MRI bore was developed (Lagendijk et al., 2008; Raaymakers et al., 2009) (*Figure 1.4*). Since 2018, this device has been clinically approved and used to treat lumbar spine bone and lymph node metastases, prostate, rectum and esophagus cancer patients up to now. In particular for pediatric tumors, MRI-guided photon treatments have not yet been clinically introduced. Nevertheless, these treatments seem to be particularly promising for children, for whom there is a special concern for dosimetric sparing and consequently for minimizing the occurrence of radiotherapy late effects.

For the integration of an MRI scanner with a linac, the influence of the lateral magnetic field on the delivered photon dose distribution has been extensively studied in literature. The main effect of the magnetic field on the photon radiation is commonly called electron return effect (ERE). The ERE is caused by the interaction of the secondary elec-

trons with air, describing a circular shaped trajectory. As a result, extra dose deposition at tissue-air interfaces is denoted (Raaijmakers et al., 2005). The ERE around air pockets can be compensated by the use of opposing photon radiation fields (Raaijmakers et al., 2007,a,b), while the ERE at the patient surface can be accounted during treatment planning by using Monte Carlo (MC) optimization algorithms (Ziegenhein et al., 2015).

The development of the MRI-linac in the last decade has led to the consideration of a possible hybrid MRI-guided proton therapy system (Raaymakers et al., 2008). Despite MRI-guidance during proton delivery is not clinically available yet, research has been going on to prove the feasibility of this system and the corresponding treatment workflow (Oborn et al., 2017). When passing through a magnetic field, due to their charge, protons are subjected to the Lorentz force resulting in a curved proton trajectory (Raaymakers et al., 2008; Wolf and Bortfeld, 2012). Nevertheless, in contrast to photons and for magnetic field strengths up to 1.5 T, no effect on the proton dose distribution was detected at tissue-air interfaces and the proton beam curvature was shown to be compensated by using MC inverse optimization algorithms (Raaymakers et al., 2008; Hartman et al., 2015).

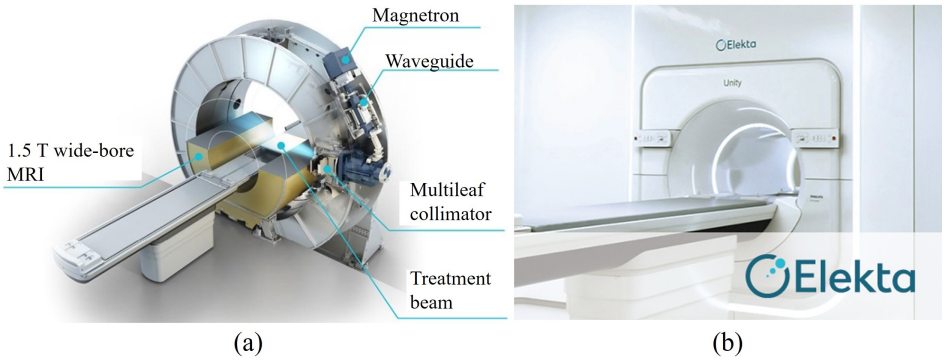

Figure 1.4 Elekta Unity MRI-linac: (a) schematic and (b) clinical machine.

1.6 Thesis outline

For a better use of radiotherapy in children, doctors and researchers have been trying for years to improve treatment effectiveness and to minimize the radiation long-term complications. The goal of this thesis was to investigate the best available IGRT techniques to treat pediatric patients with abdominal tumors, more specific with WT or NBL.

A comprehensive treatment uncertainties assessment of abdominal target volumes is required to take advantage of the state-of-the-art radiotherapy techniques. Despite IGRT treatments are currently widely employed for several indications in pediatric patients, international guidelines on its optimal use are rare (Alcorn et al., 2014; Wall et al., 2018). For WT patients undergoing flank irradiation, radiotherapy is currently based on the International Society of Paediatric Oncology (SIOP)-2001 protocol (de Kraker et al., 2001).

In this protocol, the PTV margin is suggested to be 10 mm without image guidance. In **chapter 2**, intra- and inter-fraction motion of the target and OARs and patient set-up uncertainties were quantified aiming to estimate more adequate safety margins while having available CT, 4D-CT and daily CBCT information during treatment for this patient category.

Moreover, radiotherapy treatments of WT and NBL patients at the UMCU are currently done using a CBCT-guided VMAT workflow. In this thesis, **chapter 3** and **4** are focused in evaluating the potential dosimetric benefit of treating this patient category with novel IGRT techniques compared to the current VMAT workflow: MRI-guided photon therapy using an IMRT delivery (**chapter 3**) and CBCT-guided IMPT using a PBS delivery (**chapter 4**).

In **chapter 3**, the potential reduction of the PTV margin and its dosimetric impact when using MRI-guided IMRT ($IMRT_{MRI}$) compared to CBCT-guided VMAT treatments were investigated for a group of WT patients. 4D-CT, CBCT and MR images, acquired during treatment planning and delivery, were used to estimate the PTV expansion for each workflow. For the dosimetric comparison, $IMRT_{MRI}$ and VMAT plans were generated using five margin scenarios (estimated PTV ± 0, 1 and 2 mm). In addition, $IMRT_{MRI}$ plans were optimized accounting for a 1.5 T transverse magnetic field to realistically model an MRI-guided treatment.

In **chapter 4**, the dosimetric sparing and robustness against inter-fraction anatomical changes between CBCT-guided intensity-modulated PBS and VMAT techniques were determined for WT and NBL patients. Both VMAT and PBS plans were robustly optimized on the patient-specific ITV using clinical set-up and range (only for PBS) uncertainties. To assess the robustness of both VMAT and PBS dose distributions against daily anatomical changes, fractional dose re-calculations were performed using clinical CBCT images. For the estimation of the HUs from the daily CBCT data, the planning-CT was deformably registered to the CBCTs.

During IGRT treatments, for the use of MRI-only planning and / or MRI-guided delivery, sCT images are currently employed for the dose calculation performance. In the past few years, sCT images have been generated for several body sites (i.e brain, head and neck, pelvis) in adult patients but nothing yet was reported for children with abdominal cancer. In **chapter 5**, a method enabling sCT generation of the whole abdomen using MR images of pediatric patients treated for WT and NBL was developed. The proposed method relies on an automatic atlas-based segmentation of bone and lungs followed by a direct MRI intensity to HU values conversion. The dosimetric accuracy of the generated sCTs was verified for both robustly optimized VMAT and PBS dose distributions.

Finally, the most relevant findings of this thesis are summarized and discussed in **chapter 6**. Moreover, possible future studies and perspectives on the use of MRI-guided proton therapy to treat this patient category are also outlined in this chapter.

CHAPTER 2

Intra- and inter-fraction uncertainties during IGRT for Wilms' tumor

The following chapter is based on:

Guerreiro F, Seravalli E, Janssens GO, van de Ven CP, van den Heuvel-Eibrink MM and Raaymakers BW 2018 Intra- and inter-fraction uncertainties during IGRT for Wilms' tumor. *Acta Oncol.* 57(7):941-9.

Abstract

Background and Purpose: To assess intra- and inter-fraction motion uncertainties, due to displacements of the tumor bed (TB) and organs at risk (OARs), as well as intra- and inter-fraction patient set-up uncertainties, due to patient position variations, during image-guided radiation therapy (IGRT) in children with Wilms' tumor (WT).

Material and Methods: Four-dimensional computed tomography (4D-CT) and daily pre- and post-treatment cone-beam CT (CBCT) images of 15 WT patients (average 4, range 1 - 8 years) undergoing flank irradiation after nephrectomy were analyzed. TB (marked by four surgical clips) and OARs motion uncertainties were quantified by displacements of the center of mass in all orthogonal directions. Translational and rotational bone off-sets were recorded for patient set-up uncertainties assessment in all orthogonal directions. The average results, systematic and random errors were computed.

Results: Average intra- and inter-fraction motion uncertainties were $\leq$ 1.1 mm (range [-7.3 ; 7.9] mm) for the TB and $\leq$ 3.2 mm (range [-9.9 ; 9.6] mm) for the OARs. Average intra- and inter-fraction patient set-up uncertainties were $\leq$ 0.1 mm (range [-3.3 ; 4.8] mm) and $\leq 0.9^\circ$ (range $[0.0^\circ ; 2.8^\circ]$). Both motion and patient set-up uncertainties were larger for the craniocaudal direction. Calculated systematic and random errors were $\leq$ 2.4 mm for the motion uncertainties and $\leq$ 0.8 mm / 0.7° for the patient set-up uncertainties.

Conclusions: Average motion and patient set-up uncertainties during radiotherapy treatment were found to be limited. However, uncertainties were larger for the craniocaudal direction and a wide distribution among patients was found. When having available 4D-CT and CBCT information, the use of patient-specific and anisotropic safety margins is advised for both target volume and OARs.

2.1 Introduction

Wilms' tumor (WT) is the most common malignancy of the kidney in childhood. By tailoring systemic agents, surgery and radiotherapy, overall survival of WT patients has been consistently high over the last decades (de Kraker et al., 2004; Pritchard-Jones et al., 2015). Therefore, long-term toxicity of cancer treatments has become an important issue. In addition to treatment-induced neoplasms (Taylor et al., 2008), children undergoing abdominal radiotherapy are at increased risk of developing orthopedic, renal, metabolic, hepatic and vascular problems (Rate et al., 1991; Ritchey et al., 1996; van Waas et al., 2012).

In the radiotherapy workflow, there are many possible sources of uncertainty that may limit the accuracy of the treatment such as: (1) delineation (systematic), (2) motion (systematic and random) and (3) patient set-up (systematic and random) uncertainties. Delineation uncertainties are caused by inter-observer variability and by differences between imaging modalities (i.e soft-tissue contrast). Motion uncertainties arise from displacements of the tumor bed (TB) and organs at risk (OARs) either caused by respiration (intra-fraction uncertainty) or by day-to-day variations like organ filling and / or weight changes (inter-fraction uncertainty). Patient set-up uncertainties result from patient position differences during treatment delivery (intra-fraction uncertainty) or in between fractions (inter-fraction uncertainty). As a consequence, safety margins should be used for both TB and OARs to assure adequate target coverage without exceeding the normal tissue (NT) dose constraints (van Herk, 2004).

Motion and / or patient set-up uncertainties have already been studied for abdominal tumors in adults (Wysocka et al., 2010; van den Horst et al. 2013; Pham et al., 2014) and children (Beltran et al., 2010; Nazmy et al., 2012; Pai Panandiker et al., 2012; Huijskens et al. 2015, 2017; Kannan et al., 2017; Uh et al., 2017; van Dijk et al., 2017). Four-dimensional computed tomography (4D-CT) (Pai Panandiker et al., 2012; Kannan et al., 2017) and 4D-magnetic resonance imaging (MRI) (Uh et al., 2017) are used to estimate the breathing uncertainty and daily cone-beam CT (CBCT) images to assess both intra- and inter-fraction uncertainties (Beltran et al., 2010; Nazmy et al. 2012; Huisjkens et al., 2015, 2017; van Dijk et al., 2017). However, none of these studies with pediatric patients has investigated both intra- and inter-fraction TB and OARs motion and patient set-up uncertainties for a homogeneous disease patient cohort at a single institute.

A comprehensive assessment of uncertainties for abdominal target volumes is essential to take advantage of the state-of-the-art radiotherapy techniques, such as intensity-modulated radiation therapy (IMRT), volumetric modulated arc therapy (VMAT) and intensity-modulated proton therapy (IMPT). Thus, the purpose of this study was to analyze these uncertainties during image-guided radiation therapy (IGRT) in pediatric patients with WT undergoing flank irradiation using 4D-CT and daily CBCT images.

2.2 Materials and Methods

A flowchart with all the steps of the pediatric radiotherapy chain at the radiotherapy department of the University Medical Center Utrecht (UMCU), The Netherlands, is represented in *Figure 2.1*. For each step included in the uncertainty analysis, a detailed explanation of the method used is described in the following sections.

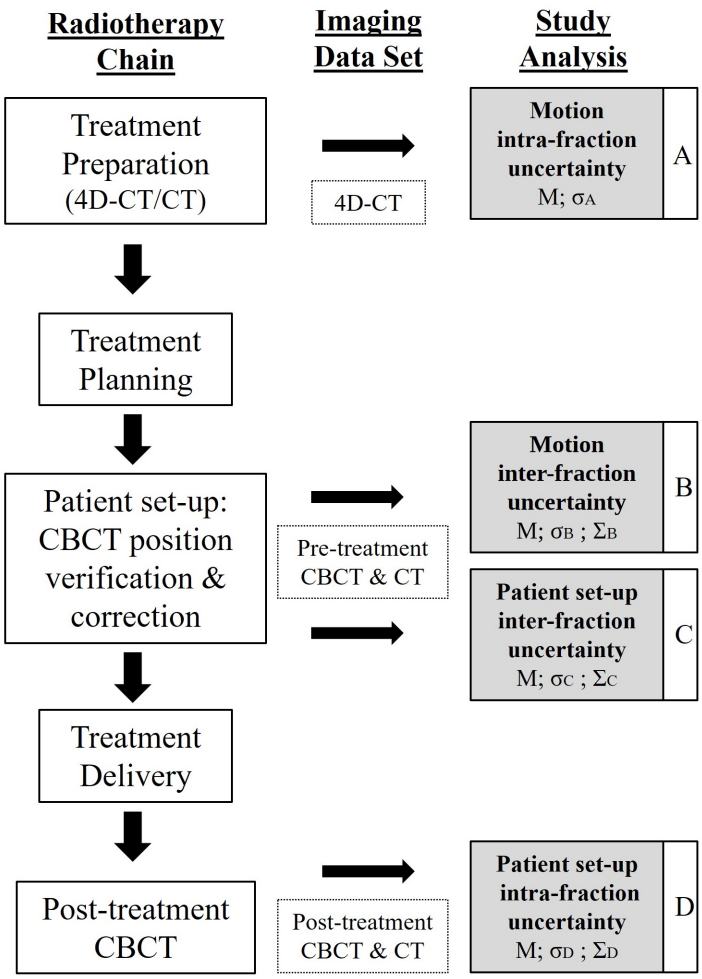

Figure 2.1 Radiotherapy treatment chain for pediatric patients treated at the radiotherapy department of the University Medical Center Utrecht (UMCU), and the stages of motion and patient set-up uncertainty analysis (steps A - D) with the corresponding imaging modality used for the assessment. The planning-CT was obtained by averaging the 4D-CT and was used for the registrations with the daily CBCTs. Post-treatment CBCTs were only acquired for the first three to five fractions of each patient (*Supplementary Material, section 2.6*).

2.2.1 Patient and treatment characteristics

After institutional review board approval (WAG/mb/17/008865), 15 consecutive patients (six males, nine females) with WT undergoing flank irradiation between April 2015 and October 2016 at the UMCU were included in this study. The average patient age at the time of treatment was 4 years (range 1 - 8 years). After four to six weeks of induction chemotherapy, a nephrectomy with para-aortic lymph node sampling was performed. A right nephrectomy was done for a total of eight patients while the remaining seven patients received a left nephrectomy (*Supplementary Material, section 2.6*). During surgery, four titanium clips were placed at the superior (close to the diaphragm), lateral and medial (close to the vessels) and inferior (close to the ureter stump) tumor resection margins. The stability of the position of the surgical clips was verified during treatment by calculating the distance between the clips on the pre-treatment CBCTs. No signs of clip migration were observed.

Treatment preparation was performed under general anesthesia (GA) in ten out of the 15 patients. Furthermore, radiotherapy was delivered under GA for six patients due to limited patient compliance (*Supplementary Material, section 2.6*). A radiotherapy dose between 14.4 and 25.2 Gy was delivered to all patients using a 10 MV full-arc VMAT technique performed on an Elekta synergy linear accelerator (linac) equipped with an Agility multileaf collimator (Elekta, Stockholm, Sweden). The duration of the radiotherapy fractions, including imaging and irradiation, was on average 9 min.

2.2.2 4D-CT and CBCT imaging: acquisition and registration

For each patient, all available images, including a planning 4D-CT and daily CBCTs, were analyzed. Patients were fixated in a supine position in a vacuum mattress (Bluebag, Elekta, Stockholm, Sweden) with the arms wide along the body.

The 4D-CT images were obtained using a 16-, 40-, or 64- channel detector scanner (Brilliance, Philips Medical Systems, Best, The Netherlands) in spiral mode with the following parameters: 170 mAs/slice, 120 kV, 0.44 s gantry rotation, 0.08 pitch, 1.5 mm collimation and 3 mm slice thickness. Each respiratory cycle during free-breathing was captured as a series of ten phases acquired at equally spaced intervals between 0% and 100%. Respiratory trace measurements for pulmonary gating were obtained using a deformable rubber belt fixed to the patient's chest (Philips Bellow System, Best, The Netherlands). Furthermore, the planning-CT was obtained by taking the pixel-by-pixel average of the ten phases of the 4D-CT. Both planning-CT and 4D-CT images shared the same spatial coordinates, thus no additional co-registration step was necessary.

Daily pre-treatment CBCTs were acquired for all treatment fractions using the Elekta XVI 4.5.1 on-board CBCT imaging system (Elekta, Stockholm, Sweden). Scans with an arc of 200° of 10 ms and 16 mA with 100 kV and an acquisition timeframe of 30 s, leading to four times less imaging dose than a standard adult protocol, were taken. Each daily pre-treatment CBCT was co-registered to the planning-CT using the automatic rigid

registration algorithm available clinically on the Elekta XVI software v5.0 (Borgefors, 1988). Translational and rotational bone off-sets were obtained using a region of interest encompassing the vertebral column representative for the area in close proximity to the TB. Translational bone off-sets were corrected online using the automated treatment table movement. Rotational bone off-sets were not directly corrected for and only when larger than 3°, in at least one orthogonal direction, patient re-positioning was performed.

At our department, instead of the 10 mm planning target volume (PTV) margin around the clinical target volume (CTV), as recommended in the International Society of Paediatric Oncology (SIOP)-2001 protocol (de Kraker et al., 2001), a 5 mm margin is employed around a patient-specific internal target volume (ITV). The ITV is used to account for the breathing uncertainty and is defined by visual inspection of the surgical clips motion on the 4D-CT image. As no information on the intra-fraction patient set-up uncertainty was available for this patient cohort, post-treatment CBCTs were acquired for the first three to five fractions of each patient to assess this uncertainty (*Supplementary Material, section 2.6*). The post-treatment CBCTs were co-registered to the planning-CT using the same procedure followed for the pre-treatment CBCTs. In total, 138 pre-treatment and 50 post-treatment CBCT images were analyzed (*Supplementary Material, section 2.6*).

2.2.3 Uncertainties assessment

2.2.3.1 Motion (Figure 2.1, steps A & B)

Measurements of the motion uncertainties were done offline using the clinical registered images (*section 2.2.2*) and an in-house delineation software (Bol et al., 2009). For the purpose of this study, the clips, contralateral kidney, liver and spleen were delineated on the planning-CT by one radiation oncologist. TB and OARs motion uncertainties were quantified by center of mass (CoM) displacements, in all orthogonal directions, as this measure is less sensitive to organ deformation. The + and - signs indicate right/posterior/cranial and left/anterior/caudal directions, respectively. The individual displacements of the four surgical clips were used as surrogate for the TB motion.

For the intra-fraction uncertainty estimation (step A), the clips and OARs contours were translated / rotated from the planning-CT to match the anatomy of the maximum expiration and inspiration phases of the 4D-CT (*Figure 2.2*). Maximum expiration and inspiration phases of the 4D-CT were selected by visual inspection (*Supplementary Material, section 2.6*). Deviations in the boundaries of the contours (i.e to remove the presence of air pockets from the inside of the contours) were corrected manually. Average volume differences between the defined contours on both 4D-CT phases were negligible (kidney $\leq 1\%$, liver $\leq 4\%$, spleen $\leq 2\%$). CoM displacements between the maximum expiration, used as reference, and inspiration phases of the 4D-CT were calculated per patient.

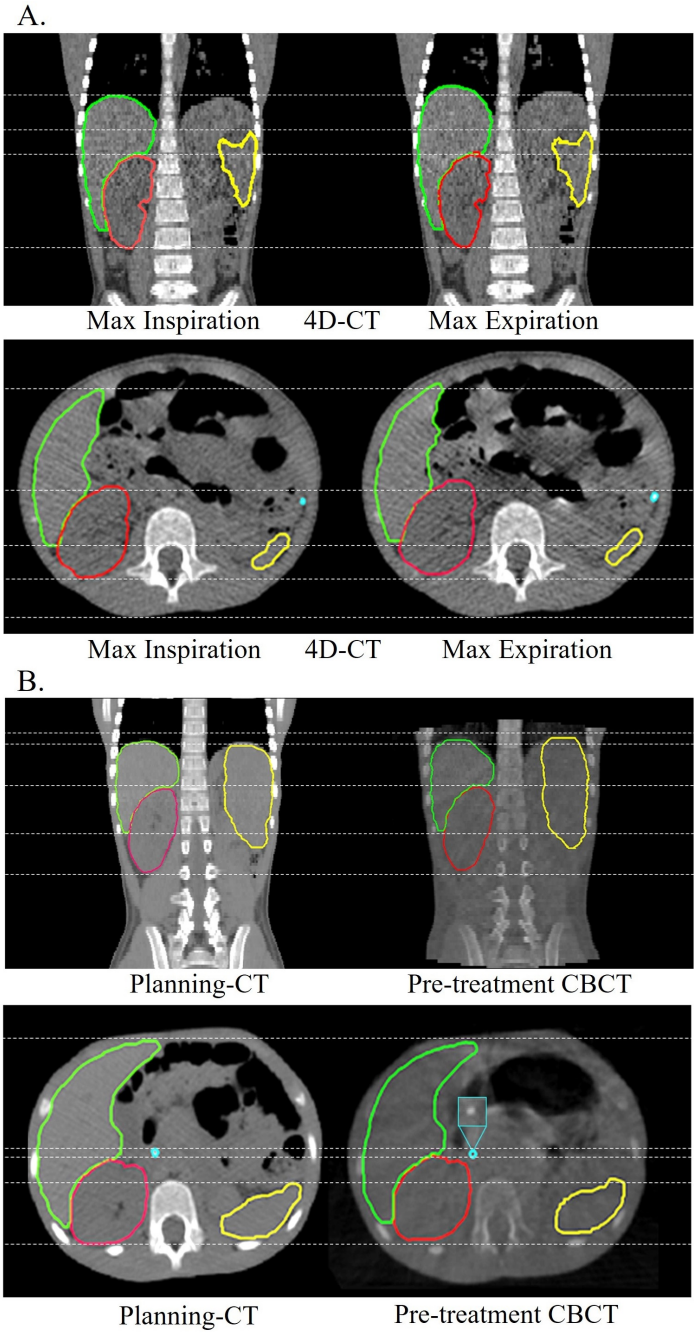

Figure 2.2 Examples of the imaging data sets used for the motion uncertainty assessment for both intra-fraction (A, top rows) and inter-fraction (B, bottom rows) uncertainties for one patient. Dashed white lines are used to help identifying the borders of the delineated structures: liver (in green), kidney (in red), spleen (in yellow), one surgical clip (in blue).

For the inter-fraction uncertainty assessment (step B), the clips and OARs contours were translated / rotated from the planning-CT to match the anatomy of the pre-treatment CBCTs (*Figure 2.2*). Deviations in the boundaries of the contours (i.e due to different breathing phases) were corrected manually. Average volume differences between the planning-CT contours and the modified contours on the CBCTs were negligible (kidney $\leq$ 2%, liver and spleen $\leq$ 6%). CoM displacements between the planning-CT, used as reference, and the pre-treatment CBCT images were determined for each patient.

2.2.3.2 Patient set-up (Figure 2.1, steps C & D)

For the assessment of the patient set-up uncertainties, the clinical registered images (*section 2.2.2*) were used.

For the intra-fraction uncertainty assessment (step D), the post-treatment CBCTs were used to calculate the translational and rotational bone off-sets with respect to the planning-CT for each patient (Beltran et al., 2010). Due to software reasons, the bone off-sets between the post-treatment CBCTs and the planning-CT, instead of the pre-treatment CBCTs, were used. Nevertheless, negligible differences in the bone off-sets in all orthogonal directions ($\leq$ 0.05 mm / 0.3°) were observed between methodologies.

For the inter-fraction uncertainty assessment (step C), the pre-treatment CBCTs were used to calculate the translational and rotational patient bone off-sets with respect to the planning-CT. During treatment, the alignment between the patient's planning and treatment position at the target volume location was achieved by applying online translational shifts to the treatment table (*section 2.2.2*). Within the XVI software, rotational bone off-sets are converted into translational shifts resulting in a residual translational patient set-up uncertainty. The difference between the translational bone off-sets provided by the XVI software and the correction applied to the treatment table was used to estimate this translational inter-fraction patient set-up uncertainty.

2.2.4 Uncertainties analysis

2.2.4.1 Motion (Figure 2.1, steps A & B)

For the intra-fraction uncertainty, the results are expressed as a group mean (M), as a range of values and as a group random error (σ_A; the standard deviation (SD) of the individual values of all patients) (van Herk et al., 2003; van Herk, 2004). For the inter-fraction uncertainty, the results are expressed as a M, as a range of values, as a group systematic error (Σ_B; the SD of the individual means of all patients) and as a group random error (σ_B; root mean square (RMS) of the individual SDs) (van Herk, 2004).

2.2.4.2 *Patient set-up (Figure 2.1, steps C & D)*

For both intra- and inter-fraction uncertainties, the results are expressed as a M, as a range of values, as a group systematic error ($\Sigma_{C,D}$; the SD of the individual means of all patients) and as a group random error ($\sigma_{C,D}$; RMS of the individual SDs) (van Herk, 2004).

2.3 Results

For the intra-fraction motion uncertainty (step A), M was smaller than 0.8 mm for the TB (range [-1.9 ; 3.3] mm) and 3.2 mm for the OARs (range [-3.4 ; 5.5] mm) in all orthogonal directions (*Table 2.1, Figure 2.3*). σ_A was smaller than 1.4 mm (*Table 2.2*). For the inter-fraction motion uncertainty (step B), M was smaller than 1.1 mm for the TB (range [-7.3 ; 7.9] mm) and 1.2 mm for the OARs (range [-9.9 ; 9.6] mm) in all orthogonal directions (*Table 2.1, Figure 2.3*). Σ_B and σ_B were smaller than 2.4 mm (*Table 2.2*).

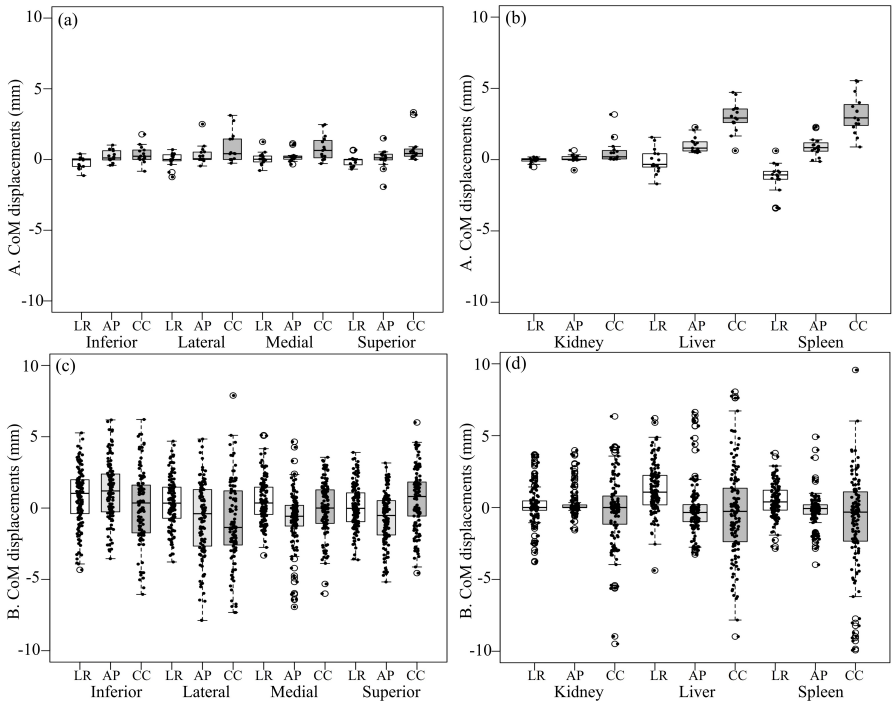

Figure 2.3 Boxplots with jitter describing the intra- (top row, step A) and inter-fraction (bottom row, step B) center of mass (CoM) displacements of the tumor bed (TB, (a)(c)) and organs at risk (OARs, (b),(d)) for each orthogonal direction. Horizontal bar, boxes, whiskers and circles represent median values, 50th and 90th percentiles and outliers, respectively. *Abbreviations: LR= left-right; AP= anterior-posterior; CC= craniocaudal.*

The CoM displacements were more pronounced in the craniocaudal (CC) direction for both intra- and inter-fraction motion uncertainties (*Figure 2.3*). Moreover, a large number of outliers in the TB and OARs CoM displacements were denoted among patients, especially for the inter-fraction motion uncertainty (*Figure 2.3*).

For the intra-fraction patient set-up uncertainty (step D), M was smaller than 0.1 mm (range [-3.3 ; 4.8] mm) and 0.9° (range [0.0° ; 2.8°]) in all orthogonal directions (*Table 2.1*). Σ_D and σ_D were smaller than 0.8 mm and 0.7° (*Table 2.2*). For the inter-fraction patient set-up uncertainty (step C), M was smaller than 0.1 mm (range [-0.9 ; 0.8] mm) in all orthogonal directions (*Table 2.1*). Σ_C and σ_C were smaller than 0.2 mm (*Table 2.2*). Few outliers in both intra-and inter-fraction patient set-up uncertainties were detected among patients in all orthogonal directions.

Table 2.1 Group mean (M) and range results for the motion (steps A & B) and patient set-up (steps C & D) uncertainties. Steps A and D are related to the intra-fraction and steps B and C to the inter-fraction uncertainties. Only the bone off-set rotational shift measures are presented in degrees. *Abbreviations: LR= left-right; AP= anterior-posterior; CC= craniocaudal; OARs= organs at risk; TB= tumor bed.*

Error Source	**Evaluated Structure**		**Measure** (mm/degree)	**LR**	**AP**	**CC**
A	**TB (clips)**	Superior	*M*	-0.1	0.1	0.8
			Range	[-0.7 ; 0.7]	[-1.9 ; 1.5]	[0.0 ; 3.3]
		Lateral	*M*	0.0	0.3	0.8
			Range	[-1.2 ; 0.4]	[-0.5 ; 2.5]	[-0.3 ; 3.1]
		Medial	*M*	0.1	0.2	0.8
			Range	[-0.8 ; 1.3]	[-0.3 ; 1.1]	[-0.3 ; 2.5]
		Inferior	*M*	-0.2	0.2	0.4
			Range	[-1.1 ; 0.4]	[-0.4 ; 1.0]	[-0.8 ; 1.8]
	OARs	Kidney	*M*	0.0	0.1	0.6
			Range	[-0.5 ; 0.2]	[-0.7 ; 0.7]	[0.0 ; 3.2]
		Liver	*M*	-0.1	1.0	3.0
			Range	[-1.7 ; 1.6]	[0.5 ; 2.3]	[0.6 ; 4.7]
		Spleen	*M*	-1.3	0.9	3.2
			Range	[-3.4 ; 0.6]	[-0.1 ; 2.3]	[0.9 ; 5.5]
B	**TB (clips)**	Superior	*M*	0.2	-0.5	1.0
			Range	[-3.6 ; 3.9]	[-4.6 ; 3.2]	[-4.6 ; 6.0]
		Lateral	*M*	0.2	-0.6	-1.1
			Range	[-3.8 ; 3.7]	[-5.5 ; 4.8]	[-7.3 ; 7.9]
		Medial	*M*	0.4	-0.6	-0.1
			Range	[-3.3 ; 3.8]	[-4.1 ; 4.7]	[-5.3 ; 3.3]
		Inferior	*M*	0.5	1.1	0.3
			Range	[-4.3 ; 5.2]	[-3.6 ; 6.2]	[-6.0 ; 6.2]
	OARs	Kidney	*M*	0.1	0.4	-0.2
			Range	[-3.7 ; 3.7]	[-1.6 ; 3.9]	[-9.4 ; 6.3]
		Liver	*M*	1.2	-0.1	-0.2
			Range	[-4.3 ; 6.2]	[-3.3 ; 6.6]	[-9.0 ; 8.1]
		Spleen	*M*	0.5	-0.2	-1.0
			Range	[-2.7 ; 3.5]	[-4.0 ; 4.9]	[-9.9 ; 9.6]
C	**Bone off-set**	Translational shift	*M*	0.1	-0.1	0.0
			Range	[-0.5 ; 0.7]	[-0.9 ; 0.8]	[-0.6 ; 0.6]
D	**Bone off-set**	Translational shift	*M*	0.0	-0.1	0.0
			Range	[-3.3 ; 2.0]	[-2.7 ; 3.2]	[-0.7 ; 4.8]
		Rotational shift	*M*	0.9	0.8	0.8
			Range	[0.0 ; 2.6]	[0.0 ; 2.8]	[0.0 ; 2.4]

Table 2.2 Calculated group systematic (Σ) and group random (σ) errors for the intra- and inter-fraction motion (steps A & B) and patient set-up (steps C & D) uncertainties. Steps A and D are related to the intra-fraction and steps B and C to the inter-fraction uncertainties. Only the bone off-set rotational shift measures are presented in degrees. *Abbreviations: LR= left-right; AP= anterior-posterior; CC= craniocaudal; OARs= organs at risk; TB= tumor bed.*

Error Source	Evaluated Structure		Error (mm/degree)	LR	AP	CC
A	TB (clips)	Superior	σ_A	0.4	0.7	1.0
		Lateral		0.5	0.7	1.1
		Medial		0.5	0.4	0.9
		Inferior		0.4	0.4	0.6
	OARs	Kidney	σ_A	0.2	0.3	0.9
		Liver		0.9	0.6	1.1
		Spleen		1.1	0.7	1.4
B	TB (clips)	Superior	Σ_B	1.1	1.2	1.1
			σ_B	1.2	1.3	1.7
		Lateral	Σ_B	1.4	2.0	2.2
			σ_B	1.2	1.8	1.9
		Medial	Σ_B	1.0	1.4	1.1
			σ_B	1.2	1.3	1.7
		Inferior	Σ_B	1.6	1.5	1.5
			σ_B	1.4	1.4	2.0
	OARs	Kidney	Σ_B	1.1	0.7	1.8
			σ_B	0.8	0.7	1.6
		Liver	Σ_B	0.8	1.7	2.4
			σ_B	1.5	1.1	2.2
		Spleen	Σ_B	0.7	0.8	2.4
			σ_B	1.0	0.9	2.4
C	Bone off-set	Translational shift	Σ_C	0.1	0.2	0.1
			σ_C	0.0	0.0	0.0
D	Bone off-set	Translational shift	Σ_D	0.5	0.4	0.4
			σ_D	0.7	0.8	0.8
		Rotational shift	Σ_D	0.6	0.5	0.4
			σ_D	0.6	0.6	0.7

2.4 Discussion

The purpose of this study was to quantify the intra- and inter-fraction motion and patient set-up uncertainties during IGRT, using 4D-CT and daily CBCT images, of 15 patients with WT undergoing flank irradiation. Results demonstrate on average limited motion and negligible patient set-up uncertainties during treatment. However, a large number of outliers for the TB and OARs motion uncertainties were found among patients, especially for the inter-fraction uncertainty.

For the motion uncertainties, maximum CoM displacements were smaller than 8 mm and 10 mm in magnitude for the TB and OARs, respectively. Published studies have already reported the intra-fraction motion uncertainty for pediatric patients by calculating the CoM displacements between the maximum expiration and inspiration phases of 4D-CT (Pai Panandiker et al., 2012; Kannan et al., 2017) and 4D-MR images (Uh et al., 2017).

For the TB, (Uh et al., 2017) quantified the breathing uncertainty for 17 patients younger than 8 years using 4D-MRI scans. A larger average CoM displacement of the TB (1.6 mm vs. 0.8 mm) was found by (Uh et al., 2017) possibly due to the use of the whole CTV volume as surrogate for the TB motion instead of the surgical clips. In the present study, the use of the CTV as motion surrogate would be insufficient as the TB is not clearly discernible on the 4D-CT images.

Regarding the OARs, literature is available for the kidneys (Pai Panandiker et al., 2012; Kannan et al., 2017; Uh et al., 2017), spleen and liver (Kannan et al., 2017; Uh et al., 2017). (Pai Panandiker et al., 2012), using 4D-CT images of a similar patient cohort (11 patients, range 2 - 8 years) reported slightly larger average CoM displacements of the kidney (1.9 mm vs. 0.6 mm). The difference can be explained by the use of absolute CoM displacements instead of considering the sign of the displacement as in the present study. With the purpose of calculating Σ and σ, the measured displacements and not their absolute values should be used (van Herk, 2004). (Kannan et al., 2017) found for 15 patients, while using 4D-CT images, average CoM displacements of 1.4, 2.5 and 3.1 mm in the CC direction for the kidney, liver and spleen, respectively. (Uh et al., 2017) reported average CoM displacements of 1.6, 3.2 and 3.0 mm in the CC direction for the kidney, liver and spleen, respectively. The results observed in this study were comparable with the results from both publications (Kannan et al., 2017; Uh et al., 2017).

Furthermore, published studies have already addressed the inter-fraction motion uncertainty of the CTV (Nazmy et al., 2010), kidneys (Nazmy et al., 2010; Huijskens et al., 2015) and liver (Nazmy et al., 2010) but no information is available on the spleen. (Nazmy et al., 2010) looked at the CTV CoM displacements, using CBCTs of four neuroblastoma patients, and found a maximum displacement in the CC direction of 5 mm (vs. 8 mm). Deviations can be explained by differences in the methodology as (Nazmy et al., 2010) used the whole CTV volume rather than the individual surgical clips for the TB motion uncertainty estimation. (Huijskens et al., 2015) observed an average kidney CoM displacement smaller than 1.5 mm (vs. 0.6 mm) by using CBCTs of a heterogeneous group of 39 patients. The difference could be related to the considered patient population - mean age of 4 years in the present study and 8 years in (Huijskens et al., 2015) study. Furthermore, (Nazmy et al., 2010) while using CBCTs of nine patients showed a maximum displacement in the CC direction of 10 mm (vs. 9 mm) for the kidneys and 13 mm (vs. 9 mm) for the liver. The use of the upper pole of the organs (vs. CoM) for the motion estimation could explain the deviations between the results of (Nazmy et al., 2010) and the results of this study. The CoM displacements are less sensitive to deformations, thus (Nazmy et al., 2010) might have interpreted deformations as translations while performing measurements with the upper pole of the organs.

In the present study, the inter-fraction motion uncertainty was found to be larger when compared to the intra-fraction uncertainty. However, the inter-fraction uncertainty might be potentially overestimated due to variations in the imaging procedures. Despite the negligible percentage of volume differences seen between contours delineated on the planning-CT and on the CBCT images ($\leq$ 6%), different image acquisition meth-

ods may still influence the baseline organ position due to breathing and the visibility of the organ boundaries, especially for the CBCTs as a result of the poorer soft-tissue contrast.

The use of GA to immobilize patients during IGRT and patient-specific factors (i.e weight, height) might also affect the TB and OARs motion uncertainties. Several studies in literature reported previously on this (Pai Panandiker et al., 2012; Kannan et al., 2017; Huijskens 2015, 2017). (Pai Panandiker et al., 2012) found that the intra-fraction motion uncertainty of the kidney was smaller for patients treated with GA. They also concluded that renal motion had a significant correlation with the age and height of the patient. However, (Kannan et al., 2017) did not found significant differences in the intra-fraction motion uncertainty of the OARs based on the use of GA and the patient age. Moreover, (Huijskens et al., 2015, 2017) reported that no significant correlations were found between the inter-fraction motion uncertainty of the kidney and height (Huijskens et al., 2015) and between the intra- and inter-fraction motion uncertainties of the diaphragm and patient-specific factors (i.e age, height, weight) (Huijskens et al., 2017). In addition, for WT patients, the nephrectomy side might also influence the motion of the TB and the surrounding OARs. However, no data is available in literature on this. In the present study, the relation between the intra- and inter-fraction TB and OARs motion uncertainties and the use of GA and nephrectomy side was analyzed using a non-parametric Mann-Whitney-U test (data not shown). Significance differences were only found regarding the inter-fraction motion and the nephrectomy side (right vs. left side) for the liver (average -1.1 vs. 0.6 mm) and spleen (average -1.4 vs. -0.4 mm) in the CC direction. Moreover, the correlation between the TB and OARs intra- and inter-fraction motion uncertainties and patient-specific factors (height and weight) was determined using a Spearman's test (data not shown). No correlation was found between motion uncertainties and patient-specific factors. Despite the use of non-parametric statistical tests considering the small number of patients included in each subgroup ($n<10$), a larger patient cohort is needed to confirm the results of the statistical significance between motion uncertainties and the use of GA, nephrectomy side and patient-specific factors.

Furthermore, patient set-up uncertainties due to patient position variations were found to be small in this study and thus considered negligible when online CBCT imaging is employed and patients are immobilized supine in a vacuum mattress. Similar observations were done by (Beltran et al., 2010) regarding the intra-fraction patient set-up uncertainty. They reported an average uncertainty smaller than 0.5 mm (vs. $\leq$ 0.1 mm) and Σ and σ smaller than 1 mm (vs. $\leq$ 0.8 mm). For the evaluation of the intra-fraction patient set-up uncertainty, it must be noted that the post-treatment CBCT scans were only acquired for the first fractions and using a modified CBCT protocol compared to adults in order to reduce the dose given to the patient without compromising the image guidance accuracy. As a result of the negligible patient set-up intra-fraction uncertainty observed, post-treatment CBCTs are currently not acquired at our department anymore.

The simultaneous assessment of both intra- and inter-fraction imaging data enabled an accurate estimation of the motion and patient set-up uncertainties during radiotherapy treatment of WT patients undergoing flank irradiation. For the motion uncertainties, due to the wide distribution of the Σ and σ (range [0.2 ; 2.4] mm) and due to the large number of outliers found among the considered patient population in all orthogonal directions, the use of patient-specific and anisotropic target volume safety margins is recommended. The use of personalized target margins can limit the volume of healthy tissue included in the target volume allowing for the reduction of the risk of chronic toxicity. Assuming that children are at particular predisposition to develop radiation-induced late effects as they are more sensitive to radiation than adults (Hall and Phill, 2006), we advise the acquisition of both 4D-CT during preparation and pre-treatment CBCT images during delivery for the assessment of the treatment margins. The 4D-CT images should be used for the definition of an individualized ITV to account for the breathing uncertainty.

Moreover, TB motion should be assessed using the surgical clips displacements. Without the use of surgical clips, no estimation of the TB motion uncertainty using CT and CBCT images for WT patients would be possible. Furthermore, daily pre-treatment CBCTs should be acquired for both online correction of the patient position and visualization of eventual OARs displacements or some rare deformations with respect to the TB. Despite CBCT imaging offers adequate bone contrast for patient positioning, the visualization of the target and OARs might be however compromised due to the poor soft-tissue contrast. MRI-guided treatment systems currently under development (Lagendijk et al., 2016), which provide superior soft-tissue contrast allowing for adaptive radiotherapy regimes, are showing to be a great promise for optimal IGRT in the pediatric population, for whom there is particular concern to avoid potential radiation-induced late effects (Hess et al., 2016).

Loco-regional control rates exceeding 95% with radiotherapy doses between 14.4 and 25.2 Gy in children with WT should force clinicians towards better sparing of the OARs (Pritchard-Jones et al., 2015). Taking into account that individual OARs motion uncertainties could go up to 10 mm, in addition to patient-specific target safety margins, to ensure an optimal sparing we recommend the use of patient-specific and anisotropic OARs safety margins. These margins should be individualized based on the 4D-CT and daily CBCT images if an adaptation is demanded.

To the authors' knowledge, this is the first study evaluating both intra- and inter-fraction motion uncertainties of the OARs and TB, demarcated by surgical clips, and patient set-up uncertainties for a homogeneous disease patient cohort at a single institute. The gold standard for WT patients undergoing flank irradiation consists of using 10 mm margin around the CTV as recommended by the international SIOP-2001 protocol (de Kraker et al., 2001). As this protocol was developed long before IGRT was implemented and as new radiotherapy approaches are under development, knowledge on the potential treatment uncertainties for WT patients is essential. Facing the limited average motion uncertainties, the negligible patient set-up uncertainties and the use of individualized margins

based on the imaging modalities, such as 4D-CT and CBCT, the use of smaller safety margins than the one suggested by the SIOP-2001 protocol may be achieved. However, for an accurate estimation of a PTV expansion to use for this patient category, an estimation of the delineation uncertainty and a larger patient cohort would be necessary. Future studies should be focused on evaluating the effect of the use of patient-specific and reduced margins on the OARs doses using conformal IGRT techniques and novel techniques such as IMPT and MRI-guided treatments for abdominal pediatric cancer.

2.5 Conclusion

This study comprises an overview of the uncertainties during radiotherapy treatment for a homogeneous group of children with WT undergoing flank irradiation. With the purpose of reducing safety margins, IGRT techniques are highly recommended for these patients. Imaging data collected before and during radiotherapy demonstrated limited TB and OARs motion and negligible patient set-up uncertainties. For the motion uncertainties, due to the wide distribution of the Σ and σ found and due to the existence of a large number of outliers among the considered patient population in all orthogonal directions, the use of patient-specific and anisotropic safety margins can be recommended for both target and OARs when having available 4D-CT and daily CBCT information.

2.6 Supplementary Material

Table 2.3 Patient, treatment and imaging characteristics. *Abbreviations: F= female; M= male; NEF= nephrectomy; Fra= fractions; P= preparation; T= treatment; N= no; Y= yes; Max= maximum; Min= minimum; Insp= inspiration; Exp= expiration.*

Patient Characteristics						Treatment Characteristics					Imaging Characteristics			
									Anesthesia		No CBCTs		4D-CT	
No	Sex	Age (years)	Height (cm)	Weight (kg)	CTV (cm^3)	NEF side	Dose (Gy)	No Fra	P	T	pre-CBCT	post-CBCT	Max Insp	Max Exp
1	F	8	128	23	389	left	25.2	14	N	N	14	5	0%	50%
2	M	4	112	17	526	right	25.2	14	Y	Y	14	5	0%	60%
3	F	4	118	18	136	left	25.2	14	Y	Y	14	4	90%	60%
4	F	5	117	19	53	right	14.4	8	N	N	8	3	0%	60%
5	F	6	113	19	125	right	14.4	8	N	N	8	3	0%	60%
6	M	6	125	21	30	left	14.4	8	N	N	8	3	0%	70%
7	F	5	113	20	49	right	14.4	8	Y	N	8	3	0%	60%
8	M	4	95	13	64	left	14.4	8	Y	N	8	3	90%	50%
9	M	4	98	15	151	right	14.4	8	Y	Y	8	3	0%	50%
10	F	4	96	14	147	left	14.4	8	Y	N	8	3	10%	70%
11	M	4	116	20	44	left	14.4	8	Y	N	8	3	90%	60%
12	F	3	92	14	93	right	14.4	8	Y	Y	8	3	0%	60%
13	M	3	94	15	97	left	14.4	8	N	N	8	3	0%	50%
14	F	2	86	11	53	right	14.4	8	Y	Y	8	3	0%	60%
15	F	1	77	11	52	right	14.4	8	Y	Y	8	3	0%	60%

CHAPTER 3

Potential benefit of MRI-guided IMRT for flank irradiation in pediatric patients with Wilms' tumor

The following chapter is based on:

Guerreiro F, Seravalli E, Janssens GO, van den Heuvel-Eibrink MM, Lagendijk JJW and Raaymakers BW 2019 Potential benefit of MRI-guided IMRT for flank irradiation in pediatric patients with Wilms' tumor. *Acta Oncol.* 58(2):243-50.

Abstract

Background and Purpose: Flank irradiation for Wilms' tumor (WT) is currently performed at our institute using a cone-beam computed tomography (CBCT)-guided volumetric modulated arc ($VMAT_{CBCT}$) workflow. By adding real-time magnetic resonance imaging (MRI) guidance to the treatment, safety margins might be reduced. The purpose of this study was to quantify the potential reduction of the planning target volume (PTV) margin and its dosimetric impact when using an MRI-guided intensity-modulated radiation therapy ($IMRT_{MRI}$) workflow compared to the $VMAT_{CBCT}$ workflow.

Material and Methods: 4D-CT, MR and CBCT images acquired during preparation and treatment of 15 WT patients, were used to estimate the geometric, motion and patient set-up systematic (Σ) and random (σ) errors for both $VMAT_{CBCT}$ and $IMRT_{MRI}$ workflows. The mean PTV (PTV_{mean}) expansion was calculated using the van Herk formula. Treatment plans were generated using five margin scenarios (PTV_{mean} ± 0, 1 and 2 mm). Furthermore, the $IMRT_{MRI}$ plans were optimized with a 1.5 T transverse magnetic field turned-on to realistically model an MRI-guided treatment. Plans were evaluated using dose-volume statistics ($p<0.01$, Wilcoxon).

Results: Analysis of Σ and σ errors resulted in a PTV_{mean} of 5 mm for the $VMAT_{CBCT}$ and 3 mm for the $IMRT_{MRI}$ workflows in each orthogonal direction. Target coverage was unaffected by the margin decrease with a mean $V_{95\%}$=100% for all margin scenarios. For the PTV_{mean}, an average reduction of the mean dose to the organs at risk (OARs) was achieved with $IMRT_{MRI}$ compared to $VMAT_{CBCT}$: 3.4 ± 2.4 % ($p<0.01$) for the kidney, 3.4 ± 2.1 % ($p<0.01$) for the liver, 2.8 ± 3.0 % ($p<0.01$) for the spleen and 4.9 ± 3.8 % ($p<0.01$) for the pancreas, respectively.

Conclusions: Imaging data in children with WT demonstrated that the PTV margin could be reduced isotropically by 2 mm with the $IMRT_{MRI}$ compared to the $VMAT_{CBCT}$ workflow. The former results in a dose reduction to the OARs while maintaining the target coverage.

3.1 Introduction

Wilms' tumor (WT), also known as nephroblastoma, belongs to the most frequent retroperitoneal tumors during childhood. Since the first successful protocols were launched in the seventies, reduction of the treatment intensity has become feasible for the majority of the patients, while the survival rate exceeds now 90% (Pastore et al., 2006; Pritchard-Jones et al., 2015). Nevertheless, the sub-group of patients with a higher probability for loco-regional failure (~ 20%) that need irradiation at the site of the primary tumor (Jereb et al., 1994) is at risk for potential radiation-induced late effects such as renal failure, scoliosis and metabolic syndrome (Rate et al., 1991; Ritchey et al., 1996; Sasso et al., 2010; van Waas et al., 2012). In addition, studies have shown an increased risk of secondary cancer occurring within the radiation field after radiotherapy treatment (Taylor et al., 2008; Breslow et al., 2010).

Conventionally, two ventro-dorsal opposing photon fields have been used to cover the flank target volume for decades (Gross and Neuhauser, 1950; de Kraker et al., 2001). A known disadvantage of this technique is the large volume of normal tissue (NT) receiving a radiotherapy dose comparable to the target dose. However, highly conformal image-guided radiation therapy (IGRT) delivery techniques, such as intensity-modulated radiation therapy (IMRT), volumetric modulated arc therapy (VMAT) and intensity-modulated proton therapy (IMPT), enable us to deliver steep dose gradients to the target and have therefore the potential to reduce the dose to the surrounding NT (Hillbrand et al., 2008; Schaffer et al., 2011; Bosarge et al., 2016; Vogel et al., 2017). Based on single institutional experience and international trials (de Kraker et al., 2001; van den Heuvel-Eibrink et al., 2017), at the radiotherapy department of the University Medical Center Utrecht (UMCU), WT patients undergoing flank irradiation are currently treated with VMAT.

To guarantee tumor bed (TB) coverage and organs at risk (OARs) sparing, safety margins are employed during treatment planning to compensate for uncertainties related to the location of these structures. Most of IGRT treatments are currently performed using online cone-beam computed tomography (CBCT) guidance (Jaffray et al., 2012). Despite CBCT imaging offers adequate bone contrast for patient positioning prior treatment, the exact position and deformation of the TB and OARs might go undetected due to the poor soft-tissue contrast. Magnetic resonance imaging (MRI) yields superior soft-tissue visualization allowing for the identification of organ motion and physiological changes without patient radiation burden (Lagendijk et al., 2014). In the last few years, MRI-guided systems for real-time IGRT (Mutic and Dempsey, 2014; Raaymakers et al., 2017) have been introduced into the clinic with the goal of reducing treatment safety margins, due to the better soft-tissue visualization and online plan adaptation. These systems seem promising in the pediatric population, for whom there is a particular concern for NT sparing to minimize the risk of radiation-induced complications.

Given the prospective advantages of MRI-guided treatments and considering the availability of an MRI-linear accelerator (MRI-linac) system using IMRT delivery at the UMCU, the aim of this study was to assess the potential benefit of using the MRI-guided IMRT ($IMRT_{MRI}$) workflow instead of the clinical CBCT-guided VMAT ($VMAT_{CBCT}$) workflow to treat WT patients. Both the potential margin reduction of the planning target volume (PTV) and its dosimetric impact were evaluated.

3.2 Materials and Methods

3.2.1 Patients & imaging characteristics

After institutional review board approval (WAG/mb/17/008865), 15 consecutive patients (mean age: 3 ; range 1 - 8 years) with WT undergoing flank irradiation between April 2015 and October 2016 at the radiotherapy department of UMCU were included in this study (*Table 3.1*). After induction chemotherapy, a nephrectomy was performed. During surgery, four titanium clips were placed at the superior, lateral, medial and inferior borders of the tumor.

For treatment preparation, post-operative four-dimensional CT (4D-CT) and MRI scans were taken for each patient in treatment position (*Supplementary Material, section 3.6*). The 4D-CT images were obtained using a 16-, 40-, or 64- channel detector scanner (Brilliance, Philips Medical Systems, Best, The Netherlands) with a 3 mm slice thickness. Each respiratory cycle during free-breathing was captured as a series of ten equally spaced traces. Furthermore, the planning-CT was obtained by taking the pixel-by-pixel average of the ten phases of the 4D-CT.

MRI scans (T1- (T1w) and T2-weighted (T2w)) were acquired using a 1.5 T Philips Achieva MRI scanner (Philips Medical Systems, Best, The Netherlands). The T1w-MR images were obtained using a transversal gradient echo sequence with fat saturation and a 1.5 mm slice thickness. The scans were repeated following the administration of gadolinium contrast agent. The T2w-MR images were acquired using a turbo spin echo sequence with a 0.8 mm slice thickness. The planning-CT and MR images were rigidly registered using an in-house software (Bol et al., 2009).

Patient repositioning during treatment was performed by acquiring daily pre-treatment CBCTs using the Elekta XVI 4.5.1 on-board CBCT imaging system (Elekta, Stockholm, Sweden) (*Supplementary Material, section 3.6*). Patient position was corrected online using the automated treatment table movement. For every other fraction, post-treatment CBCTs were acquired for each patient as standard of care (**chapter 2**). All pre- and post-treatment CBCT images were registered to the planning-CT using the automated rigid registration algorithm available clinically on the XVI software. A clipbox defined around the target and the vertebra volume was used to guide the registration.

Table 3.1 Patient, tumor, treatment and imaging characteristics. Tumor characteristics according to International Society of Paediatric Oncology (SIOP). *Abbreviations: HR= high risk group; IR= intermediate risk group; SM+= positive section margins; LN+= lymph nodes involvement; Fra= fractions; NEF= nephrectomy.*

Patient Characteristics			**TumorCharacteristics**	**Treatment Characteristics**					**Imaging Characteristics**		
No	Sex	Age (years)	Classification (risk group ; stage (SM+/LN+)	CTV (cm^3)	NEF side	Dose (Gy)	No Fra	Anesthesia	No of CBCTs		No of MRIs
									pre-CBCT	post-CBCT	(T1w- & T2-w)
1	F	8	blastemal type (HR); stage III (SM+)	389	left	25.2	14	N	14	5	3
2	F	4	blastemal type (HR); stage III (SM+)	527	right	25.2	14	Y	14	4	3
3	F	6	mixed type (IR); stage III (SM+)	125	right	14.4	8	N	8	3	3
4	F	5	stromal type (IR); stage III (SM+, LN+)	49	right	14.4	8	N	8	3	3
5	F	4	mixed type (IR); stage III (SM+)	151	right	14.4	8	Y	8	3	3
6	F	4	regressive type (IR); stage III (LN+)	44	left	14.4	8	N	8	3	3
7	F	4	regressive type (IR); stage III (SM+)	147	left	14.4	8	N	8	3	3
8	M	4	mixed type (IR); stage III (LN+)	64	left	14.4	8	N	8	3	3
9	M	3	regressive type (IR); stage III (SM+,LN+)	97	left	14.4	8	N	8	3	3
10	F	3	regressive type (IR); stage III (SM+,LN+)	93	right	14.4	8	Y	8	3	3
11	F	2	regressive type (IR); stage III (SM+)	53	right	14.4	8	Y	8	3	3
12	M	2	mixed type (IR); stage III (SM+)	136	left	14.4	8	Y	8	3	3
13	M	1	regressive type (IR); stage III (SM+)	32	right	14.4	8	Y	8	3	3
14	M	1	mixed type (IR); stage III (SM+)	30	left	14.4	8	N	8	3	3
15	M	1	stromal type (IR); stage III (SM+, LN+)	52	right	14.4	8	Y	8	3	3

3.2.2 Target volumes and OARs definition

The gross tumor volume (GTV) and OARs were delineated, according to the department protocol, by one radiation oncologist. The GTV was defined using the MRI scans and consisted of the TB and the lymph nodes, if applicable. For treatment planning purposes, the GTV was rigidly copied to the planning-CT. The clinical target volume (CTV) was created by expanding the GTV by 10 mm (de Kraker et al., 2001). To account for the uncertainty introduced by patient breathing, an individual and direction-specific internal target volume (ITV) was defined by measuring the surgical clips center of mass (CoM) displacements between the maximum expiration and inspiration phases of the 4D-CT images (**chapter 2**). OARs were contoured using the planning-CT.

3.2.3 PTV_{mean} determination

Both $VMAT_{CBCT}$ and $IMRT_{MRI}$ plans were optimized using the PTV concept to account for the geometric accuracy of the treatment chain, inter-fraction motion and patient set-up uncertainties. A flowchart with all the steps of the uncertainty analysis is represented in *Figure 3.1.* For more details on the methodology please see **chapter 2**. A mean PTV (PTV_{mean}) expansion defined around the clinical ITV was calculated per workflow.

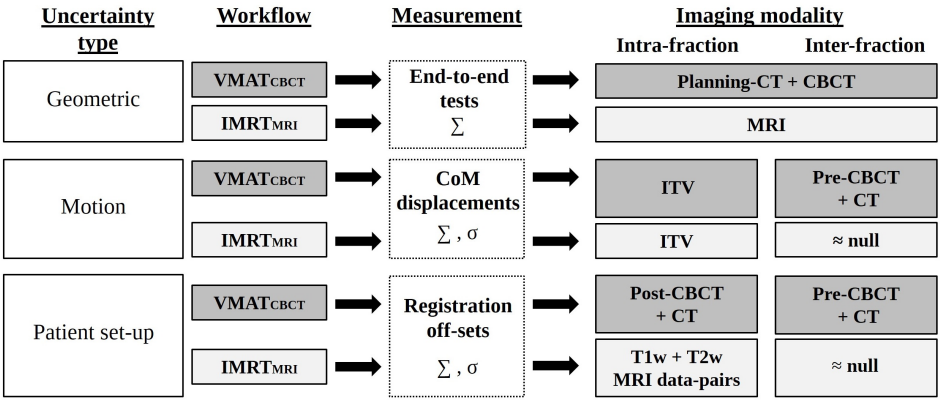

Figure 3.1 Stages of the uncertainty analysis and imaging modalities used for the PTV_{mean} estimation for the two considered workflows: the clinical $VMAT_{CBCT}$ and the prospective $IMRT_{MRI}$.

3.2.3.1 Geometric accuracy

For the $VMAT_{CBCT}$ workflow, the overall geometric accuracy of the treatment chain, excluding patient-specific factors, was estimated by calculating the displacement of measured and planned dose profiles obtained using a phantom consisting of two Perspex slabs in which a piece of Gafchromic EBT3 film (Ashland ISP, Wayne, NJ) was inserted (Wopereis et al., 2015). The phantom underwent all steps of the patient treatment chain.

For the $IMRT_{MRI}$ workflow, the overall geometric accuracy was estimated by measuring the geometric fidelity and the geometric in vivo delivery accuracy of treatments performed on the MRI-linac. For the geometric fidelity, the distortions of the MRI protocols were measured using a diameter spherical volume of 300 mm and a vendor three-dimensional (3D) geometric quality assurance fidelity phantom (Philips, Best, The Netherlands) (Tijssen et al., 2017). The geometric in vivo delivery accuracy was validated by calculating the bone directional shift between the portal images of the IMRT segments and the MRI-based calculated projections (Raaymakers et al., 2017). MRI-based projections were calculated by deformably registering the planning-CT to the MRI of the patient in treatment position. The estimated geometric fidelity and in vivo delivery accuracy uncertainties were combined in quadrature.

3.2.3.2 Motion uncertainties

Inter-fraction motion uncertainties were related to the TB motion between treatment fractions. For the $VMAT_{CBCT}$ workflow, the inter-fraction uncertainty was assessed by measuring the clips CoM displacements between the pre-treatment CBCTs and the planning-CT, used as reference (**chapter 2**). For the $IMRT_{MRI}$ workflow, the inter-fraction uncertainty was assumed to be null as online daily re-planning would be available for this workflow.

3.2.3.3 Patient set-up uncertainties

Patient set-up uncertainties were related to the patient movement during and between treatment fractions. For the $VMAT_{CBCT}$ workflow, the intra- and inter-fraction uncertainties were calculated by measuring the clinical rigid registration off-sets between the post-treatment and the pre-treatment CBCTs (*Table 3.1*) and the planning-CT, respectively (**chapter 2**). For the $IMRT_{MRI}$ workflow, the intra-fraction uncertainty was calculated by measuring the rigid registration off-sets between the T1w-MRI scans (pre- and post-enhanced), acquired with a mean interval time of 25 min, and the T2w-MRI and the post-enhanced T1w-MRI scans, acquired with a mean interval time of 33 min (*Table 3.1*) (Bol et al., 2009). The mean interval time between the MRI acquisitions was within the range of current clinical MRI-guided workflows (Fischer-Valuck et al., 2017). The inter-fraction uncertainty was assumed to be null as online daily re-planning would be available for this workflow.

Finally, systematic (Σ) and random (σ) errors were calculated for each uncertainty type (van Herk et al., 2000; van Herk, 2004). For the inter-fraction motion uncertainty in the $VMAT_{CBCT}$ workflow, Σ and σ errors were calculated for each clip. The Σ and σ errors computed among the four clips were summed in quadrature and further used for the margin estimation. For both workflows, the PTV_{mean} was obtained using the van Herk formula ($2.5\Sigma + 0.7\sigma$) (van Herk et al., 2000).

3.2.4 Treatment planning

Both $VMAT_{CBCT}$ and $IMRT_{MRI}$ plans were calculated on a clinical 3D treatment planning system (TPS) (Monaco, Elekta, Stockholm, Sweden) using the clinical delineations. $VMAT_{CBCT}$ plans were based on a 10 MV full-arc and $IMRT_{MRI}$ plans on seven 7 MV flattening filter free (FFF) co-planar beams (30, 75, 135, 181, 225, 285, 330 degrees) applied to the same isocenter. For more details regarding the beam characterization of the MRI-linac we refer to (Woodings et al., 2018). For the $IMRT_{MRI}$ plans, optimization was done with a 1.5 T magnetic field turned-on to realistically simulate an MRI-linac treatment (Raaymakers et al., 2017). The total prescribed dose ranged from 14.4 to 25.2 Gy (*Table 3.1*).

To reduce the risk of asymmetric skeletal growth (Rate et al., 1991), a homogeneous dose was aimed for the vertebra volume adjacent to the PTV. According to our clinical practice, both $VMAT_{CBCT}$ and $IMRT_{MRI}$ plans needed to fulfill the $V_{70-80\%}$>95-98% constraint on the vertebra to achieve the dose homogeneity. For each patient and workflow, plans were generated using five ITV-PTV margin scenarios: PTV_{mean} ± 0, 1 and 2 mm, to quantify the dosimetric differences if the employed margin would differ from the estimated PTV_{mean}. All plans, were optimized to achieve the same level of PTV coverage: $V_{95\%}$>99%.

To discard the possibility that differences in beam energy, beam configuration and delivery technique could influence the results, for both $VMAT_{CBCT}$ and $IMRT_{MRI}$ plans the following scenarios were considered: (1) $VMAT_{CBCT}$ plans optimized using the same PTV margin (PTV_{mean}), the same beam configuration (clinical linac) and different beam energies (6 and 10 MV); (2) IMRT plans optimized using the same PTV margin (PTV_{mean}) and the beam configuration of the clinical linac (10 MV) and the MRI-linac (7 MV); (3) $VMAT_{CBCT}$ and IMRT plans optimized using the same PTV margin (3 mm), the same beam energy (10 MV) and the same beam configuration (clinical linac).

3.2.5 Dose distribution evaluation

Mean dose (D_{mean}) and dose-volume histogram (DVH) metrics were computed to assess the ITV coverage, OARs and NT sparing. For the ITV, $D_{98\%}$, D_{mean}, $D_{2\%}$ and $V_{95\%}$ were calculated. For the OARs, D_{mean} and $D_{2\%}$were computed. For the NT, the $V_{95\%}$, V_{2Gy}, and the NT integral dose (NTID) were calculated.

The NTID was defined as (D'Souza and Rosen, 2003):

$$\text{NTID [J]} = D_{mean} V_{NT} \rho$$

, where V_{NT} is the body volume subtracting the ITV volume and ρ the body density which was assumed to be uniform (1 g/cm^3). For the statistical analysis, a Wilcoxon test ($p<0.01$) was performed between the $VMAT_{CBCT}$ and $IMRT_{MRI}$ plans optimized using the PTV_{mean}.

3.3 Results

The calculated Σ and σ errors for each uncertainty type are shown in *Table 3.2.* The estimated PTV_{mean} was 5 mm for the $VMAT_{CBCT}$ and 3 mm for the $IMRT_{MRI}$ workflows in each orthogonal direction.

Table 3.2 Calculated systematic (Σ) and random (σ) errors for each uncertainty and the PTV_{mean} for both $VMAT_{CBCT}$ and $IMRT_{MRI}$ workflows. *Abbreviations: LR= left-right; AP= anterior-posterior; CC= craniocaudal.*

Uncertainty		Error (mm)	$VMAT_{CBCT}$			$IMRT_{MRI}$		
			LR	**AP**	**CC**	**LR**	**AP**	**CC**
Geometric		Σ	0.5	0.5	0.5	1.0	1.0	1.0
Motion	**Inter-fraction**	Σ	1.3	1.5	1.5	0.0	0.0	0.0
		σ	1.2	1.4	1.8	0.0	0.0	0.0
Patient set-up	**Inter-fraction**	Σ	0.1	0.2	0.1	0.0	0.0	0.0
		σ	0.0	0.0	0.0	0.0	0.0	0.0
	Intra-fraction	Σ	0.5	0.4	0.4	0.4	0.5	0.6
		σ	0.7	0.8	0.8	0.4	0.4	0.6
Quadratic Sum		Σ	1.5	1.7	1.6	1.1	1.1	1.2
		σ	1.4	1.6	2.0	0.4	0.4	0.6
ITV-PTV_{mean} margin		$2.5\Sigma + 0.7\sigma$	4.6	5.3	5.3	3.1	3.2	3.4
		Final	5.0	5.0	5.0	3.0	3.0	3.0

For both workflows, the ITV coverage was unaffected by the margin decrease with a mean $V_{95\%}$ of 100% for all scenarios (*Table 3.3*). Furthermore, D_{mean} of the OARs progressively decreased along with the margin (*Table 3.3, Figure 3.2*). The mean reduction of the OARs D_{mean} between the largest and the smallest margin scenarios was down to 9% for the $VMAT_{CBCT}$ (range [0.3 ; 2.4] Gy) and down to 10% for the $IMRT_{MRI}$ (range [0.1 ; 2.9] Gy) workflows. In the boxplots (*Figure 3.2*), a large inter-patient variability in all margin scenarios can be observed, which was dependent on the TB location (*Supplementary Material, section 3.6*). For the PTV_{mean}, a mean reduction of the D_{mean} to the OARs (range [0.1 ; 2.3] Gy) was achieved with the $IMRT_{MRI}$ compared to the $VMAT_{CBCT}$ workflow: 3.4 ± 2.4 % ($p<0.01$) for the kidney, 3.4 ± 2.1 % ($p<0.01$) for the liver, 2.8 ± 3.0 % ($p<0.01$) for the spleen and 4.9 ± 3.8 % ($p<0.01$) for the pancreas, respectively.

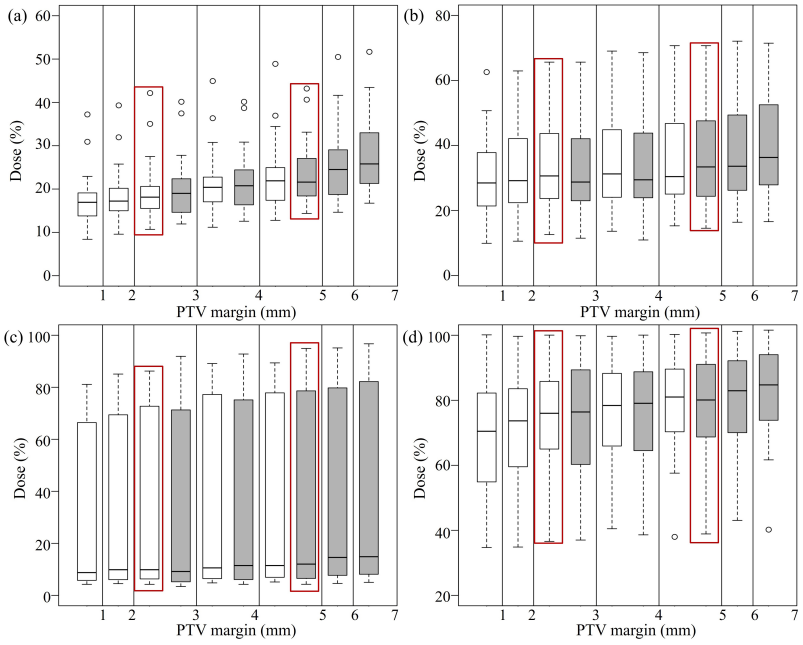

Figure 3.2 Boxplots of the D_{mean} to the (a) kidney (b) liver (c) spleen and (d) pancreas for both $VMAT_{CBCT}$ (in gray) and $IMRT_{MRI}$ (in white) workflows and all margin scenarios. Plans optimized with the PTV_{mean} are indicated by the red boxes. Note that the y-axes differ in range.

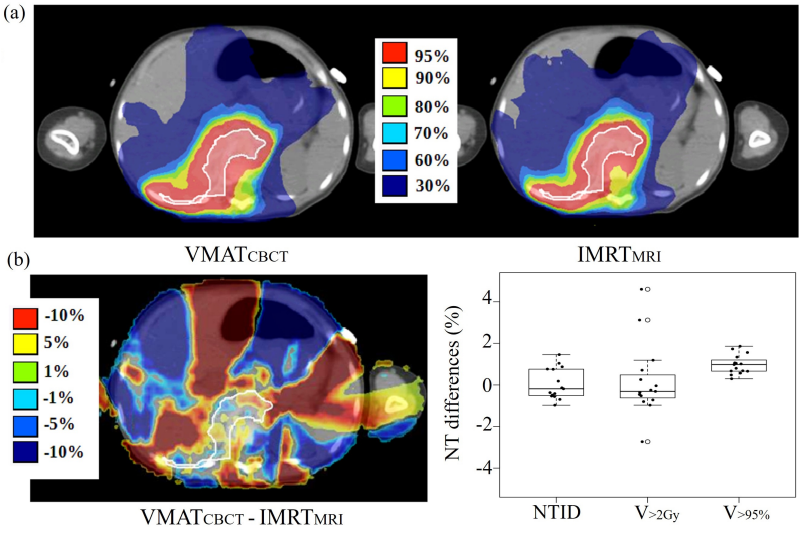

Figure 3.3 Dose comparison of a transversal planning-CT slice of one patient (a) and dose, NTID and NT volume differences (b) between the $VMAT_{CBCT}$ and $IMRT_{MRI}$ plans optimized with the PTV_{mean}. The ITV is shaded in white (prescribed dose = 14.4 Gy).

In addition, a decrease in the NT dose was obtained with the margin reduction (*Table 3.3*). The mean reduction of the NTID between the largest and the smallest margin scenarios was 2.8 ± 1.3 % for the $VMAT_{CBCT}$ (range [1.4 ; 6.7] %) and 2.3 ± 0.9 % for the $IMRT_{MRI}$ (range [1.1 ; 4.0] %) workflows. For the PTV_{mean}, a mean reduction of 0.1 ± 0.7 % (range [-1.0 ; 1.5] %, p=0.9) for the NTID, of 0.2 ± 1.8 % (range [-2.7 ; 4.6] %, p=0.6) for the V_{2Gy} and of 1.0 ± 0.5 % (range [0.3 ; 1.9] %, p<0.01) for the $V_{95\%}$ was achieved with the $IMRT_{MRI}$ compared to the $VMAT_{CBCT}$ workflow (*Figure 3.3*). For the same PTV expansion, the $VMAT_{CBCT}$ workflow denoted equal or even better NT sparing than the $IMRT_{MRI}$, in particular for the low dose region (V_{2Gy}).

Regarding the effect of different beam energies (1), beam configurations (2) and delivery techniques (3) on the final dose distributions, significant differences were only found for the NT dosimetric parameters (NTID and V_{2Gy}) in scenario (3) (*Supplementary Material, section 3.6*).

Table 3.3 DVH parameters and NTID results (%) per margin scenario for both $VMAT_{CBCT}$ and $IMRT_{MRI}$ workflows. Mean and standard deviation (SD) results are shown.

		(%)	Margin scenario				
			3 mm	**4 mm**	**5 mm**	**6 mm**	**7 mm**
$VMAT_{CBCT}$	**ITV**	$D_{98\%}$	98.3 ± 0.9	97.9 ± 0.7	98.5 ± 0.8	98.3 ± 0.7	98.3 ± 0.7
		D_{mean}	101.9 ± 1.0	101.7 ± 0.8	101.9 ± 0.7	102.0 ± 0.7	101.8 ± 0.8
		$D_{2\%}$	106.9 ± 1.6	106.7 ± 1.7	106.8 ± 1.4	107.1 ± 1.4	106.7 ± 1.8
	Kidney	D_{mean}	20.8 ± 8.4	22.2 ± 8.5	24.0 ± 9.0	26.0 ± 10.2	28.4 ± 10.2
		$D_{2\%}$	71.9 ± 20.4	75.5 ± 21.2	79.0 ± 20.9	81.3 ± 21.7	84.1 ± 21.5
	Liver	D_{mean}	33.8 ± 15.2	35.0 ± 15.6	37.0 ± 16.0	38.8 ± 15.9	40.6 ± 15.9
		$D_{2\%}$	87.7 ± 16.8	88.5 ± 16.6	90.5 ± 14.9	92.6 ± 13.6	93.4 ± 12.6
	Spleen	D_{mean}	34.3 ± 35.6	36.1 ± 36.5	37.5 ± 37.4	39.1 ± 37.6	40.6 ± 38.7
		$D_{2\%}$	57.5 ± 43.5	59.5 ± 42.7	60.5 ± 43.0	62.2 ± 42.1	62.9 ± 41.4
	Pancreas	D_{mean}	73.6 ± 18.7	76.3 ± 17.1	78.8 ± 17.1	80.8 ± 16.6	82.4 ± 17.1
		$D_{2\%}$	100.8 ± 8.1	100.7 ± 9.7	101.6 ± 9.6	102.2 ± 8.9	101.8 ± 10.2
	NT	$V_{95\%}$	2.7 ± 0.8	3.0 ± 1.1	3.7 ± 1.1	4.2 ± 1.3	4.8 ± 1.5
		V_{2Gy}	30.2 ± 8.8	30.8 ± 8.9	31.7 ± 8.9	32.3 ± 9.3	33.2 ± 9.7
		NTID	17.2 ± 4.1	17.7 ± 4.3	18.5 ± 4.5	19.1 ± 4.5	20.0 ± 5.0
			1 mm	**2 mm**	**3 mm**	**4 mm**	**5 mm**
$IMRT_{MRI}$	**ITV**	$D_{98\%}$	97.4 ± 0.8	97.8 ± 1.1	97.8 ± 0.9	97.9 ± 0.7	97.7 ± 0.7
		D_{mean}	101.5 ± 0.9	101.7 ± 1.1	101.7 ± 0.9	102.0 ± 0.7	101.7 ± 0.7
		$D_{2\%}$	106.5 ± 2.0	106.4 ± 1.7	106.7 ± 1.6	107.2 ± 1.1	106.8 ± 1.1
	Kidney	D_{mean}	18.1 ± 7.5	19.4 ± 7.7	20.6 ± 8.4	22.2 ± 8.8	23.8 ± 9.6
		$D_{2\%}$	65.7 ± 19.6	70.9 ± 19.1	73.6 ± 19.3	76.2 ± 20.8	79.6 ± 20.6
	Liver	D_{mean}	30.0 ± 14.0	32.1 ± 14.8	33.6 ± 14.7	34.9 ± 15.4	36.5 ± 16.5
		$D_{2\%}$	82.8 ± 19.6	84.7 ± 18.4	86.6 ± 16.9	87.9 ± 17.1	90.2 ± 14.6
	Spleen	D_{mean}	31.8 ± 32.5	33.3 ± 33.8	34.7 ± 34.7	36.4 ± 36.0	37.3 ± 36.5
		$D_{2\%}$	58.4 ± 41.3	59.6 ± 41.0	60.0 ± 41.8	61.2 ± 41.4	61.8 ± 42.0
	Pancreas	D_{mean}	68.3 ± 19.2	71.4 ± 18.5	73.9 ± 18.4	76.0 ± 17.7	78.6 ± 17.1
		$D_{2\%}$	98.6 ± 9.6	99.1 ± 10.8	100.0 ± 11.5	101.3 ± 10.7	101.3 ± 11.2
	NT	$V_{95\%}$	1.8 ± 0.7	2.3 ± 0.8	2.7 ± 0.9	3.2 ± 1.0	3.8 ± 1.1
		V_{2Gy}	30.5 ± 8.8	31.1 ± 9.0	31.5 ± 9.2	32.1 ± 9.0	32.5 ± 9.4
		NTID	17.3 ± 4.0	17.9 ± 4.2	18.5 ± 4.4	19.0 ± 4.4	19.6 ± 4.6

3.4 Discussion

The purpose of this study was to show the potential reduction of the PTV margin and its dosimetric impact on the target, OARs and NT when having available MRI-guidance in an $IMRT_{MRI}$ workflow compared to the clinical $VMAT_{CBCT}$ workflow. To the authors' knowledge this is the first study evaluating *in-silico* the dosimetric effect of treating pediatric patients on an MRI-linac system.

The PTV margin was defined taking into account the geometric accuracy of the treatment chain, inter-fraction motion and patient set-up uncertainties. An isotropic reduction of 2 mm was calculated when using the $IMRT_{MRI}$ instead of the $VMAT_{CBCT}$ workflow. Potential limitations of the uncertainty analysis presented in this work are (1) the assumption of null inter-fraction uncertainties for the $IMRT_{MRI}$ workflow and (2) the omission of the delineation uncertainty from the PTV margin recipe for both workflows.

For the $IMRT_{MRI}$ workflow, null inter-fraction uncertainties were assumed as with MRI-linac systems accurate online soft-tissue tracking and re-planning accounting for the daily anatomy is possible. Nevertheless, the authors are aware that the assumption of null inter-fraction uncertainties might be optimistic as errors resulting from the daily plan adjustments, with online re-optimization, or the estimation of Hounsfield units (HUs) from the MRI data, for the dose calculation purposes, might still occur. To minimize the online re-optimization uncertainties, a new TPS generation is being developed at the radiotherapy department of UMCU to compensate for intra- and inter-fraction patient anatomical changes in a fast online re-planning application (Kontaxis et al., 2015a,b, 2017a,b). For the conversion of MRI intensity values to HUs, there are currently two available methods reported in literature: (1) using the planning-CT deformably registered to the MRI (Acharya et al., 2016; Raaymakers et al., 2017; Fischer-Valuck et al., 2017) or (2) using a so-called synthetic or pseudo CT (Koivula et al., 2017; Tenhunen et al., 2018). For these two approaches, dosimetric inaccuracies were reported to be on average 0.4% (Raaymakers et al., 2017) and -0.6% (Koivula et al., 2017). A future investigation will focus on estimating uncertainties in calculating doses on synthetic CTs for pediatric patients with abdominal tumors.

Furthermore, as mentioned previously, the systematic target delineation uncertainty was not included in the PTV margin calculation in this study. Estimating inter-observer delineation variability for pediatric cases is even more difficult than for adults as a result of the small number of patients treated in each center, the broad spectrum of pediatric tumors, the lack of common guidelines and the individual patient's specific needs (Coles et al., 2003; Padovani et al., 2009). Thus, for the assessment of the exact PTV expansion, an estimation of the delineation uncertainty and a larger patient cohort would be necessary for both workflows. In addition for the $IMRT_{MRI}$ workflow, patient data obtained from clinical MRI-guided treatments would be required to estimate the magnitude of the inter-fraction uncertainties. Acquiring patient imaging data on a device which is not clinical yet is however not feasible for children due to the stringent ethical regulations associated to this patient group. Trying to overcome these limitations, treatment

planning was performed for five different margin scenarios in order to investigate the dosimetric differences between plans optimized with a smaller or larger PTV expansion (to ± 2 mm) than the estimated PTV_{mean}. For both workflows, mean differences between the largest and the smallest margin scenarios were up to 10% for the OARs D_{mean} and 3% for the NTID.

Additionally, instead of using an ITV, a better OARs and NT sparing might be achieved for the $IMRT_{MRI}$ workflow when including intra-fraction information, measured using 4D-MRI, into the online re-planning application. In literature, it was previously shown that with an online re-planning framework more conformal dose distributions were generated when compared to a treatment plan optimized using a safety margin (Kontaxis et al., 2017b). When using the $IMRT_{MRI}$ workflow, as the TB is potentially discernable on MRI for this patient group, uncertainties related to the estimation of the breathing motion by using surgical clips as surrogates would be eliminated.

In this work, we established that the ITV coverage was unaffected and the OARs D_{mean} and NTID progressively decreased along with a stepwise margin reduction. For the PTV_{mean}, significant differences in dosimetry were denoted between the two workflows. A decrease down to 16% on the D_{mean} to the OARs was found for the $IMRT_{MRI}$ workflow. Moreover, a large inter-patient variability in all margin scenarios was denoted, especially for the liver and spleen, which might indicate that some patients would benefit more from the $IMRT_{MRI}$ workflow than others, depending on the TB location. However, as a better sparing of the unique remaining kidney and pancreas are two of the most essential concerns during radiotherapy of WT patients due to the risk of developing renal complications and metabolic syndrome (Ritchey et al., 1996; van Waas et al., 2012), compromising the doses to the remaining organs can be allowed.

Besides the magnitude of the safety margin, the beam energy, the beam configuration and the chosen delivery technique might also impact the quality of the final dose distribution. This hypothesis was tested by optimizing both $VMAT_{CBCT}$ and $IMRT_{MRI}$ plans for different planning scenarios. Despite the MRI-linac system has geometric accuracy levels that are twice as large compared to clinical linacs, significant differences were only found for the NT in scenario (3). Thus, NT doses are affected by the delivery technique chosen and not by the beam energy and configuration. As VMAT requires less monitor units and shorter treatment delivery times than IMRT, a similar or even better NT sparing is expected with VMAT. In the future, improvements on the OARs and NT sparing might be achieved by implementing a VMAT delivery on the MRI-linac systems.

In this study, the reduction of the PTV margin and consequently the significant decrease of both OARs doses and NT volume receiving dose values comparable to the tumor dose ($V_{95\%}$), has been demonstrated when using the $IMRT_{MRI}$ instead of the clinical $VMAT_{CBCT}$ workflow. Assuming that children are at particular risk of developing radiation-induced late effects as they are more sensitive to radiation than adults (Hall and Phil, 2006), the $IMRT_{MRI}$ workflow would be more dosimetrically favorable than the current clinical $VMAT_{CBCT}$ workflow. However, as with any new technology, cost is a

potential limiting factor for the use of the MRI-linac and the authors are well aware that it is not yet widely available for clinical use.

Ideally, a comprehensive assessment of the follow-up chronic toxicity in pediatric patients is required to take advantage of all the state-of-the-art radiotherapy delivery techniques such as $VMAT_{CBCT}$, $IMRT_{MRI}$ and IMPT. With IMPT with pencil beam scanning there is hope of reducing both radiation-induced late effects and the chances of developing secondary cancer as a result of the unique dose-deposition pattern characterized by the minimal / zero exit dose (Hall and Phill, 2006; Hillbrand et al., 2008; Vogel et al., 2017). A future dosimetric investigation will focus on the potential benefits of treating pediatric patients with IMPT over the $IMRT_{MRI}$ and $VMAT_{CBCT}$ workflows.

3.5 Conclusion

To the authors' knowledge this is the first study evaluating *in-silico* the dosimetric effect of treating pediatric patients with MRI-guided routines when compared to the current clinical $VMAT_{CBCT}$ workflow. Imaging data collected during radiotherapy demonstrated that with the $IMRT_{MRI}$ workflow the PTV margin could be reduced isotropically by 2 mm. Furthermore, the $IMRT_{MRI}$ workflow reduces the doses to the OARs and NT while maintaining the target coverage compared to the $VMAT_{CBCT}$ treatments.

3.6 Supplementary Material

Table 3.4 DVH parameters results (%) for both $VMAT_{CBCT}$ and $IMRT_{MRI}$ workflows for plans optimized with the PTV_{mean}. Results are divided per each workflow according to the patient nephrectomy side. Significance difference between groups was tested using a Mann-Whitney test (p<0.01, in bold).

	(%)		nephrectomy side		
			left (n=7)	right (n=8)	(p<0.01)
Kidney	D_{mean}	$VMAT_{CBCT}$	25.3 ± 8.4	23.2 ± 10.6	0.39
		$IMRT_{MRI}$	21.7 ± 7.1	19.8 ± 10.5	0.39
	$D_{2\%}$	$VMAT_{CBCT}$	85.6 ± 15.2	70.3 ± 25.0	0.33
		$IMRT_{MRI}$	79.4 ± 16.0	66.7 ± 22.5	0.28
Liver	D_{mean}	$VMAT_{CBCT}$	26.3 ± 8.6	45.9 ± 16.3	**5.90E-3**
		$IMRT_{MRI}$	23.7 ± 7.2	42.0 ± 15.4	**9.30E-3**
	$D_{2\%}$	$VMAT_{CBCT}$	77.8 ± 12.4	101.8 ± 1.6	**3.10E-4**
		$IMRT_{MRI}$	72.3 ± 11.6	101.7 ± 2.7	**3.10E-4**
Spleen	D_{mean}	$VMAT_{CBCT}$	60.6 ± 33.9	7.3 ± 3.2	0.02
		$IMRT_{MRI}$	55.9 ± 21.5	6.6 ± 2.0	0.02
	$D_{2\%}$	$VMAT_{CBCT}$	91.9 ± 33.2	22.9 ± 9.5	0.02
		$IMRT_{MRI}$	91.3 ± 30.3	22.5 ± 7.9	**9.30E-3**
Pancreas	D_{mean}	$VMAT_{CBCT}$	88.7 ± 7.6	65.8 ± 15.2	0.04
		$IMRT_{MRI}$	84.3 ± 7.5	59.8 ± 16.2	0.02
	$D_{2\%}$	$VMAT_{CBCT}$	105.0 ± 3.5	97.9 ± 13.1	0.22
		$IMRT_{MRI}$	103.9 ± 2.7	95.5 ± 16.0	0.05

The $VMAT_{CBCT}$ plans were optimized using a 10 MV beam as standard of practice while $IMRT_{MRI}$ plans were restricted by the specific beam configuration of the MRI-linac system (7 MV FFF beam). To discard the possibility that differences in the beam energy, the beam configuration and the delivery technique could influence the final dose distributions, the following scenarios were considered:

1. $VMAT_{CBCT}$ with a 6 MV beam vs. $VMAT_{CBCT}$ with a 10 MV beam. Plans were optimized using the same PTV margin (PTV_{mean}, 5 mm) and using the beam configuration of the clinical linac with different beam energies (*Table 3.5*).

2. $IMRT_{MRI}$ with a 7 MV beam vs. IMRT with a 10 MV beam. Plans were optimized using the same PTV margin (PTV_{mean}, 3 mm) and using the beam configuration of the MRI-linac and of the clinical linac (*Table 3.6*).

3. $VMAT_{CBCT}$ with a 10 MV beam vs. IMRT with a 10 MV beam. Plans were optimized using the same PTV margin (3 mm) and using the same beam configuration and energy (*Table 3.7*).

Table 3.5 DVH and NTID results (%) for $VMAT_{CBCT}$ plans optimized using the PTV_{mean} (5 mm), the same beam configuration and different beam energies. Mean and standard deviation (SD) results are shown. ΔD denotes the difference between plans. Significance difference between plans was tested using a Wilcoxon test (p<0.01).

	(%)	$VMAT_{CBCT}$ (6 MV)		$VMAT_{CBCT}$ (10 MV)		ΔD		
		mean	SD	mean	SD	mean	SD	(p<0.01)
ITV	$D_{98\%}$	98.4	0.9	98.5	0.8	-0.1	0.9	0.89
	D_{mean}	101.9	0.8	101.9	0.7	0.0	0.6	0.89
	$D_{2\%}$	106.8	1.6	106.8	1.4	0.0	0.8	0.61
Kidney	D_{mean}	24.0	8.1	24.0	9.0	0.0	1.9	0.59
	$D_{2\%}$	79.1	19.9	79.0	20.9	0.1	4.1	0.52
Liver	D_{mean}	36.6	14.6	37.0	16.0	-0.4	1.9	0.05
	$D_{2\%}$	90.7	14.4	90.5	14.9	0.2	1.6	0.95
Spleen	D_{mean}	37.5	37.3	37.5	37.4	0.0	0.8	0.05
	$D_{2\%}$	60.1	43.4	60.5	43.0	-0.4	2.6	0.95
Pancreas	D_{mean}	78.2	19.2	78.8	17.1	-0.6	2.4	0.22
	$D_{2\%}$	101.7	12.2	101.6	9.6	0.1	3.3	0.19
NT	$V_{95\%}$	3.9	1.2	3.7	1.1	0.3	0.3	0.61
	V_{2Gy}	31.3	8.7	31.7	8.9	-0.4	1.3	0.49
	NTID	18.7	4.5	18.5	4.5	0.2	0.7	0.25

Table 3.6 DVH and NTID results (%) for IMRT plans optimized using the PTV_{mean} (3 mm) and different beam configurations and energies. Mean and standard deviation (SD) results are shown. ΔD denotes the difference between plans. Significance difference between plans was tested using a Wilcoxon test (p<0.01).

	(%)	$IMRT_{MRI}$ (7 MV)		IMRT (10 MV)		ΔD		
		mean	SD	mean	SD	mean	SD	(p<0.01)
ITV	$D_{98\%}$	97.8	0.9	98.1	1.2	-0.4	0.5	0.05
	D_{mean}	101.7	0.9	102.0	0.9	-0.3	0.3	0.05
	$D_{2\%}$	106.7	1.6	106.9	1.6	-0.1	0.6	0.05
Kidney	D_{mean}	20.6	8.4	20.6	8.0	-0.1	1.0	1.00
	$D_{2\%}$	73.6	19.3	74.0	19.3	-0.3	4.4	0.81
Liver	D_{mean}	33.6	14.7	33.9	15.5	-0.3	1.1	0.30
	$D_{2\%}$	86.6	16.9	86.4	18.1	0.2	2.8	0.92
Spleen	D_{mean}	34.7	34.7	34.8	35.2	-0.2	1.0	0.30
	$D_{2\%}$	60.0	41.8	60.8	42.0	-0.8	2.7	0.92
Pancreas	D_{mean}	73.9	18.4	73.1	18.9	0.8	1.6	0.07
	$D_{2\%}$	100.0	11.5	99.9	10.3	0.1	1.9	0.63
NT	$V_{95\%}$	2.7	0.9	2.8	0.9	0.0	0.3	0.64
	V_{2Gy}	31.5	9.2	31.1	9.1	0.4	0.6	0.06
	NTID	18.5	4.4	18.2	4.3	0.3	0.3	0.05

Table 3.7 DVH and NTID results (%) for $VMAT_{CBCT}$ and IMRT plans optimized using the same PTV margin (3 mm) and the same beam configuration and energy. Mean and standard deviation (SD) results are shown. Δ*D* denotes the difference between plans. Significance difference between plans was tested using a Wilcoxon test (p<0.01, in bold).

	(%)	$VMAT_{CBCT}$ (10 MV)		IMRT (10 MV)		Δ*D*		
		mean	SD	mean	SD	mean	SD	(p<0.01)
ITV	$D_{98\%}$	98.3	0.9	98.1	1.2	0.1	1.2	0.46
	D_{mean}	101.9	1.0	102.0	0.9	-0.1	1.2	1.00
	$D_{2\%}$	106.9	1.6	106.9	1.6	0.1	1.8	0.87
Kidney	D_{mean}	20.8	8.4	20.6	8.0	0.2	1.8	0.66
	$D_{2\%}$	71.9	20.4	74.0	19.3	-2.1	6.7	0.13
Liver	D_{mean}	33.8	15.2	33.9	15.5	-0.1	2.3	0.80
	$D_{2\%}$	87.7	16.8	86.4	18.1	1.3	4.1	0.25
Spleen	D_{mean}	34.3	35.6	34.8	35.2	-0.5	1.8	0.05
	$D_{2\%}$	57.5	43.5	60.8	42.0	-3.3	4.1	**6.10E-4**
Pancreas	D_{mean}	73.6	18.7	73.1	18.9	0.5	3.0	0.36
	$D_{2\%}$	100.8	8.1	99.9	10.3	0.9	3.2	0.21
NT	$V_{95\%}$	2.7	0.8	2.8	0.9	-0.1	0.5	0.36
	V_{2Gy}	30.2	8.8	31.1	9.1	-0.9	1.0	**3.00E-3**
	NTID	17.2	4.1	18.2	4.3	-1.0	0.8	**9.00E-3**

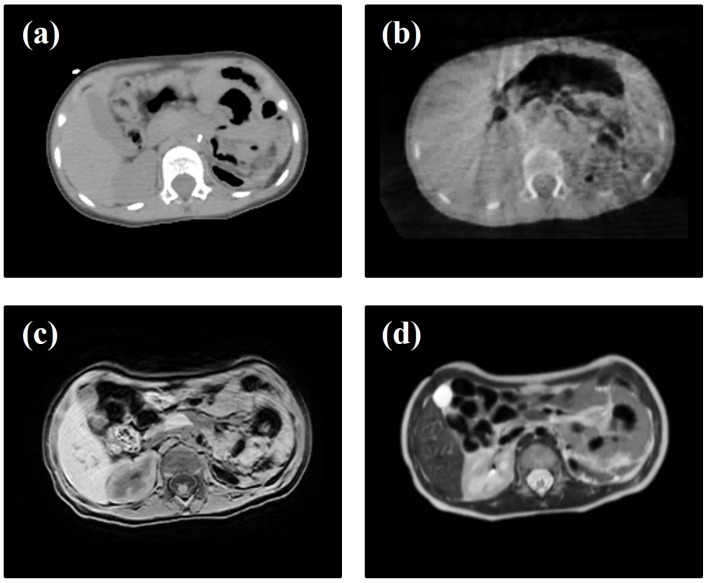

Figure 3.4 Example of transversal slices of the (a) planning-CT, (b) CBCT, (c) T1w- and (d) T2w-MR images used in the uncertainty analysis in this study.

CHAPTER 4

Evaluating the benefit of PBS vs. VMAT dose distributions in terms of dosimetric sparing and robustness against inter-fraction anatomical changes for pediatric abdominal tumors

The following chapter is based on:

Guerreiro F, Zachiu C, Seravalli E, Ribeiro CO, Janssens GO, Ries M, Denis de Senneville B, Maduro JH, Brouwer CL, Korevaar EW, Knopf AC and Raaymakers BW 2019 Evaluating the benefit of PBS vs. VMAT dose distributions in terms of dosimetric sparing and robustness against inter-fraction anatomical changes for pediatric abdominal tumors. *Radiother. Oncol.* 138:158-65.

Abstract

Background and Purpose: To evaluate the dosimetric sparing and robustness against inter-fraction anatomical changes between photon and proton dose distributions for children with abdominal tumors.

Material and Methods: Volumetric modulated arc therapy (VMAT) and intensity-modulated pencil beam scanning (PBS) proton dose distributions were calculated for 20 abdominal pediatric cases (average: 3 ; range: 1 - 8 years). VMAT plans were based on a full-arc while PBS plans were based on 2 - 3 posterior-oblique radiation fields. Plans were robustly optimized on a patient-specific internal target volume (ITV) using a uniform 5 mm set-up uncertainty. Additionally, for the PBS plans a ± 3% proton range uncertainty was accounted for. Fractional dose re-calculations were performed using the planning computed tomography (CT) deformably registered to the daily cone-beam CT (CBCT) images. Fractional doses were accumulated rigidly. Planned and CBCT accumulated VMAT and PBS dose distributions were compared using dose-volume histogram (DVH) parameters.

Results: Significant better sparing of the organs at risk with a maximum reduction in the mean dose of 40% was achieved with PBS. Mean ITV DVH parameters differences between planned and CBCT accumulated dose distributions were smaller than 0.5% for both VMAT and PBS. However, the ITV coverage ($V_{95\%} > 99\%$) was not reached for one patient in the accumulated VMAT dose distribution.

Conclusions: For pediatric patients with abdominal tumors, improved dosimetric sparing was obtained with PBS compared to VMAT. In addition, PBS delivered by posterior-oblique radiation fields demonstrated to be robust against anatomical inter-fraction changes. Compared to PBS, daily anatomical changes proved to affect the target coverage of VMAT dose distributions to a higher extent.

4.1 Introduction

Wilms' tumor (WT) and neuroblastoma (NBL) belong to the most frequent abdominal tumors in pediatric patients (Maris et al., 2007; Brok et al., 2016). Due to the use of a multimodality treatment comprising surgery, chemotherapy and radiotherapy, the survival rates for these patients have increased over the past few decades (Pritchard-Jones et al., 2015; Ladenstein et al., 2017). The sub-group of patients that receive radiotherapy is however at increased risk of developing toxicity to the normal tissue (NT).

With the use of more advanced photon radiotherapy techniques, such as volumetric modulated arc therapy (VMAT), conformal dose gradients are delivered to complex target volumes enabling the reduction of the NT volume irradiated at tumor dose levels (Otto, 2008). Nevertheless, low doses are still widely spread in the surrounding NT. With intensity-modulated proton therapy (IMPT) using a pencil beam scanning (PBS) delivery, as a result of the unique dose deposition pattern characterized by the low entrance dose and rapid dose fall-off (Lomax, 1999; Lomax et al., 2004), there is hope to reduce the low dose bath and consequently the radiation-induced late effects (Hill-Kayser et al., 2019). In literature, clinical studies on PBS are sparse, patient cohorts are small and the follow-up is too short to evaluate long-term complications. However, publications assessing the dosimetric feasibility of treating pediatric abdominal tumors with PBS report a better NT sparing with this type of irradiation (Hillbrand et al., 2008; Hattangadi et al., 2011; Kristensen et al., 2015; Vogel et al., 2017).

During radiotherapy treatments in abdominal cancer, inter-fraction anatomical changes, such as patient diameter variations, due to weight loss / gain, and daily gastrointestinal gas volume differences, might occur. Due to the unpredictability of these changes over the treatment course and the difference between the depth-dose curves of photons and protons, the effect of inter-fraction uncertainties on the target and NT doses can be different between the two delivery techniques. In theory, proton dose distributions are more sensitive to uncertainties in computed tomography (CT) densities and changes in patient anatomy compared to photon dose distributions (Albertini et al., 2011). Robust treatment planning is currently used in proton radiotherapy to prevent that the target coverage is not maintained throughout the treatment by mitigating the effect of both range and set-up uncertainties (Unkelbach et al., 2007; Fredriksson et al., 2011; Stuschke et al., 2012, 2013).

To facilitate the choice between photons and protons to treat pediatric patients, a dosimetric comparison and an evaluation of the robustness of both delivery techniques should be performed. However, studies comparing the robustness of photon and proton delivery modalities against inter-fraction anatomical changes for children have not been published yet. The goal of this study was to quantify for pediatric abdominal tumors: (1) the dosimetric differences in terms of dose sparing and (2) the dosimetric impact of daily anatomical changes based on cone-beam CT (CBCT) information between VMAT, used clinically at our department, and intensity-modulated PBS proton dose distributions.

4.2 Materials and Methods

4.2.1 Patient and imaging characteristics

After institutional review board approval (WAG/mb/17/008865), images from 20 consecutive patients treated at our department between April 2015 and September 2017 were included in this study: nine WT patients (average: 3 ; range: 1 - 8 years), undergoing flank irradiation after nephrectomy, and 11 NBL patients (average: 4 ; range: 1 - 7 years) (*Supplementary Material, section 4.6*).

For treatment preparation, patients were fixated in a vacuum mattress (Bluebag, Elekta, Stockholm, Sweden) in a supine position with the arms wide along the body. A four-dimensional CT (4D-CT) was acquired for each patient in treatment position and using the same field of view (FOV): from the lungs until the lower abdomen. The 4D-CT images were obtained as a series of ten phases using a 16-, 40-, or 64- channel detector scanner (Brilliance, Philips Medical Systems, Best, The Netherlands). Scans with a current of 120 mA, with 90 kV, a pitch of 0.8, a gantry rotation speed of 0.7 s, a slice thickness of 3 mm corresponding to a CT dose index (CTDI) of 6 mGy were acquired. The planning-CT was obtained by taking the pixel-by-pixel average of the ten phases of the 4D-CT. During treatment, daily CBCT images were acquired for all treatment fractions using the XVI 4.5.1 on-board CBCT imaging system (Elekta, Stockholm, Sweden). Scans with an arc of 200° of 10 ms and 16 mA with 100 kV and an acquisition timeframe of 30 s, leading to four times less imaging dose than a standard adult pre-set (CTDI of 1 mGy), were taken. During treatment, each CBCT was registered to the planning-CT using the rigid registration algorithm available online on the XVI software (Elekta, Stockholm, Sweden) (Borgefors, 1988).

4.2.2 Treatment planning characteristics

The clinical target volume (CTV) was created by expanding the gross tumor volume (GTV) by 5 mm for the NBL patients and 10 mm for the WT patients. To account for the breathing motion, an internal target volume (ITV) was individualized for each patient and orthogonal direction. Breathing motion was assessed by measuring center of mass displacements of surgical clips, used as surrogates for the tumor bed boundaries, visible on the maximum expiration and inspiration phases of the 4D-CT image. ITV expansions were up to 1 mm in the left-right (LR) and anterior-posterior (AP) directions and up to 2 mm in the craniocaudal (CC) direction, depending on the patient (**chapter 2**). All organs at risk (OARs) were contoured using the planning-CT. In addition, patient-specific safety margins were added to the OARs contours according to the individual motion measured on the 4D-CT image. OARs margins were up to 1 mm in the LR and AP directions and up to 3 mm in the CC direction, depending on the organ and on the patient (**chapter 2**).

Three-dimensional (3D) treatment plan optimization was performed in RayStation software (Raysearch, Stockholm, Sweden) using the planning-CT and using a collapsed cone engine for VMAT and a pencil beam algorithm for intensity-modulated PBS proton dose distributions. According to the department clinical protocol, VMAT plans consisted of a full-arc. Given the posterior location of the tumor, 2 - 3 posterior radiation fields were selected for the PBS plans. Number and direction of the proton beams (range [90° ; 240°]) were chosen individually per patient according to the tumor location and achievement of planning goals. To cover shallow targets, a range shifter of 40 mm was used. Additionally, a relative biological effectiveness (RBE) of 1.1 was included (Paganetti, 2014). For PBS dose calculations, the Monte Carlo (MC) dose engine is known to be more accurate than the pencil beam algorithm (Taylor et al., 2017). Nevertheless, due to the posterior location of the target and the chosen beam configuration, an average uncertainty of 0.5% on the dose-volume histogram (DVH) parameters was found between the MC and pencil beam optimized PBS dose distributions. Given this negligible difference and the longer optimization time required by the MC engine, PBS plans were computed using the pencil beam algorithm.

The center of the ITV was defined as the isocenter for both modalities. The prescribed dose (PD) ranged from 14.4 to 36.0 Gy (from 8 - 20 fractions), depending on the patient (*Supplementary Material, section 4.6*). To reduce the risk of asymmetric skeletal growth, a homogeneous dose was aimed for the vertebra volume adjacent to the ITV for both modalities: $V_{70-80\%}$ > 95-98%, depending on the patient (Hoeben et al., 2019).

To assure a fair dosimetric comparison, both VMAT and PBS dose distributions were 3D ITV-based robustly optimized and evaluated accounting for several scenarios where patient set-up and range (only for PBS) uncertainties were simulated. Set-up uncertainties were modeled by making translational shifts of the plan isocenter and range uncertainties by scaling the planning-CT density. A uniform 5 mm patient set-up and ± 3% range uncertainties were accounted for (Moyers et al., 2010; Albertini et al., 2011). During 3D robust plan optimization, robustness against these uncertainties was attained using a minimax optimization method (Fredriksson et al., 2011). Plans were optimized accounting for different dose scenarios using the selected set-up (5 mm in six directions plus the nominal plan) and range (± 3% plus the nominal plan, only for PBS) uncertainties. In total, seven and 21 dose scenarios were calculated during the VMAT and PBS plan optimization, respectively.

For the 3D robust plan evaluation, different dose scenarios were computed using the same magnitude of the set-up (5 mm in 26 fixed directions) and range (± 3%, only for PBS) uncertainties. In total, 26 and 52 dose scenarios were calculated for the VMAT and PBS plans, respectively. The information from all scenarios per technique was combined in a voxel-wise minimum evaluation dose (Vw_{min}) by calculating the minimum dose per voxel in all scenarios. Plans were considered clinically robust if 98% of the ITV received at least 95% of the PD ($V_{95\%}$> 98%) in the Vw_{min} (Korevaar et al., 2016).

As a result of the proton finite range and stopping power sensitivity to electron density variations, the robustness of the planned PBS dose distributions may be compromised by small deviations occurring during treatment delivery, such as (1) patient anatomy changes due to breathing motion, (2) inter-play effects and (3) machine errors (Lomax, 2016). Therefore, to assure that for this patient group a 3D ITV-based robust optimization is sufficient to cover these disturbing effects (1 - 3), a 4D robustness evaluation method (4DREM) was used to evaluate the PBS dose distribution of the patient denoting the largest target breathing motion (2 mm in the CC direction) (Ribeiro et al., 2019). Disturbing effects were considered by calculating sub-plan doses, based on treatment-plan specific delivery-machine log files, on all ten phases of the 4D-CT image (Ribeiro et al., 2019). Phase-specific dose contributions were accumulated on the expiration phase using ANACONDA (Anatomically Constrained Deformation Algorithm) algorithm available in RayStation software. Additionally, for each sub-plan, set-up and range uncertainties were incorporated by calculating dose scenarios accounting for 5 mm isocenter shifts in 14 directions and planning-CT density perturbations of ± 3%. PBS plan robustness was evaluated by calculating a 4D accumulated Vw_{min} (4D Vwa_{min}) obtained from the computed phase-specific dose scenarios. Robustness was confirmed if 98% of the CTV received at least 95% of the PD ($V_{95\%} > 98\%$) in the 4D Vwa_{min}.

4.2.3 Fractional dose calculation and accumulation

Fractional dose re-calculations were performed using the daily CBCT images. Despite CBCT is commonly employed for patient position verification during treatment, the imaging quality is inferior compared to CT resulting in incorrect Hounsfield units (HUs) for dose calculations (Stock et al., 2009; Fotina et al., 2012; Veiga et al., 2014). For the estimation of the HUs from the CBCTs, the planning-CT was deformably registered to each CBCT using Evolution (de Senneville et al., 2016). This algorithm was previously validated for CT - CBCT registrations for kidney and lung cancer patients (Zachiu et al., 2017). The performance of the registration algorithm was evaluated by visual inspection of tissue landmarks (i.e surgical clips). On the deformed CTs (dCTs), the gas volumes from the planning-CT were filled with a water equivalent density (0 HU) and the gas volumes from the CBCTs were rigidly copied for dose calculation purposes. Fractional doses were re-calculated on the dCTs and accumulated rigidly on the planning-CT. A rigid dose accumulation was chosen due to the limited soft-tissue contrast seen on the CBCTs (*Figure 4.1*). As CBCT images were acquired with less imaging dose than a standard adult protocol (*section 4.2.1*), an accurate estimation of the daily deformations cannot be guaranteed for all structures. Thus, the clinical ITV and OARs, delineated on the planning-CT, were used for the evaluation of the planned and CBCT accumulated dose distributions.

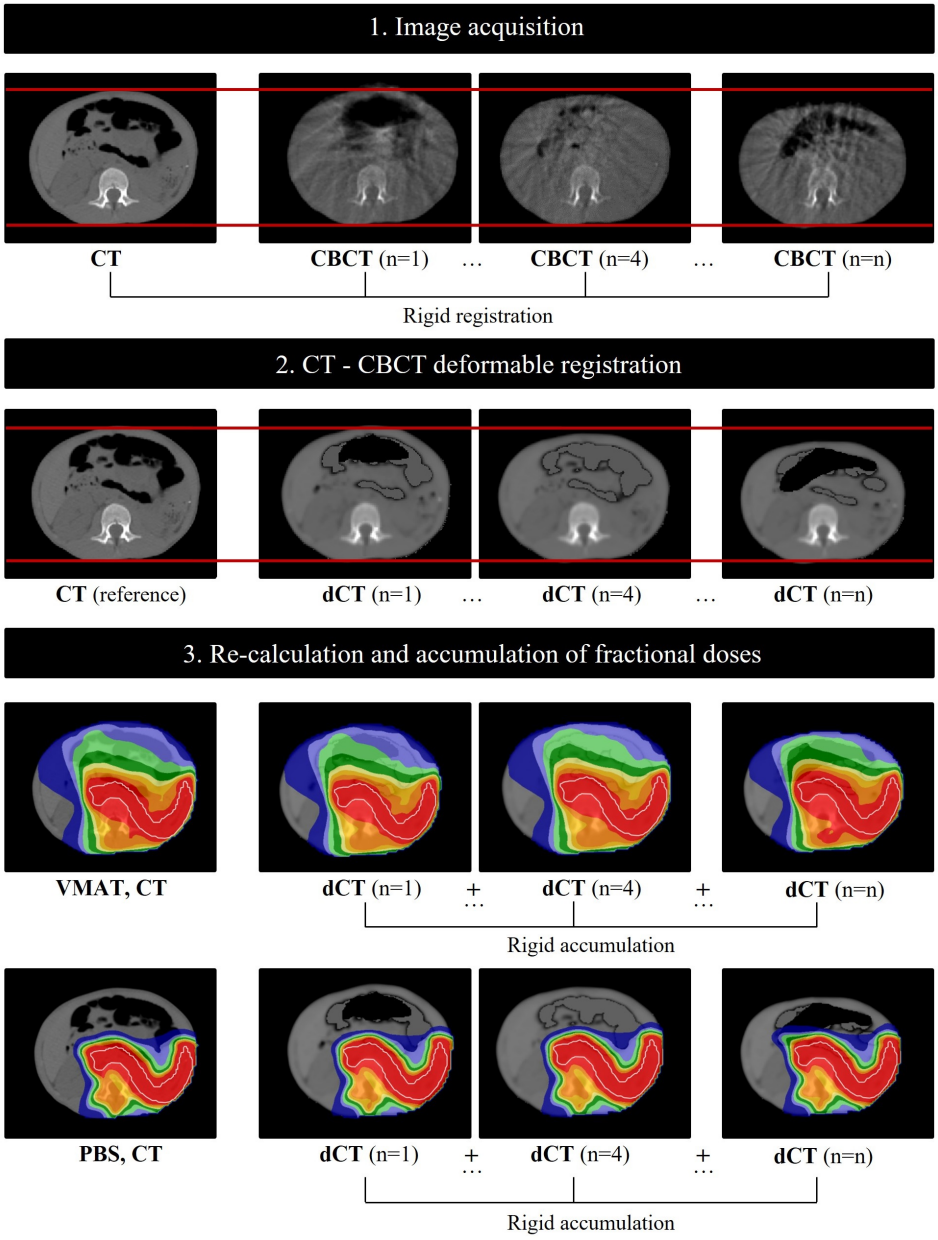

Figure 4.1 Schematic representation of the workflow used in this study. For the image acquisition (1), a planning-CT and daily CBCTs were acquired for each patient. CBCT images were obtained online for all treatment fractions and rigidly registered to the planning-CT. For the fractional dose re-calculations, the planning-CT was deformably registered to the CBCT images (2). Fractional doses were re-calculated on the dCTs and accumulated rigidly on the planning-CT for both VMAT and PBS dose distributions (3).

4.2.4 Evaluation

4.2.4.1 Anatomy

The changes in patient diameter and in gastrointestinal gas volume on the planning-CT and CBCTs were calculated for each patient. Gastrointestinal gas pockets were delineated within the available CBCT FOV. Variations in patient diameter were assessed by computing the difference of the distance in the AP direction of the ITV center of mass to the patient's surface between the planning-CT and the CBCT images.

4.2.4.2 Dosimetry

Two separate evaluations were performed: (1) comparison between VMAT and PBS planned dose distributions in terms of ITV robustness and dose sparing and (2) comparison between planned and CBCT accumulated VMAT and PBS dose distributions in terms of ITV robustness, OARs and NT doses.

For both (1) and (2), clinical DVH parameters were evaluated. For the ITV, the $D_{98\%}$, $D_{50\%}$ and $D_{2\%}$ were computed. In addition, the $V_{95\%}$ was calculated in the Vw_{min} and in the CBCT accumulated Vw_{min} (CBCT Vwa_{min}) to evaluate the robustness of (1) planned and (2) accumulated dose distributions, respectively. CBCT Vwa_{min} was obtained using a 1 mm set-up uncertainty (in 26 fixed directions), to simulate residual treatment errors, and a ± 3% range uncertainty (only for PBS). For the OARs, the mean dose (D_{mean}), $D_{50\%}$ and $D_{2\%}$ were computed. For the NT (defined as the body minus the ITV), the D_{mean}, V_{2Gy} and $V_{95\%}$ were calculated. Comparisons were statistically evaluated using the Wilcoxon test ($p<0.05$).

4.3 Results

4.3.1 Anatomy

In total, 224 CBCTs were evaluated. Patient diameter variations between the planning-CT and CBCTs were on average 0.5 ± 0.4 cm (range [-1.2 ; 2.0] cm). The volume of gastrointestinal gas as seen on the CBCT images showed large differences compared to the planning-CT: average 99.4 ± 126.9 ml (range [-216.7 ; 454.7] ml).

4.3.2 Dosimetry

ITV coverage was fulfilled in the planned VMAT and PBS dose distributions. Mean $V_{95\%}$ in the Vw_{min} was 98.7 ± 0.5 % (range [98.2 ; 99.8] %) and 98.8 ± 0.6 % (range [98.1 ; 99.6] %) for VMAT and PBS dose distributions, respectively. For the patient denoting the largest breathing motion, the $V_{95\%}$ of the CTV was 99.8% in the 4D Vwa_{min}.

Significant better sparing of the OARs and NT was achieved with PBS compared to VMAT for all patients (*Table 4.1, Figure 4.2*). The average reduction in the D_{mean} was 12.9 ± 8.0 % (range [3.4 ; 33.1] %) for the contralateral kidney, 8.1 ± 4.5 % (range [2.0 ; 15.7] %) for the ipsilateral kidney, 22.8 ± 7.4 % (range [5.5 ; 34.8] %) for the liver, 13.4 ± 7.7 % (range [1.6 ; 28.9] %) for the spleen, 17.4 ± 10.5 % (range [3.8 ; 39.5] %) for the pancreas and 8.0 ± 2.6 % (range [3.7 ; 13.9] %) for the NT.

Significant differences between the planned and CBCT accumulated dose distributions were only found for the ITV on the VMAT plans (*Table 4.2*). In the accumulated VMAT dose distributions, the ITV coverage was not met for one patient due to the large variation of gas volumes between the planning-CT and the CBCT images (*Figure 4.3*). Smaller dose differences on the ITV were found between planned and accumulated PBS dose distributions (*Table 4.2, Figure 4.3*). Mean $V_{95\%}$ in the CBCT Vwa_{min} was 99.6 ± 0.8 % (range [96.8 ; 100] %) and 99.8 ± 0.3 % (range [99.1 ; 100] %) for VMAT and PBS dose distributions, respectively. For the OARs, mean differences between planned and CBCT accumulated dose distributions were below 1.9% for VMAT and below 0.6% for PBS. Moreover, larger individual differences were found for VMAT (range [-11.3 ; 9.6] %) compared to PBS (range [-5.3 ; 5.2] %) dose distributions (*Table 4.2*).

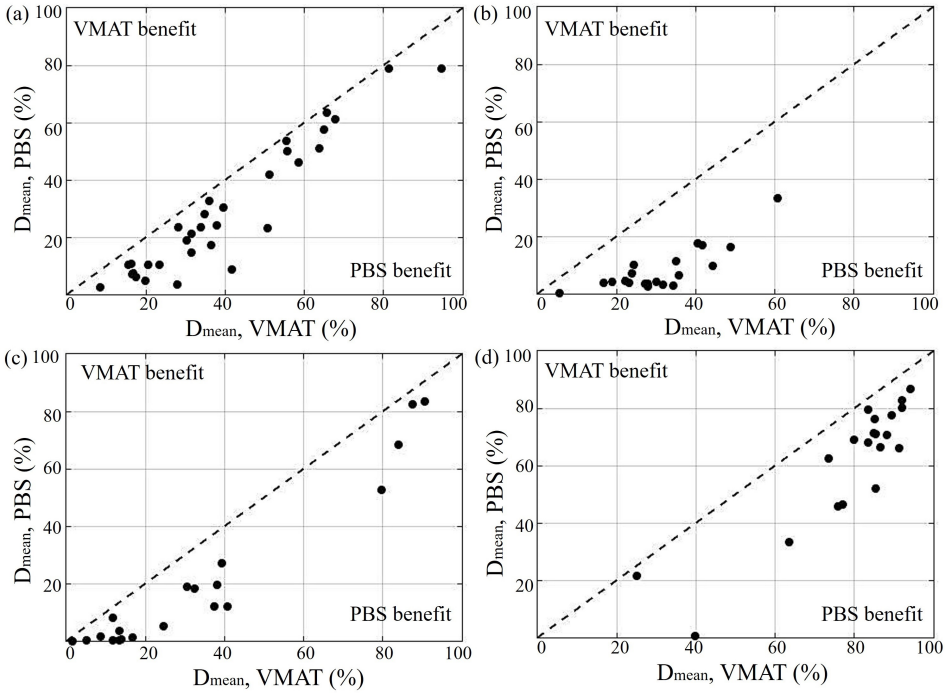

Figure 4.2 D_{mean} delivered by VMAT and PBS to the OARs for the kidneys (a), liver (b), spleen (c) and pancreas (d).

Table 4.1 DVH parameters (%) comparison of VMAT and PBS dose distributions, with p<0.05 (Wilcoxon test) considered significant (in bold). Δ*D* denotes the difference between VMAT and PBS dose distributions. Values are presented as a percentage of the respective PD. *Abbreviations: SD= standard deviation.*

Structures	(%)	VMAT	PBS	Δ*D* (VMAT - PBS)		
		mean ± SD	mean ± SD	mean ± SD	range	(p<0.05)
ITV	$D_{98\%}$	98.1 ± 0.5	98.1 ± 0.5	0.0 ± 0.8	[-1.2 ; 1.5]	1.0
	$D_{50\%}$	100.2 ± 0.1	100.4 ± 0.2	-0.2 ± 0.2	[-0.6 ; 0.4]	**1.6E-4**
	$D_{2\%}$	102.9 ± 1.0	104.0 ± 0.9	-1.2 ± 1.1	[-3.5; 0.9]	**1.0E-3**
Kidney (contralateral)	$D_{50\%}$	23.8 ± 10.5	9.8 ± 10.5	14.1 ± 9.1	[0.9 ; 37.6]	**2.6E-4**
	$D_{2\%}$	70.8 ± 22.6	62.2 ± 26.0	8.6 ± 9.4	[-3.3 ; 35.5]	0.3
Kidney (ipsilateral)	$D_{50\%}$	57.7 ± 26.2	48.5 ± 29.5	9.2 ± 5.2	[0.2 ; 17.6]	0.4
	$D_{2\%}$	95.2 ± 17.3	94.2 ± 19.0	0.9 ± 2.1	[-1.5 ; 5.4]	0.8
Liver	$D_{50\%}$	26.4 ± 13.1	0.3 ± 0.9	26.1 ± 12.7	[1.0 ; 49.7]	**7.6E-8**
	$D_{2\%}$	81.6 ± 16.9	67.3 ± 28.5	14.4 ± 13.6	[-0.7 ; 38.8]	0.2
Spleen	$D_{50\%}$	32.3 ± 32.8	17.7 ± 34.1	14.6 ± 10.5	[-1.3 ; 35.4]	**1.1E-3**
	$D_{2\%}$	65.2 ± 37.0	58.1 ± 43.8	7.2 ± 9.5	[-3.0 ; 25.1]	0.7
Pancreas	$D_{50\%}$	83.4 ± 22.8	66.8 ± 31.6	16.6 ± 17.1	[-0.8 ; 55.6]	**4.4E-2**
	$D_{2\%}$	98.7 ± 10.0	96.7 ± 21.6	1.9 ± 11.7	[-4.0 ; 51.1]	0.2
NT	V_{2Gy}	34.0 ± 8.8	14.2 ± 5.0	19.8 ± 5.2	[12.7 ; 30.2]	**1.4E-7**
	$V_{95\%}$	4.2 ± 2.1	3.8 ± 1.8	0.4 ± 0.6	[-0.7 ; 1.7]	0.6

Table 4.2 Dose differences (Δ*D*) between planned and CBCT accumulated dose distributions for VMAT and PBS, with p<0.05 (Wilcoxon test) considered significant (in bold). Values are presented as a percentage of the respective PD. If Δ*D*>0 the planned dose is higher than the accumulated dose and Δ*D*<0 otherwise. *Abbreviations: SD= standard deviation.*

Structures	(%)	Δ*D* (VMAT) (planned - accumulated)			Δ*D* (PBS) (planned - accumulated)		
		mean ± SD	range	(p<0.05)	mean ± SD	range	(p<0.05)
ITV	$D_{98\%}$	0.5 ± 0.9	[-1.9 ; 2.6]	**3.4E-2**	0.2 ± 0.5	[-0.3 ; 0.7]	0.7
	$D_{50\%}$	0.1 ± 0.8	[-2.4 ; 1.3]	0.2	0.1 ± 0.1	[-0.1 ; 0.3]	0.2
	$D_{2\%}$	-0.2 ± 0.9	[-2.8 ; 1.3]	0.6	-0.1 ± 0.6	[-1.7 ; 0.5]	1.0
Kidney (contralateral)	$D_{50\%}$	-0.2 ± 1.3	[-3.7 ; 2.6]	1.0	-0.2 ± 0.4	[-1.2 ; 0.4]	0.9
	$D_{2\%}$	-0.8 ± 3.5	[-9.4 ; 5.5]	0.9	0.0 ± 1.3	[-2.4 ; 4.2]	1.0
Kidney (ipsilateral)	$D_{50\%}$	1.9 ± 3.6	[-1.7; 9.6]	0.9	-0.1 ± 0.8	[-1.7 ; 1.2]	1.0
	$D_{2\%}$	0.0 ± 1.1	[-2.7 ; 1.9]	1.0	0.2 ± 0.6	[-0.2 ; 1.9]	0.8
Liver	$D_{50\%}$	0.4 ± 0.8	[-0.1 ; 2.6]	0.8	-0.2 ± 0.7	[-3.2 ; 0.1]	0.7
	$D_{2\%}$	0.6 ± 1.6	[-2.5 ; 4.8]	0.9	0.5 ± 2.5	[-4.8 ; 5.2]	1.0
Spleen	$D_{50\%}$	0.1 ± 0.8	[-1.7 ; 2.1]	1.0	0.2 ± 0.8	[-0.5 ; 3.4]	0.9
	$D_{2\%}$	-0.6 ± 3.0	[-11.3 ; 3.3]	0.8	0.0 ± 1.0	[-3.4 ; 1.6]	0.9
Pancreas	$D_{50\%}$	0.6 ± 1.5	[-1.9 ; 3.5]	0.9	0.6 ± 2.6	[-5.3 ; 4.7]	1.0
	$D_{2\%}$	0.1 ± 1.2	[-2.4 ; 2.3]	0.9	0.1 ± 1.0	[-2.2 ; 2.2]	0.6
NT	V_{2Gy}	0.7 ± 0.8	[-0.1 ; 3.0]	0.7	-0.1 ± 0.4	[-0.9 ; 0.9]	0.9
	$V_{95\%}$	0.1 ± 0.3	[-0.6 ; 0.8]	1.0	0.1 ± 0.1	[-0.1 ; 0.2]	0.8

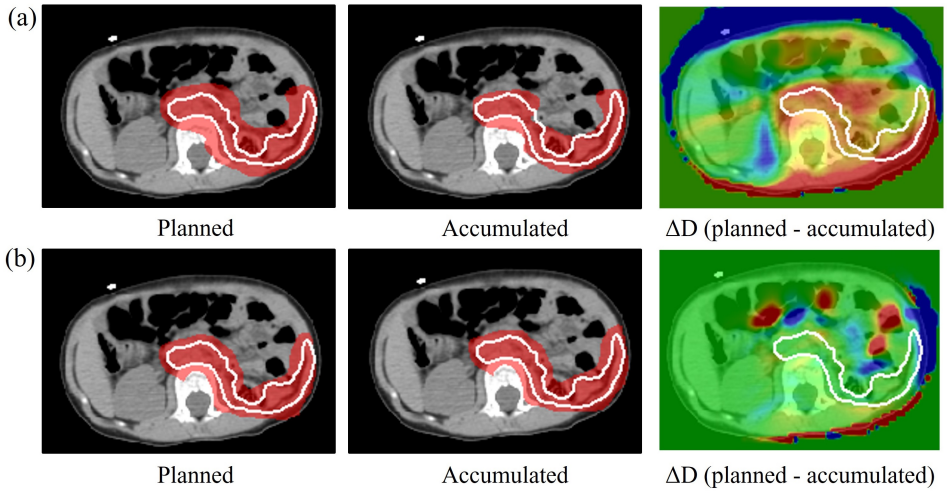

Figure 4.3 VMAT (a) and PBS (b) planned and CBCT accumulated dose distributions for the patient failing the ITV coverage in the accumulated VMAT dose distribution. Dose distributions are overlaid on the planning-CT. The 95% isodose is shown in red and the ITV in white. ΔD denotes the dose difference between planned and CBCT accumulated dose distributions in a -0.5 (blue, planned < accumulated dose) to 0.5 (red, planned > accumulated dose) Gy range.

4.4 Discussion

In the present study, dosimetric differences between 3D ITV-based robustly optimized VMAT and intensity-modulated PBS proton dose distributions were quantified in 20 pediatric patients with abdominal cancer. Moreover, the robustness of VMAT and PBS dose distributions against inter-fraction anatomical changes ($\leq$ 2 cm, $\leq$ 455 ml), visualized on daily CBCT images, was investigated for the same patient group. Results demonstrated a significant dosimetric sparing of the OARs and NT without compromising the target dose with PBS for all patients. Furthermore, PBS delivered by posterior-oblique radiation fields proved to be more robust against daily anatomical inter-fraction changes compared to VMAT using a full-arc delivery.

In literature, the dosimetric sparing with PBS was already investigated for both WT and NBL patients against conventional radiotherapy using two opposing radiation fields (Hillbrand et al., 2008; Vogel et al., 2017), 3D conformal radiotherapy (Kristensen et al., 2015) and intensity-modulated radiation therapy (IMRT) (Hillbrand et al., 2008; Hattangadi et al., 2011). Nevertheless, none of these studies compared PBS against VMAT. In addition, none of them used robust optimization and evaluation to account for the effect of both set-up and range uncertainties on the PBS dose distributions limiting the generality of the comparison between approaches. In proton therapy, uncertainties in CT densities and patient anatomy can generate severe effects on the delivered dose as proton path length changes result in displacements of the Bragg peak dose fall-off (Lo-

max, 2008a,b). Consequently, a PTV-based plan optimization is not accurate enough for proton therapy (Lomax, 2008a,b; Liu et al., 2013). In the present study, ITV-based robustly optimized VMAT plans were chosen for the comparison with PBS to mitigate biases related to the use of different optimization methods. Being aware that photon planning is commonly done using a PTV approach, differences between PTV-based and ITV-based robustly optimized VMAT dose distributions were calculated (*Supplementary Material, section 4.6*). No significant deviations were found for the majority of the DVH parameters.

In addition, a realistic choice of set-up and range (only for PBS) uncertainties was aimed during the robust optimization and evaluation (Moyers et al., 2010; Albertini et al., 2011). However, it can still be argued if the chosen uncertainties are too large given the available online image guidance and verification techniques. In previous studies (**chapter 2, 3**), we estimated the target safety margin to use in a CBCT-guided workflow for a group of 15 WT patients. When accounting for the treatment chain geometric accuracy, patient set-up and inter-fraction motion uncertainties, a target safety margin of 5 mm in all orthogonal directions was calculated (**chapter 3**). For this reason, a 5 mm set-up uncertainty plus an ITV margin to account for the breathing motion were used in this study. Nevertheless, range uncertainties might be further mitigated by the use of dual-energy CT (Yang et al., 2010) and / or proton CT (Hansen et al., 2018).

In literature, 4D robustly optimized and evaluated PBS dose distributions are reported to be more robust and interplay-effect-resistant for moving targets than 3D robustly optimized dose distributions (Liu et al., 2016). Since the use of 4D robust optimization and evaluation implies more manual work and optimization time, in the present work a 3D robust optimization and evaluation of the PBS dose distributions was performed. In addition, a 4D evaluation of the 3D robustly optimized PBS dose distribution for the patient denoting the largest breathing motion was done. For this patient, the target criterion ($V_{95\%}$>98% in the Vw_{min}) was met for both 3D and 4D evaluation methods (98.9% vs. 99.8%). Due to the target posterior location, the beam configuration chosen and the small magnitude of the breathing motion seen for this patient group (**chapter 2**), using 3D robustly optimized and evaluated PBS dose distributions is considered clinically suitable. Moreover, plan robustness evaluation was performed using a Vw_{min} and not a worst-case dose as previously reported in literature (Stuschke et al., 2012; Liu et al., 2013). Vw_{min} was chosen as a better agreement between the PTV criteria for photon plans and the target DVH criteria for PBS was denoted in comparison to the worst-case evaluation dose (Korevaar et al., 2016).

In this study, VMAT and PBS dose distributions robustness against inter-fraction anatomical changes was assessed using daily CBCT images. Due to the existence of possible image artifacts and inaccurate HUs, CBCT images are of limited value for direct dose calculations. Several methods to enable CBCT dose calculations have already been published in literature (Veiga et al. 2014, 2015; Kurz et al., 2015, 2016). In the present work, the planning-CT was deformably registered to the CBCTs to calculate the fractional doses. Two potential limitations of this apporach are (1) the rigid accumulation of fractional

doses and (2) the manual adaptation of daily gastrointestinal gas volume variations. For a deformable dose accumulation, a voxel-by-voxel accuracy is required (Veiga et al., 2015) which cannot be ensured due to the poor CBCT image quality seen (*Figure 4.1*). While using a rigid dose accumulation, daily anatomical deformations were neglected. Nevertheless, the largest inter-fraction anatomical changes, such as patient diameter and gastrointestinal gas volume variations, were accounted for. Moreover, the manual adaptation of the gas volumes was sufficient for the purpose of this study but can represent a limitation for daily online re-planning. Due to the unpredictability of gastrointestinal gas volume changes, for the calculation of the fractional doses in abdominal cancer patients using a CBCT scatter correction approach as suggested by (Kurz et al., 2016) or fast deep learning methods (Kida et al., 2018; Kurz et al., 2018) might be considered better options for an online re-planning workflow. Nevertheless, these methods either require (1) storing of vendor specific CBCT projections (Kurz et al., 2016), which is a disadvantage when needing to use other on-board imaging systems, or (2) large amounts of imaging data for the network training (Kida et al., 2018; Kurz et al., 2018), which is a limitation for children due to the large variability in age, height and weight in pediatric cohorts.

The results of this study show that the ITV coverage was reduced in the CBCT accumulated VMAT dose distribution compared to the planned dose for one patient. Smaller ITV and OARs dose differences were seen for PBS as a result of the selected beam configuration / angles. With the use of patient-specific posterior-oblique radiation fields, uncertainties related to the variation of gastrointestinal gas volumes during treatment can be avoided as the proton beams stop before reaching the anterior part of the abdomen. Clinically, the VMAT plans are optimized using a full-arc as a requirement to achieve both an acceptable target coverage and a homogeneous dose in the vertebra (Hoeben et al., 2019). Thus, planning strategies such as performing a density override of the gastrointestinal gas pockets on the planning-CT or using online daily re-planning might be necessary to reduce discrepancies between planned and delivered photon doses. In future studies investigating the robustness of both photon and proton radiotherapy plans, imaging data with more appropriate image quality (i.e MRI) should be used to better quantify the target and OARs fractional doses. Furthermore, the plan robustness evaluation should be included in trials to select patients that benefit from proton therapy.

From a dosimetric point of view to treat children with WT or NBL, PBS showed to be more favorable, regarding both dose sparing and robustness against inter-fraction anatomical changes, compared to VMAT. Nevertheless, long-term follow-up of a large pediatric cohort is mandatory to estimate the real clinical benefit of treating children with PBS. In addition, a comprehensive dosimetric assessment of the available radiotherapy modalities is essential to take advantage of more recent techniques. In comparison with PBS, MRI-guided treatments are also showing to be promising for pediatric patients. With MRI-guided systems (Raaymakers et al., 2017), the use of decreased safety margins due to the better visualization of the target could be achieved allowing for real-time adaptive regimes without extra patient radiation burden (Lagendijk et al., 2014). In a previous study (**chapter 3**), we have quantified the dosimetric impact when

using MRI-guided IMRT ($IMRT_{MRI}$) compared to the clinical VMAT workflow to treat WT patients (n=15). When using a PTV margin of 1 mm for the $IMRT_{MRI}$ (simulating a best-case scenario), the calculated D_{mean} was 18% in the kidney, 30% in the liver, 32% in the spleen and 68% in the pancreas. In the present study, for the same patient category (WT, n=9) when using robustly optimized PBS dose distributions (5 mm, ± 3%), the computed D_{mean} was 15% in the kidney, 10% in the liver, 32% in the spleen and 53% in the pancreas. Consequently for this patient category, intensity-modulated PBS using current clinical robustness settings is shown to be more dosimetrically favorable compared to the best-case scenario of $IMRT_{MRI}$. In the future, further dosimetric sparing might be expected if using MRI-guided PBS (PBS_{MRI}). This approach is not clinically available yet, however research has been going on to prove the feasibility of MRI-guided proton systems and the corresponding treatment workflow (Oborn et al., 2017). Future work will include evaluating the potential dosimetric benefit with PBS_{MRI} for pediatric patients with abdominal tumors.

4.5 Conclusion

In summary, this study provides substantial dosimetric information to help assessing the optimal referral patterns for pediatric patients with abdominal tumors. From a dosimetric point of view to treat children with WT or NBL, intensity-modulated PBS showed to be more favorable, regarding both dose sparing and robustness against inter-fraction anatomical changes, compared to VMAT. Whether the reported dosimetric gain and robustness against inter-fraction anatomical changes of PBS dose distributions is translated into any clinical benefit for this patient category is however uncertain at present time.

4.6 Supplementary Material

Table 4.3 Patient, tumor and treatment characteristics. Tumor characteristics according to International Society of Paediatric Oncology (SIOP) for WT patients and to European SIOP neuroblastoma group (SIOPEN) for NBL patients. *Abbreviations: HR= high risk group; IR= intermediate risk group; SM+= positive section margins; LN+= lymph nodes involvement; NEF= nephrectomy; Fra= fractions.*

	Patient Characteristics			Tumor Characteristics	Treatment Characteristics		
	No	Sex	Age (years)	Classification (risk group); stage (SM+/LN+)	NEF side	Dose (Gy)	No Fra
WT	1	F	8	blastemal type (HR); stage III (SM+)	Left	25.2	14
	2	F	4	regressive type (IR); stage III (LN+)	Left	14.4	8
	3	F	4	regressive type (IR); stage III (SM+)	Left	14.4	8
	4	M	3	regressive type (IR); stage III (SM+, LN+)	Left	14.4	8
	5	F	3	regressive type (IR); stage III (SM+, LN+)	Right	14.4	8
	6	F	2	regressive type (IR); stage III (SM+)	Right	14.4	8
	7	M	2	mixed type (IR); stage III (SM+)	Left	14.4	8
	8	M	1	regressive type (IR); stage III (SM+)	Right	14.4	8
	9	M	1	stromal type (IR); stage III (SM+, LN+)	Right	14.4	8
NBL	10	M	6	Macroscopic residual disease		36	20
	11	F	5	Macroscopic residual disease		36	20
	12	F	2	Macroscopic residual disease		30	10
	13	F	7	Microscopic residual disease		21.6	12
	14	M	5	Microscopic residual disease		21.6	12
	15	M	5	Microscopic residual disease		21.6	12
	16	F	4	Microscopic residual disease		21.6	12
	17	M	2	Microscopic residual disease		21.6	12
	18	F	2	Microscopic residual disease		21.6	12
	19	F	1	Microscopic residual disease		21.6	12
	20	F	1	Microscopic residual disease		21.6	12

Table 4.4 DVH parameters (%) comparison of ITV-based robustly optimized VMAT ($VMAT_{ITV}$), using a set-up uncertainty of 5 mm, and PTV-based optimized VMAT ($VMAT_{PTV}$), using a PTV margin of 5 mm, dose distributions with p<0.05 (Wilcoxon test) considered significant (in bold). ΔD denotes the difference between $VMAT_{ITV}$ and $VMAT_{PTV}$ dose distributions. Values are presented as a percentage of the respective PD. *Abbreviations: SD= standard deviation.*

Structures	(%)	$VMAT_{ITV}$	$VMAT_{PTV}$	ΔD ($VMAT_{ITV}$ - $VMAT_{PTV}$)	
		mean ± SD	mean ± SD	mean ± SD	(p<0.05)
ITV	$D_{98\%}$	98.1 ± 0.5	97.3 ± 0.8	0.8 ± 0.9	**1.0E-03**
	$D_{50\%}$	100.2 ± 0.1	100.7 ± 0.3	-0.5 ± 0.3	**8.8E-7**
	$D_{2\%}$	102.9 ± 1.0	103.6 ± 1.0	-0.7 ± 0.8	**1.9E-02**
Kidney (contralateral)	$D_{50\%}$	23.8 ± 10.5	25.4 ± 11.0	-1.6 ± 5.3	0.6
	$D_{2\%}$	70.8 ± 22.6	70.6 ± 23.14	0.2 ± 4.6	1.0
Kidney (ipsilateral)	$D_{50\%}$	57.7 ± 26.2	55.6 ± 26.6	2.1 ± 3.8	0.7
	$D_{2\%}$	95.2 ± 17.3	95.2 ± 18.4	0.0 ± 1.5	0.5
Liver	$D_{50\%}$	26.4 ± 13.1	27.3 ± 13.2	-1.0 ± 3.9	0.7
	$D_{2\%}$	81.6 ± 16.9	82.4 ± 16.7	-0.8 ± 2.8	0.8
Spleen	$D_{50\%}$	32.3 ± 32.8	32.0 ± 32.9	0.2 ± 3.9	1.0
	$D_{2\%}$	65.2 ± 37.0	66.4 ± 35.7	-1.2 ± 3.4	1.0
Pancreas	$D_{50\%}$	83.4 ± 22.8	81.9 ± 22.5	1.5 ± 3.5	0.7
	$D_{2\%}$	98.7 ± 10.0	99.6 ± 8.6	-1.0 ± 1.7	0.1
NT	V_{2Gy}	34.0 ± 8.8	33.3 ± 9.0	0.7 ± 2.2	0.8
	$V_{95\%}$	4.2 ± 2.1	4.3 ± 2.2	-0.1 ± 0.3	0.8

Table 4.5 Dose differences (ΔD) between planned and accumulated dose distributions for $VMAT_{ITV}$ and $VMAT_{PTV}$, with p<0.05 (Wilcoxon test) considered significant (in bold). Values are presented as a percentage of the respective PD. If ΔD>0 the planned dose is higher than the accumulated dose and ΔD<0 otherwise. *Abbreviations: SD= standard deviation.*

Structures	(%)	ΔD ($VMAT_{ITV}$) (planned - accumulated)		ΔD ($VMAT_{PTV}$) (planned - accumulated)	
		mean ± SD	(p<0.05)	mean ± SD	(p<0.05)
ITV	$D_{98\%}$	0.5 ± 0.9	**3.4E-2**	0.3 ± 1.2	**4.1E-2**
	$D_{50\%}$	0.1 ± 0.8	0.2	0.1 ± 0.8	0.3
	$D_{2\%}$	-0.2 ± 0.9	0.6	-0.3 ± 1.1	0.6
Kidney (contralateral)	$D_{50\%}$	-0.2 ± 1.3	1.0	-0.3 ± 1.3	0.9
	$D_{2\%}$	-0.8 ± 3.5	0.9	-0.8 ± 3.2	0.8
Kidney (ipsilateral)	$D_{50\%}$	1.9 ± 3.6	0.9	1.6 ± 2.8	1.0
	$D_{2\%}$	0.0 ± 1.1	1.0	0.0 ± 1.0	0.8
Liver	$D_{50\%}$	0.4 ± 0.8	0.8	0.3 ± 0.6	0.9
	$D_{2\%}$	0.6 ± 1.6	0.9	0.3 ± 1.0	0.9
Spleen	$D_{50\%}$	0.1 ± 0.8	1.0	0.1 ± 0.7	1.0
	$D_{2\%}$	-0.6 ± 3.0	0.8	-0.5 ± 2.6	0.8
Pancreas	$D_{50\%}$	0.6 ± 1.5	0.9	0.5 ± 1.6	0.9
	$D_{2\%}$	0.1 ± 1.2	0.9	0.3 ± 1.6	0.9
NT	V_{2Gy}	0.7 ± 0.8	0.7	0.6 ± 0.9	0.7
	$V_{95\%}$	0.1 ± 0.3	1.0	0.1 ± 0.3	0.9

CHAPTER 5

Feasibility of MRI-only photon and proton dose calculations for pediatric patients with abdominal tumors

The following chapter is based on:

Guerreiro F, Koivula L, Seravalli E, Janssens GO, Maduro JH, Brouwer CL, Korevaar EW, Knopf AC, Korhonen J and Raaymakers BW 2019 Feasibility of MRI-only photon and proton dose calculations for pediatric patients with abdominal tumors. *Phys. Med. Biol.* 64(5):055010.

Abstract

Background and Purpose: The purpose of this study was to develop a method enabling synthetic computed tomography (sCT) generation of the whole abdomen using magnetic resonance (MR) images of pediatric patients with abdominal tumors.

Material and Methods: The proposed method relies on an automatic atlas-based segmentation of bone and lungs followed by an MRI intensity to synthetic Hounsfield unit conversion. Separate conversion algorithms were used for the bone, lungs and soft-tissue. Rigidly registered CT and T2-weighted MR images of 30 patients in treatment position and with the same field of view were used for the evaluation of the atlas and the conversion algorithms. The dose calculation accuracy of the generated sCTs was verified for volumetric modulated arc therapy (VMAT) and pencil beam scanning (PBS) proton therapy. VMAT and PBS plans were robustly optimized on an internal target volume (ITV) against a patient set-up uncertainty of 5 mm.

Results: Average differences between CT and sCT dose calculations for the ITV $V_{95\%}$ were 0.5% (range [0.0 ; 5.0] %) and 0.0% (range [-0.1 ; 0.1] %) for VMAT and PBS dose distributions, respectively. Average differences for the mean dose to the organs at risk were $\leq$ 0.2% (range [-0.6 ; 1.2] %) and $\leq$ 0.2% (range [-2.0 ; 2.6] %) for VMAT and PBS dose distributions, respectively.

Conclusions: Results showed that MRI-only photon and proton dose calculations were feasible for children with abdominal tumors.

5.1 Introduction

Wilms' tumor (WT) and neuroblastoma (NBL) belong to the most frequent abdominal tumors in pediatric patients. By combining the use of surgery, chemotherapy and radiotherapy, the survival rates for these patients have increased over the past few decades up to 90% for WT and 60% for NBL (Pritchard-Jones et al., 2015; Ladenstein et al., 2017).

During radiotherapy treatment planning (RTP) with either photons or protons, computed tomography (CT) imaging is used for the conversion of Hounsfield unit (HU) values to relative electron density (in photon therapy) or stopping power ratio relative to water (in proton therapy). This information is needed for the computation of the dose to deliver to the patient (Chernak et al., 1975). Magnetic resonance imaging (MRI) yields superior soft-tissue visualization allowing for a better visualization of the target and the assessment of the organs at risk (OARs) motion and deformation without patient radiation burden (Lagendijk et al., 2014). In the last few years, MRI-only RTP has been introduced into clinics (Edmund and Nyholm, 2017; Tenhunen et al., 2018) promising to avoid systematic uncertainties arising from the CT - MR image registration and to decrease the patient exposure to ionizing radiation by skipping the planning-CT. Reducing both the registration uncertainties and the patient imaging dose is particularly important for pediatric patients for whom the radiation oncology community strives to minimize the risk of radiation-induced complications.

Currently, the main challenge of performing MRI-only dose calculations is the estimation of tissue attenuation properties from the MR images. For this purpose, the commonly named pseudo CT or synthetic CT (sCT) images can be generated from the patient's MRI to serve as surrogate for the dose calculations. Two recent review articles by (Edmund and Nyholm, 2017) and (Johnstone et al., 2018) provide a comprehensive overview of the currently available sCT generation methods. These can be divided in four different approaches: bulk-density override, atlas-based, voxel-based and more recently introduced deep learning methods.

Bulk-density override has been studied for over a decade with either manual or automatic contour segmentation (Lee et al., 2003; Stanescu et al., 2008). Although this technique provides a user-friendly method for sCT generation, it does not allow a straightforward creation of reference images for patient positioning verification during RTP (Johnstone et al., 2018). For the atlas-based methods, the main goal is to create an MR to CT image atlas and convert the MRI intensity into HU values by registering the patient's MRI to the atlas (Dowling et al., 2012, 2015; Uh et al., 2014; Guerreiro et al., 2017). The main drawbacks of this method are the lack of adaptation to atypical anatomies and the strict requirements for imaging posture and settings. Voxel-based methods rely only on the MRI contrast, independently of the voxels location, for the generation of sCT images for different body parts and anatomies (Hsu et al., 2013; Edmund et al., 2014; Korhonen et al., 2014; Jonsson et al., 2015). Compared to the atlas-based approach, images generated by this method are usually more vulnerable to MRI artifacts (Sjolund et al., 2015). More recently, novel techniques for sCT generation are being explored by deep learn-

ing methods. (Han, 2017) and (Dinkla et al., 2018) have presented fast sCT generation methods using a convolutional neural network (CNN) and (Maspero et al., 2018) using a conditional generative adversarial network (cGAN).

Despite providing an acceptable dose calculation accuracy, none of these sCT generation approaches is reported to outperform the others (Edmund and Nyholm, 2017; Johnstone et al., 2018). Moreover, a population-based study comparing CT- and sCT-based dose calculations should be initiated in order to establish acceptable dosimetric deviations from the planning-CT dose for clinically relevant dose-volume histogram (DVH) parameters (Korsholm et al., 2014).

In the past few years using the mentioned techniques, sCT images have been generated for several body sites such as brain (Edmund et al., 2014; Jonsson et al., 2015; Koivula et al., 2016; Dinkla et al., 2018), head & neck (Hsu et al., 2013; Sjolund et al., 2015; Guerreiro et al., 2017) and pelvis (Korhonen et al., 2014; Koivula et al., 2016; Guerreiro et al., 2017; Maspero et al., 2017a,b, 2018) in adult patients. The purpose of this study was to develop a method enabling sCT generation for pediatric patients, which is one of the most challenging patient populations as a result of the highly individual anatomies among patients. To the authors' knowledge, the present work is the first generating sCTs with a large field of view (FOV), including the whole abdomen, for children diagnosed with abdominal cancer. The presented sCT generation method is based on an automatic atlas-based segmentation of tissue classes followed by a voxel-based MRI intensity to HU values conversion algorithm. The accuracy of performing dose calculations with the generated sCTs was assessed for both photon and proton irradiation modalities.

5.2 Materials and Methods

5.2.1 Patient and imaging characteristics

After institutional review board approval (WAG/mb/17/008865), images from 30 consecutive patients treated at the radiotherapy department of the University Medical Center Utrecht (UMCU) between April 2015 and January 2018 were included in this study: nine WT patients (mean age: 3, range: 2 - 4 years), undergoing flank irradiation, and 21 NBL patients (mean age: 4, range 2 - 7 years). For nine out of 30 patients, the target was located on the upper part of the abdomen within the diaphragm border (Pat_{up}s), while for the remaining 21 patients the target was located on the lower part of the abdomen (Pat_{low}s).

After chemotherapy and resection, all patients received radiotherapy to the primary tumor site. For treatment preparation, four-dimensional CT (4D-CT) and T2-weighted (T2w-) MR images were acquired for each patient on the same day ($\leq$ 45 min), in radiotherapy treatment position and using the same FOV which covered the top of the lungs until the lower abdomen. Patients were fixated in a supine position in an individualized vacuum mattress (Bluebag, Elekta, Stockholm, Sweden) and imaging was per-

formed with patients under general anesthesia. The 4D-CT images were acquired using a 16-, 40-, or 64- channel detector scanner (Brilliance, Philips Medical Systems, Best, The Netherlands). Respiratory trace measurements for pulmonary gating were obtained using a deformable rubber belt fixed to the patient's chest (Philips Bellow System, Philips Medical Systems, Best, The Netherlands). The planning-CT was obtained by taking the pixel-by-pixel mean of the ten phases of the 4D-CT. Voxel dimensions ranged between 0.8 - 1.4 mm for both left-right (LR) and anterior-posterior (AP) directions and between 2 - 3 mm for the craniocaudal (CC) direction, depending on the patient. The T2w-MR images were acquired using a 1.5 T Philips Achieva MRI scanner (Philips Medical Systems, Best, The Netherlands) and a three-dimensional (3D) turbo spin echo sequence without motion compensation strategies. Voxel dimensions ranged between 0.7 - 0.8 mm for both LR and CC directions and between 1 - 3 mm for the AP direction, depending on the patient. The specific sequence parameters for the T2w-MR images were as follows: TE= 90 ms, TR= 454.4 ms, flip angle= 90 deg, BW= 570 Hz and acquisition duration= 249 s.

5.2.2 sCT generation

The proposed sCT method is an extension of the previously published dual-model technique, described in detail in (Korhonen et al., 2014; Koivula et al., 2016, 2017), combining an automatic atlas-based segmentation and a voxel-based MRI intensity to HU values conversion algorithm for bone and soft-tissue classes. Briefly, in the current sCT method auto-segmentation and conversion algorithms for the lungs were included in addition to bone and soft-tissue classes. For each patient, a single T2w-MR image was used for the sCT generation. A schematic representation of the adopted workflow is shown in *Figure 5.1* and all steps are described in more detail on the following sections.

5.2.2.1 Automatic atlas-based segmentation

Rigidly registered, based on mutual information, planning-CT and T2w-MR images were used for the atlas construction. A selection of patients (24 / 30) was divided into three groups based on their height: group one (range [86 ; 95] cm), group two (range [96 ; 112] cm) and group three (range [113 ; 124] cm), each group containing eight patients. A separate atlas was created for each of the three groups by manually contouring bones and lungs volumes on the T2w-MR images. For the sCT generation, the automatic segmentation of bone and lungs volumes from MRI was made using a leave-one-out strategy for the 24 patients included in the atlas database. For the remaining six patients, bone and lungs were automatically segmented using one of the three generated atlases depending on the patient's height. The commercial medical image processing software MIM (version 6.7, MIM Software, Inc., Cleveland, OH, USA) was used for the automatic atlas-based segmentation by creating a deformable registration based on mutual information between the patient's MR and the MR images in the atlas. Manually contoured bone and lungs volumes from the patients in the atlas were combined and average volumes were obtained for each patient. Additionally, the soft-tissue was automatically segmented using a Boolean exclusion of the segmented bone and lungs volumes from the body contour

defined on the MRI. On the planning-CT, tissue classes were automatically segmented by applying a threshold: bone (HU > 150), lungs (HU < -150) and soft-tissue (-150 ≤ HU ≤ 150). No manual adjustments of the MRI and planning-CT contours were done after auto-segmentation.

5.2.2.2 Conversion algorithms for bone, lungs and soft-tissue

Before performing the MRI intensity to HU values conversion, the MR images were 3D bias-field corrected (Tustison et al., 2010) to enable a uniform intensity level across the patient body. In addition, the original MRI intensity values were scaled to a coherent base level, which corresponded to the median intensity level of the adipose tissue calculated from the MR images of the 24 patients included in the atlases (Koivula et al., 2017). This workflow was previously shown to be robust for the sCT generation using MR images from multiple MRI scanners and with different intensity levels.

The conversion from MRI intensity to HU values was done directly by using three different curves corresponding to each of the automatic segmented tissue classes (*section 5.2.2.1*): bone, lungs and soft-tissue. Conversion curves (*Figure 5.1*) were constructed using the segmented CT and MRI volumes of the 24 patients included in the atlases. Furthermore, the three calculated conversion curves were used for the MRI intensity to HU values conversion for all 30 patients.

For the bone and lungs conversion curves construction, the MRI intensity and corresponding CT HU values were matched using histogram points: histogram peak as the median value and the 5% cut-off value from the median as minimum and maximum values. For the bone, the HU values conversion was executed as inversely proportional to the MRI intensity values. As a result, the low signal from cortical bone on the MRI was linked to high HU values (HU = 807) while the high signal from bone marrow on the MRI was linked to lower HU values (HU = -47). For the lungs, the MRI intensity to HU values correspondence was defined to be directly proportional. Therefore, the low signal from alveonic-rich tissue on the MRI was represented by low HU values (HU = -783) while the high signal from lung capillaries on the MRI was represented by higher HU values (HU = -101). For both conversion curves, a step-wise function using 12 constant HU segments was used to estimate the values in between. For the soft-tissue conversion curve construction, MRI intensity values were collected using regions of interest inserted in the muscle, adipose tissue and fluids. Then, the MRI voxel values were converted into HU values in a three-part step-wise conversion relying on the known HU values of muscle (HU = 55), adipose tissue (HU = -105) and fluids (HU = 10). HU values between these three segments were interpolated using a step-wise function with three steps.

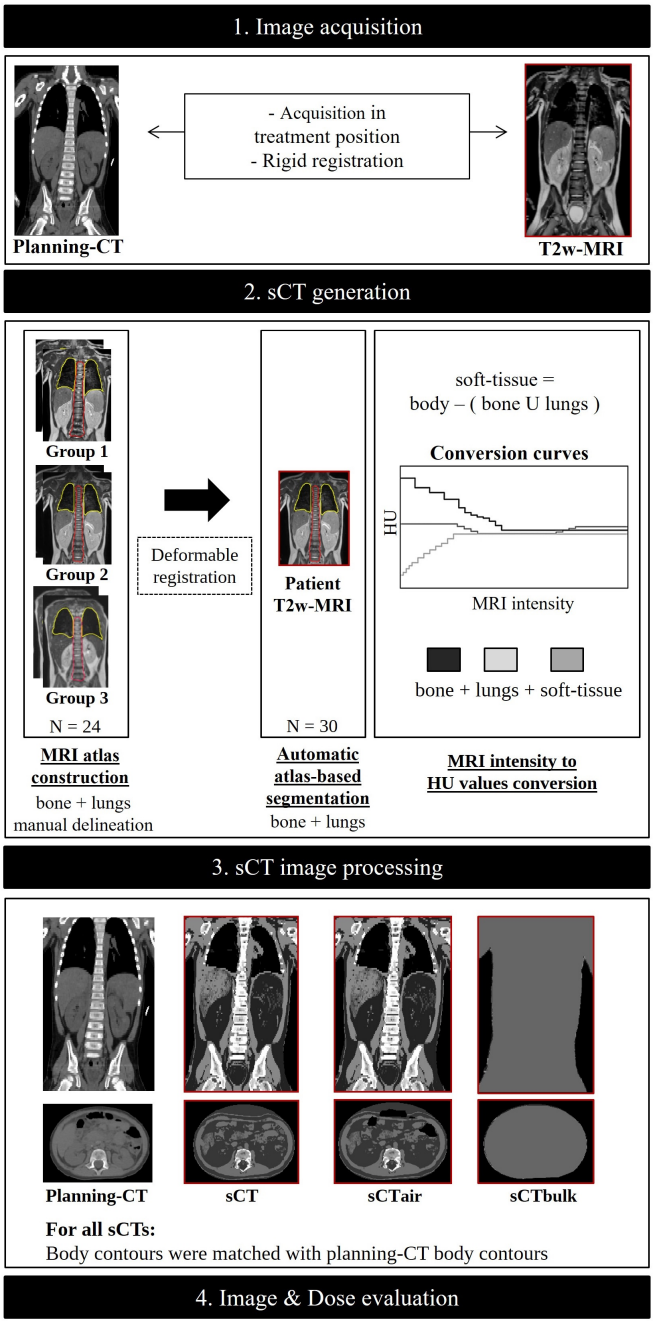

Figure 5.1 Schematic representation of the workflow used in this study. For the image acquisition (1), both planning-CT and T2w-MR images were acquired on the same day and in treatment position. The sCT generation method (2) is divided in two steps: The automatic atlas-based segmentation followed by the MRI intensity to HU values conversion for the bone, lungs and soft-tissue classes. For each patient (n=30), a single T2w-MR image was used for the sCT generation. The final two steps consisted of the sCT image processing (3) and the image and dose evaluation (4).

5.2.2.3 sCT image processing

For each patient, the sCT was re-sampled to the planning-CT dimensions. On the sCT, the body contour from the planning-CT was used instead of the body contour provided by the MRI. This was done to minimize uncertainties arising from set-up and time differences between the CT and MR imaging sessions. Thus, areas of the MRI outside the planning-CT body contour were manually labeled as -1000 HU and areas of the planning-CT outside the MRI body contour were manually labeled as 0 HU. Furthermore, on the original sCTs the bowel gases were assigned automatically as muscle HU while no density override was performed on the planning-CT. To minimize the possible differences between the planning-CT and the original sCT doses arising from the bowel filling, a second set of sCTs was generated containing the air pockets extracted from the planning-CT (sCT_{air}).

5.2.3 Treatment planning characteristics

For both patient groups, the gross tumor volume (GTV) consisted of the pre-operative tumor extension, including pathologic lymph nodes and residual disease if applicable. The clinical target volume (CTV) was created by expanding the GTV by 5 mm, for WT patients, and by 10 mm, for NBL patients. To account for the breathing motion, assessed by using a 4D-CT and surgical clips as surrogates, an internal target volume (ITV) was individualized in each orthogonal direction for all patients (**chapter 2**).

The sCT dosimetric accuracy was assessed for both volumetric modulated arc therapy (VMAT), used currently clinically at the radiotherapy department of UMCU to treat these patients, and intensity-modulated pencil beam scanning (PBS) proton therapy. For both VMAT and PBS plans, RTP was performed in RayStation treatment planning system (Raysearch, Stockholm, Sweden) using the planning-CT and a uniform dose grid of 3 mm. The VMAT plans consisted of a 6 MV full-arc. Since the target volumes were mainly located in the posterior part of the abdomen, the PBS plans were based on 2 - 3 posterior-oblique radiation fields to avoid the effect of bowel filling on the dose distributions. The center of the ITV was selected as the isocenter for both delivery techniques. The prescribed dose (PD) ranged from 14.4 to 36.0 Gy, depending on the patient. To reduce the risk of asymmetric skeletal growth, a homogeneous dose was aimed for the vertebra volume adjacent to the ITV. To achieve that, the following constraint was applied to the vertebra volume: $V_{70-80\%} >$ 95-98%, depending on the patient.

Both VMAT and PBS plans were 3D robustly optimized on the ITV using a minimax optimization method (Fredriksson et al., 2011) and a uniform 5 mm patient set-up uncertainty. For the PBS plans, robustness against a range uncertainty was not accounted for to assess the dose differences in a setting more susceptible to density changes between the planning-CT and the generated sCTs.

For the robust plan optimization, plans were optimized accounting for the nominal plan plus six different scenarios where the plan isocenter was shifted in fixed directions using the magnitude of the selected set-up uncertainty (Fredriksson et al., 2011). For the plan robustness evaluation, different dose scenarios were computed using the same magnitude of the set-up uncertainty in 26 fixed directions. Additionally, the information from all 26 scenarios per technique was combined in a voxel-wise minimum evaluation dose (Vw_{min}) by calculating the minimum dose per voxel in all dose scenarios. Plans were considered robust if in the Vw_{min} 98% of the ITV received at least 95% of the PD ($V_{95\%}$>98%) (Korevaar et al., 2016).

5.2.4 sCT evaluation

5.2.4.1 Image evaluation

The imaging evaluation of the original sCTs was done by calculating the voxel-wise mean error (ME) and the mean absolute error (MAE) in terms of HU against the corresponding planning-CT. The ME and MAE were calculated in a Boolean intersect of the automatic planning-CT and MRI bone, lungs, and soft-tissue volumes (*section 5.2.2.1*) to minimize the unavoidable HU differences due to random air pockets, posture and / or lungs volume differences due to breathing motion between consecutive CT and MR imaging sessions. In addition, the Dice similarity coefficient (DSC) was calculated for the segmented bone and lungs volumes on the planning-CT and MR images.

5.2.4.2 Dose evaluation

To validate the dosimetric accuracy of the sCTs, dose re-calculations of the VMAT and PBS plans were performed on the generated sCTs (sCT and sCT_{air}) and on a water bulk density sCT (sCT_{bulk}). The relative dose differences between the planning-CT and sCTs doses were calculated for the following DVH metrics: ITV $D_{98\%}$, $D_{50\%}$, $D_{2\%}$ and $V_{95\%}$, as well as OARs (kidneys, liver, spleen) mean dose (D_{mean}), $D_{50\%}$, $D_{20\%}$ and $D_{2\%}$. Moreover, the dose distributions of the treatment plans re-calculated on all sCTs were compared to that on the planning-CT by means of different 3D global gamma criteria: (3% / 3 mm) and (2% / 2 mm), with a 90%, 50% and 10% dose threshold.

5.3 Results

5.3.1 Image evaluation

Coronal and sagittal slices of the planning-CT, T2w-MRI and the original sCT are shown in *Figure 5.2* for one Pat_{up} (a - c) and one Pat_{low} (d - f). Automatic atlas-based segmentation time was approximately 3 min and MRI intensity to HU values conversion time was approximately 15 s per patient using a standard octa-core desktop computer with a 16 GB of RAM.

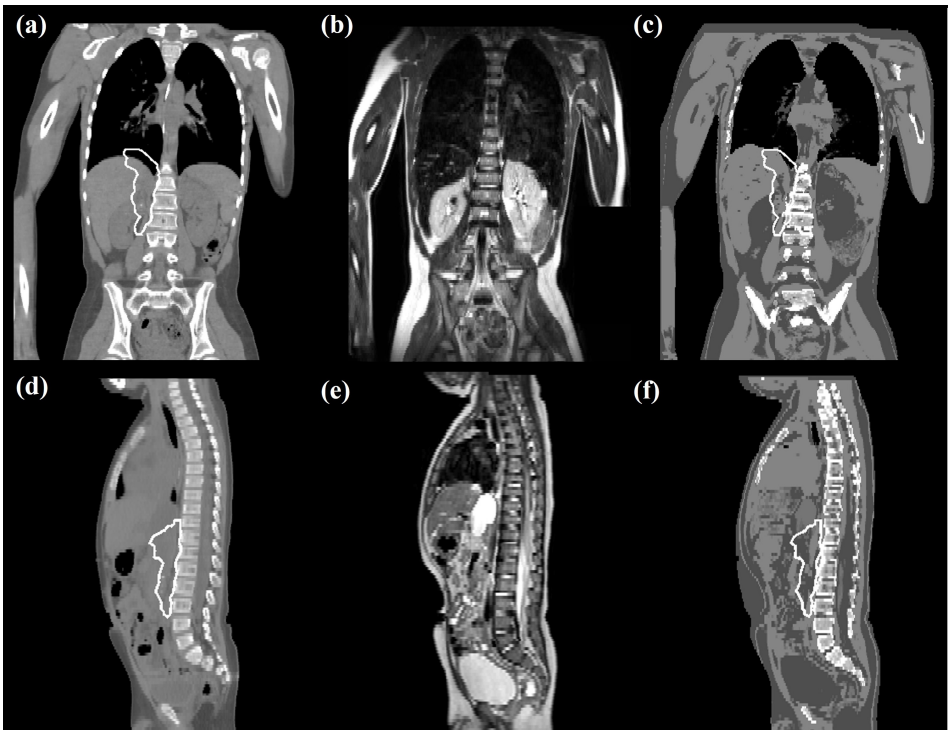

Figure 5.2 Coronal (top) and sagittal (bottom) slices of the planning-CT (a,d), the T2w-MRI (b,e) and the original sCT (c,f) for one Pat_{up} (top) and one Pat_{low} (bottom). The ITV is denoted in white.

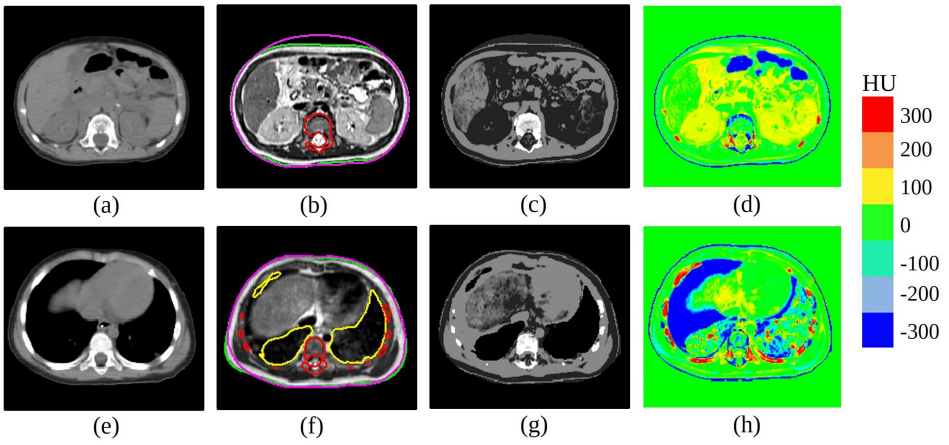

Figure 5.3 Transversal slices of the planning-CT (a,e), the T2w-MRI (b,f) and the original sCT (c,g) for one example patient. Body contours extracted from the planning-CT and MRI are presented in pink and green, respectively. The automatic atlas-based MRI contours for the bone and lungs are shown in red and yellow, respectively. HU differences between the planning-CT and the original sCT are presented in (d) and (h).

Despite the fact that images were acquired on the same day and with the patient in radiotherapy treatment position, the planning-CT and MR images demonstrated substantial inter-scan differences regarding either the size of the patient, the lungs volume and / or the presence of air pockets (*Figure 5.2, Figure 5.3*). Nevertheless, the original sCTs reproduced the appearance of the different tissue classes. The computed DSC was 0.90 ± 0.04 (range [0.82 ; 0.98]) and 0.74 ± 0.08 (range [0.54 ; 0.87]) for the bone and lungs volumes, respectively. The calculated ME was 11 ± 113 HU (range [-170 ; 207] HU) in the bone, -3 ± 65 HU (range [-165 ; 163] HU) in the lungs and 21 ± 11 HU (range [0 ; 55] HU) in the soft-tissue. The calculated MAE was 212 ± 40 HU (range [154 ; 291] HU) in the bone, 125 ± 24 HU (range [86 ; 198] HU) in the lungs and 53 ± 7 HU (range [42 ; 74] HU) in the soft-tissue. The largest HU discrepancies between the planning-CT and the original sCT images were seen in the lungs and in the ribs (*Figure 5.3*).

5.3.2 Dose evaluation

The relative dose differences of clinically relevant DVH parameters between the planning-CT and all sCT doses are illustrated using box-and-whisker plots in *Figure 5.4* for the ITV and in *Figure 5.5* for the OARs.

For the ITV, mean $V_{95\%}$ deviations to the planning-CT doses were 0.5 ± 1.4 % (range [0.0 ; 5.0] %) and 0.0 ± 0.0 % (range [0.0 ; 0.1] %) for the VMAT dose distributions re-calculated on the original sCTs and sCT_{air}s, respectively. For the PBS dose distributions, mean $V_{95\%}$ deviations were 0.0 ± 0.0 % (range [-0.1 ; 0.1] %) and 0.0 ± 0.0 % (range [-0.1 ; 0.0] %) for the original sCTs and sCT_{air}s, respectively. Large dosimetric differences were observed between the planning-CT and the original sCT for the VMAT dose distributions (*Figure 5.4*). The ITV coverage ($V_{95\%}$>99%) was not met for three patients due to the presence of large air pockets in the proximity of the ITV on the planning-CT and not on the sCT (*Figure 5.6*). When inserting the air pockets from the planning-CT on the sCT_{air}, the ITV dosimetric differences were considerably reduced (*Figure 5.4, Figure 5.6*). Given the use of posterior radiation fields, similar results were seen for the PBS plans re-calculated on both sCTs and sCT_{air}s (*Figure 5.4, Figure 5.6*).

For the OARs, the D_{mean} differences ranged between [-0.6 ; 1.2] % and [0.7 ; 0.1] % for the VMAT dose distributions re-calculated on the original sCTs and sCT_{air}s, respectively. For the PBS dose distributions, larger individual differences between the planning-CT and sCTs were observed (*Figure 5.5*). The range of D_{mean} differences was [-2.0 ; 2.6] % and [-2.6 ; 2.5] % for the original sCT and sCT_{air}, respectively. Furthermore, an increase up to 4% on the OARs $D_{2\%}$ was calculated for both delivery techniques for the Pat_{up}s in comparison to the Pat_{low}s (*Table 5.2*). This was possibly due to the large inter-scan differences seen regarding the lungs volume definition between the planning-CT and the MR images (*Figure 5.3*).

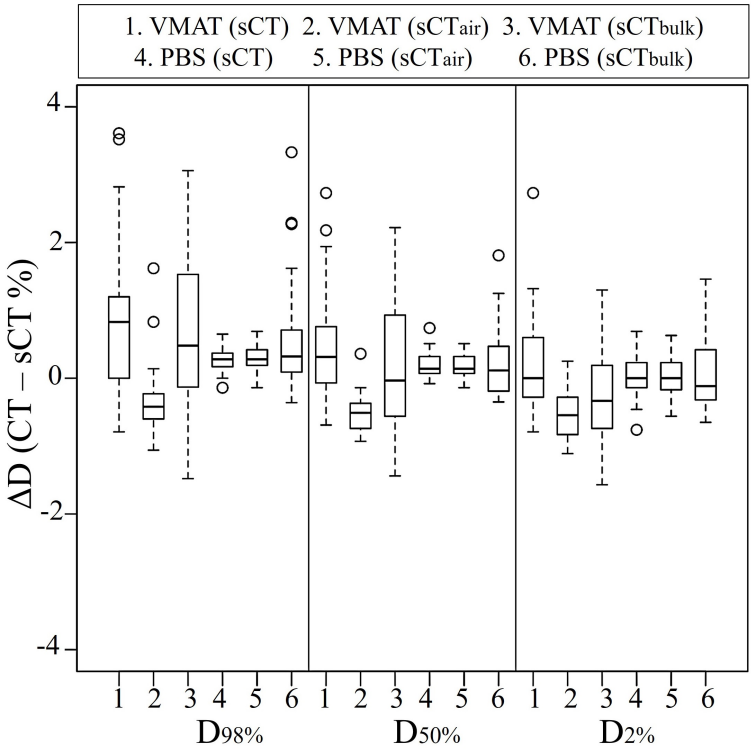

Figure 5.4 Box-and-whisker plots of the ITV DVH parameters differences between the planning-CT and sCT doses for the VMAT (1 - 3) and PBS (4 - 6) plans re-calculated on the original sCT (1,4), sCT_{air} (2,5) and sCT_{bulk} (3,6). Values are presented as a percentage of the respective PD.

The gamma pass-rates obtained between the planning-CT and all sCT doses are given in *Table 5.1.* Mean gamma pass-rates were above 87% for the generated sCTs independently of the considered gamma criteria. Focusing on the high-dose region (with a 90% dose cut-off), mean gamma pass-rates above 92% were achieved for both irradiation techniques. For the VMAT plans re-calculated on the original sCTs, the gamma pass-rates were lower than for the sCT_{air}s due to the difference of air volumes on the planning-CT and sCT, as mentioned previously. When inserting the air pockets from the planning-CT on the sCT_{air}, the gamma pass-rates were considerably increased. For the PBS plans, similar gamma pass-rates were obtained between the sCTs and sCT_{air}s. Moreover, large differences on the gamma pass-rates were denoted for the original sCTs between the Pat_{up}s and Pat_{low}s (*Table 5.2*). A decrease on the mean gamma pass-rates of 22 percentage points (pp) and 7 pp was observed for the Pat_{up}s compared to the Pat_{low}s for the VMAT and PBS dose distributions, respectively.

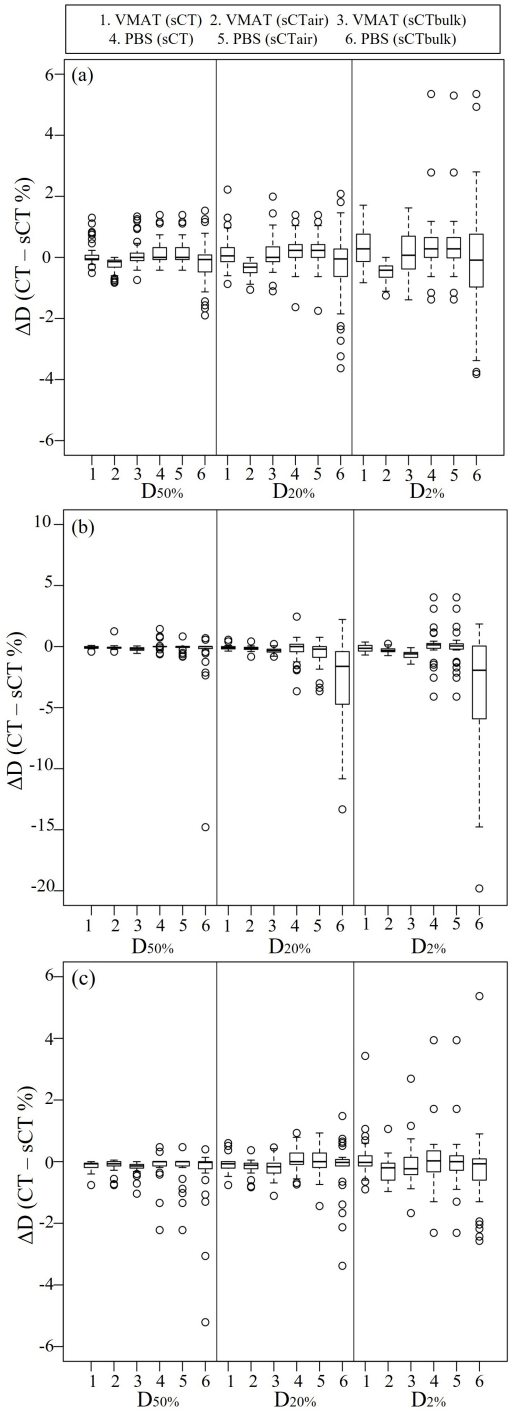

Figure 5.5 Box-and-whisker plots of the kidneys (a), liver (b) and spleen (c) DVH dosimetric differences at a given relative volume between the planning-CT and the original sCT (1,4), sCT_{air} (2,5) and sCT_{bulk} (3,6) for both VMAT (1 - 3) and PBS (4 - 6) dose distributions. Values are presented as a percentage of the respective PD.

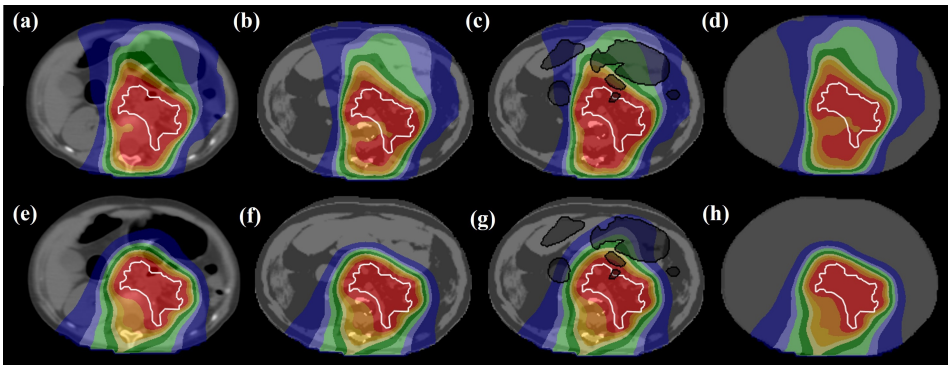

Figure 5.6 VMAT (top row) and PBS (bottom row) dose maps for doses re-calculated on the planning-CT (a,e), sCT (b,f), sCT_{air} (c,g) and sCT_{bulk} (d,h) for one Pat_{low}. The ITV contour is represented in white. The PD is 21.6 Gy and the 95% PD isodose is shown in red.

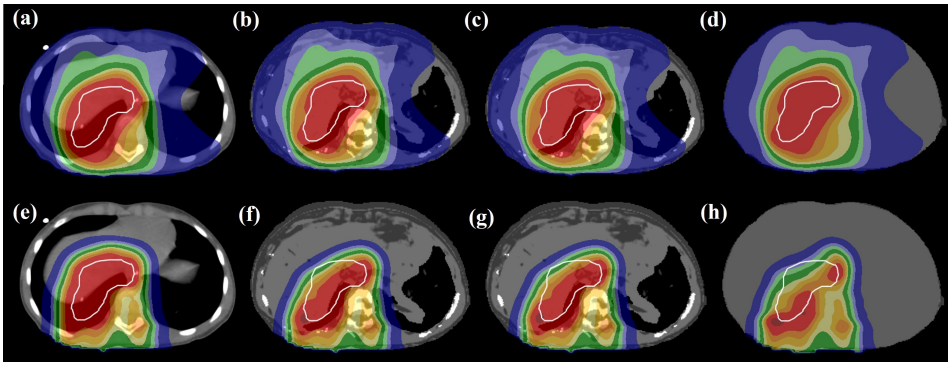

Figure 5.7 VMAT (top row) and PBS (bottom row) dose maps for doses re-calculated on the planning-CT (a,e), sCT (b,f), sCT_{air} (c,g) and sCT_{bulk} (d,h) for one Pat_{up}. The ITV contour is represented in white. The PD is 21.6 Gy and the 95% PD isodose is shown in red.

Moreover, the dosimetric accuracy of the sCT_{bulk}s was reduced in comparison to performing the dose re-calculations on the generated sCTs, especially for the PBS dose distributions. For the VMAT dose distributions, mean DVH differences to the planning-CT doses were up to 0.8% (maximum 5.0%) vs. 0.6% (maximum 1.6%) vs. 0.7% (maximum 3.1%) for the sCT, sCT_{air} and sCT_{bulk} doses, respectively. For the PBS dose distributions, mean DVH differences were up to 0.5% (maximum 5.4%) vs. 0.7% (maximum 5.3%) vs. 4% (maximum 19.8%) for the sCT, sCT_{air} and sCT_{bulk} doses, respectively. In addition, mean gamma pass-rates for the sCT_{bulk}s were considerably lower than for the generated sCTs, especially for the PBS plans (*Table 5.1*, $\leq$ 89%; minimum 53%). An increase on the mean gamma pass-rates up to 6 pp and 15 pp was achieved when using the generated sCTs compared to the sCT_{bulk}s for the VMAT and PBS dose distributions, respectively.

Table 5.1 Percentage of gamma pass-rates (%) for the comparison of planning-CT and sCT doses using different gamma criteria (mm / %) and dose thresholds (10%, 50% and 90%). *Abbreviations: SD= standard deviation.*

			Gamma pass-rate (CT & sCT) (%)					
			10%		50%		90%	
			mean ± SD	range	mean ± SD	range	mean ± SD	range
3mm / 3%	**VMAT**	sCT	99.3 ± 0.7	[97.2 ; 99.9]	97.6 ± 3.3	[86.0 ; 99.9]	97.6 ± 6.1	[74.8 ; 100]
		sCT_{air}	99.5 ± 0.4	[98.8 ; 99.9]	98.8 ± 1.2	[95.3 ; 99.9]	99.6 ± 1.7	[91.6 ; 100]
		sCT_{bulk}	99.1 ± 0.9	[96.2 ; 99.8]	97.3 ± 2.9	[88.0 ; 99.9]	98.0 ± 4.4	[84.2 ; 100]
	PBS	sCT	91.4 ± 4.3	[79.0 ; 99.5]	92.9 ± 4.3	[76.7 ; 99.4]	97.7 ± 3.9	[79.4 ; 100]
		sCT_{air}	92.1 ± 3.3	[84.0 ; 99.8]	92.7 ± 4.1	[76.6 ; 99.4]	97.5 ± 4.2	[79.3 ; 100]
		sCT_{bulk}	81.6 ± 4.0	[70.8 ; 89.8]	81.4 ± 5.4	[64.6 ; 88.5]	89.2 ± 7.8	[64.4 ; 99.0]
2mm / 2%	**VMAT**	sCT	97.7 ± 2.2	[92.8 ; 99.7]	93.6 ± 7.1	[73.1 ; 99.4]	92.4 ± 13.5	[46.8 ; 100]
		sCT_{air}	98.5 ± 1.6	[93.5 ; 99.7]	97.1 ± 2.5	[89.5 ; 99.3]	98.9 ± 3.4	[83.2 ; 100]
		sCT_{bulk}	97.3 ± 2.3	[92.5 ; 99.5]	93.2 ± 6.7	[76.5 ; 99.7]	93.1 ± 11.2	[60.1 ; 100]
	PBS	sCT	87.1 ± 5.4	[72.3 ; 98.6]	89.2 ± 5.3	[71.5 ; 97.8]	95.2 ± 5.2	[73.4 ; 100]
		sCT_{air}	88.1 ± 4.4	[73.8 ; 99.1]	89.2 ± 4.9	[71.4 ; 97.9]	95.1 ± 5.6	[73.1 ; 100]
		sCT_{bulk}	75.1 ± 4.6	[63.6 ; 82.1]	74.5 ± 6.5	[57.4 ; 83.6]	81.1 ± 10.4	[53.2 ; 95.7]

Table 5.2 Percentage of OARs $D_{2\%}$ differences and gamma pass-rates (%) for the comparison of planning-CT and sCT / sCT_{air} doses for the patients with tumors located on the upper (Pat_{up}s) and lower (Pat_{low}s) part of the abdomen.

			VMAT (%)				**PBS (%)**			
			Pat_{up}s (n=9)		**Pat_{low}s** (n=21)		**Pat_{up}s** (n=9)		**Pat_{low}s** (n=21)	
DVH	**Structure**		mean	range	mean	range	mean	range	mean	range
$D_{2\%}$	**Kidneys**	sCT	0.6	[-0.8 ; 1.7]	0.2	[-0.8 ; 1.7]	0.7	[-1.2 ; 5.4]	0.3	[-1.4 ; 2.8]
		sCT_{air}	-0.6	[-0.9 ; 0.1]	-0.5	[-1.3 ; 0.0]	0.7	[-1.2 ; 5.3]	0.3	[-1.4 ; 2.8]
	Liver	sCT	-0.1	[-0.7 ; 0.3]	-0.1	[-0.7 ; 0.4]	0.3	[-4.1 ; 4.0]	0.0	[-2.6 ; 0.4]
		sCT_{air}	-0.1	[-0.7 ; 0.2]	-0.4	[-0.7 ; 0.1]	0.0	[-4.1 ; 4.0]	0.1	[-2.6 ; 0.5]
	Spleen	sCT	0.9	[-0.1 ; 3.4]	-0.1	[-0.9 ; 0.6]	0.6	[-0.3 ; 3.9]	-0.1	[-2.3 ; 1.7]
		sCT_{air}	-0.2	[-0.9 ; 1.1]	-0.4	[-1.0 ; 0.0]	0.6	[-0.3 ; 3.9]	-0.1	[-2.3 ; 1.7]
Gamma	**Threshold**		mean	range	mean	range	mean	range	mean	range
2mm / 2%	**10%**	sCT	94.8	[92.8 ; 98.9]	98.7	[95.9 ; 99.7]	82.3	[72.3 ; 88.5]	88.6	[83.7 ; 98.6]
		sCT_{air}	96.4	[93.5 ; 99.5]	98.9	[96.3 ; 99.7]	83.3	[73.8 ; 88.5]	89.2	[84.6 ; 99.1]
	50%	sCT	85.2	[73.1 ; 95.5]	96.5	[86.5 ; 99.4]	84.5	[71.5 ; 92.7]	90.8	[86.9 ; 97.8]
		sCT_{air}	94.3	[89.5 ; 97.3]	97.7	[95.1 ; 99.3]	84.2	[71.4 ; 89.3]	90.3	[86.2 ; 97.9]
	90%	sCT	75.4	[46.8 ; 99.0]	97.3	[83.1 ; 100]	90.1	[73.4 ; 97.4]	96.5	[89.7 ; 100]
		sCT_{air}	95.6	[83.2 ; 100]	99.4	[94.6 ; 100]	89.4	[73.1 ; 96.2]	96.4	[87.9 ; 100]

5.4 Discussion

In this study, a method able to generate sCTs of the whole abdomen for pediatric patients using an automatic atlas-based segmentation combined with a triple-model technique for MRI intensity to HU values conversion was presented. To the authors' knowledge, the present study is the first evaluating the feasibility of generating sCTs for children aged from 2 to 7 years old and treated for abdominal cancer, which is one of the most challenging patient populations as a result of the highly individual anatomies among patients. Results showed that MRI-only photon and proton dose calculations on the generated sCTs were feasible.

The quantitative comparison of CT and sCT images is still under discussion. (Edmund and Nyholm, 2017) and (Johnstone et al., 2018) underline the importance of developing common standards for the quantification of the sCT accuracy for further improvements in this field. In this study, the sCT image accuracy was evaluated by using ME and MAE metrics. The mean ME was limited ($\leq$ 21 HU) for all tissue classes, indicating a good fit of the sCT method in general. Nevertheless, there was a considerable variation between patients predominantly for the bone. For this volume, a mean MAE of 212 HU was calculated, even though the reported mean ME was 11 HU. This can be explained by the intensity inhomogeneity detected on the MR images mostly caused by the large imaging volume compared to other body parts such as the pelvic region. Previous studies on the prostate have reported MAE differences in the bone of 97 HU for the dual-model technique (Koivula et al., 2016) and 134 HU for the atlas-based method (Dowling et al., 2015).

Additionally, high HU differences between the planning-CT and sCT images were detected in the ribs region and in the lungs. HU differences in the ribs can be explained by their small volume, by their poor visibility on the MRI and by their position variability among all patients. Moreover, HU differences in the lungs volume can be justified by the acquisition of both planning-CT and MR images during different breathing stages. Motion compensation strategies were employed during the planning-CT acquisition, by obtaining a 4D scan of a full breathing cycle, but not during the MRI acquisition. Smaller HU differences between the lungs volumes might potentially be achieved if matching breathing anatomies between MR and CT images had been evaluated. In this study, the clinical MR images were used as acquiring MRI sequences that are not included in the standard practice protocol is more difficult for children due to the stringent ethical regulations associated this patient group. Nevertheless, no significant motion artifacts were detected in the present MRI dataset and lungs segmentation was performed directly on the MR images (*Figure 5.3*). With more focus on the MRI intensity variation and fine tuning of MRI sequences, improved results could potentially be achieved for both atlas-based segmentation and intensity conversion models.

Besides the sCT imaging comparison, another requirement for the MRI-only workflow is the practical sCT method implementation: conversion speed, robustness, usability and amount of preliminary data needed for the atlas creation or network teaching - for which quantitative metrics maybe even more difficult to establish. Regarding the conversion speed, the most time-consuming task during this sCT generation method is the automatic atlas-based segmentation of bone and lungs. However, the sCT generation time is considerably fast (approximately 3 min taken fully by the automatic atlas-based segmentation step) and comparable to previous publications. The review by (Johnstone et al., 2018) presented generation times mainly under 5 min for voxel-wise methods and a larger variation from a couple of minutes to over an hour for atlas-based methods. Novel techniques based on deep learning can however provide sCT generation in the time scale of seconds (Maspero et al., 2018). Concerning the method's usability, the sCT generation workflow was designed to be highly accessible and easily adopted by most clinical users. However, the method's commissioning presents some limitations as every user needs to validate a suitable segmentation for the bone and lungs. Regarding the amount of preliminary data needed, a considerably feasible number of patients (n=24) was used for the atlas construction in this study. Nevertheless, the exact number of patients needed to assure an optimal ratio between automatic atlas-based segmentation time and accuracy still remains uncertain.

The sCT dosimetric accuracy was evaluated for both photon and proton irradiation techniques. Plans were optimized on the planning-CT and re-calculated on the sCT images. No optimization of the plans on the sCT and re-calculation of the same on the planning-CT was performed. This methodology was chosen as in literature it was previously shown that the CT - sCT dose comparison was invariant with respect to the optimization method used (Koivula et al., 2016). Results showed that MRI-only photon and proton dose calculations were feasible when using the generated sCTs for pediatric patients with abdominal tumors. Mean DVH differences on the ITV between the planning-CT and the original sCT doses were smaller than 0.8% for both delivery techniques. Individual differences were up to 5% and 0.7% for the VMAT and PBS dose distributions, respectively.

For the VMAT dose distributions, the ITV coverage was not met for three patients due to differences in the existence of air volumes between the planning-CT and the original sCT (*Figure 5.3*). The proposed sCT generation method performs an automatic muscle HU assignment to all air cavities seen on the MRI. After delineating the air from the planning-CT and using this contour for further dose calculations on the sCT_{air}, the target coverage was restored for these patients. For photon therapy, discrepancies between planned and delivered doses generated by the presence of random air pockets in the vicinity of the ITV need to be avoided. As a result, strategies such as performing density override of the gas pockets on the CT image during planning or using online daily re-planning in an MRI-guided photon workflow (Kontaxis et al., 2015a,b) might need to be implemented. For an MRI-guided workflow to be able to fully reproduce the patient's daily anatomy, an automatic air cavities delineation tool is essential for the investigated sCT generation method. This is particularly difficult to implement while using standard

MRI sequences as both cortical bone and air have no signal on MRI. However, in literature ultrashort echo time (UTE) pulse sequences were shown to improve the contrast between bone and the surrounding air and soft-tissue enabling a rough separation between these tissues classes (Johansson et al., 2011; Edmund et al., 2014). For PBS dose distributions, uncertainties related to the presence of random air pockets can be avoided by using posterior-oblique radiation fields. When using this beam configuration, results showed that dose differences to the planning-CT dose were similar for both original sCT and sCT_{air} images.

Mean gamma pass-rates for the generated sCTs doses ranged from [92 ; 100] % and [87 ; 98] % for VMAT and PBS dose distributions, respectively. Gamma pass-rates results for the PBS dose distributions were lower in comparison with studies in literature evaluating the sCT proton dose calculation accuracy for patients with prostate cancer (Koivula et al., 2016; Maspero et al., 2017b). For a 2 mm / 2% criterion and 10% dose threshold, (Koivula et al., 2016) and (Maspero et al., 2017b) reported a mean gamma pass-rate of 98%, in comparison with 87 - 88 % in this study. Two main reasons might be responsible for this lower PBS gamma pass-rate: (1) the large target size (mean 100 cc) and (2) the use of non-robust proton dose distributions to range uncertainty. For the patients included in this study, the ITV was extended throughout the whole abdomen in the CC direction. As a result, sCT dose re-calculations were subject to larger HU discrepancies detected between the planning-CT and MR images. Despite both planning-CT and MR images were acquired on the same day and in radiotherapy treatment position, the images demonstrated substantial inter-scan differences mostly regarding the lungs volume (mean lung DSC ~ 0.7). As a result, large relative dose deviations between the planning-CT and sCT doses were seen, especially for the Pat_{up}s (*Figure 5.7*). For the PBS dose distributions re-calculated on the generated sCTs, a decrease of 7 pp on the mean gamma pass-rates was calculated for the Pat_{up}s in comparison to Pat_{low}s. Moreover, PBS plans non-robust to range uncertainty were used in this study to assess the differences between the planning-CT and sCT doses in a setting more susceptible to density changes. However, protons can be more sensitive to uncertainties in CT densities and patient anatomy than common photons (Lomax, 2016). Robust planning is currently used in proton therapy to guarantee that the target coverage is maintained throughout the treatment by mitigating the effect of both range and set-up uncertainties. Thus, the proton dose calculation accuracy might be further improved when using a robust planning technique against both set-up and range uncertainties.

Furthermore, doses were re-calculated on a homogeneous water equivalent density sCT to evaluate the added value of using the generated sCTs for the dose calculations against using the sCT_{bulk}s. Dosimetric accuracy was reduced when using the sCT_{bulk}s for the dose re-calculations, especially for the PBS dose distributions with individual dose differences to the planning-CT dose up to 20%.

During RTP, another aspect that should be taken into account is the MRI geometric distortions and consequently the geometric accuracy of the sCTs. Gradient non-linearity distortions are the most dominant source of MRI distortions and have been shown to be more noticeable away from the scanner isocenter (Wang et al., 2004; Baldwin et al., 2007). Nevertheless, (Tijssen et al., 2017) showed that geometric distortions are only limited to 0.9 mm for a spherical volume with similar dimensions to a child's abdomen (30 cm in diameter). In this study, the patients' external contours between the planning-CT and sCT images were matched to reduce the influence of inter-scan differences due to patient set-up and anatomic differences on the dosimetric results (Prior et al., 2016; Gustafsson et al., 2017; Persson et al., 2017). Analyzing the geometric accuracy of the generated sCTs was out of the scope of this study, however the authors are aware that performing a match of the external contours between images might reduce the dosimetric differences seen. Future work will focus on evaluating the sCT geometric fidelity and patient position verification while using the generated sCTs for this patient group.

Similarly to the previously published dual-model technique (Korhonen et al., 2014; Koivula et al., 2016, 2017), the sCT generation method is robust in the absence of major artifacts and to general changes in MRI intensity levels and is suitable to be used for images acquired with different MR platforms and vendors. Improvement of the triple-model in comparison to the dual-model technique is the expanded usability when adding lung tissue for the sCT conversion model. In contrast, it is more sensitive to variations in the MRI intensity homogeneity as there are three distinct conversion curves for which all the MRI intensities have to correspond accordingly. The sCT dosimetric accuracy for targets directly located in the lungs was not tested in this study. Nevertheless, results were presented for both Pat_{up}s and Pat_{low}s. Despite that a feasible atlas-based segmentation of the lungs was possible when using T2w-MR images, a decrease in the dosimetric accuracy for the Pat_{up}s in comparison to the Pat_{low}s was seen. For the Pat_{up}s, these dosimetric differences might potentially be reduced if matching breathing anatomies between CT and MR images had been used. Future work should focus on improving the MRI acquisition by using motion mitigation techniques and on the development of dedicated MRI sequences for the sCT generation.

In summary, the results presented in this study are a promising step for the future clinical implementation of an MRI-only radiotherapy workflow to treat children with abdominal tumors. The employed method is able to generate sCTs with a large FOV, including the whole abdomen of the patient, which is essential for RTP. Accurate MRI-only photon dose calculations were achieved with the generated sCTs. However, the correct representation of air pockets in the bowel was found crucial. For MRI-only proton dose calculations, future research should focus in reducing anatomic differences between the CT and the generated sCTs and using robustness against range uncertainty during planning for a more realistic dose comparison.

5.5 Conclusion

In the present study, the feasibility of generating sCTs for children using standard T2w-MR images with a large FOV, including the whole abdomen of the patient, was evaluated. The proposed sCT generation method combines an automatic atlas-based segmentation with a triple-model technique for MRI intensity to HU values conversion for bone, lungs and soft-tissue classes. Results showed that MRI-only photon and proton dose calculations for pediatric patients with abdominal tumors were feasible. Clinical implementation of the proposed method will, however, require further investigations on improving the MRI acquisition, evaluating the sCT geometric fidelity and in using robust treatment planning strategies.

CHAPTER 6

Discussion

The use of radiotherapy or radiation therapy (RT) has historically been one of the great successes in childhood cancer treatments (O'Leary et al., 2008). Nevertheless, it is associated with challenges and adverse long-term complications that have been documented over the past years (Gibbs et al., 2006). As radiotherapy techniques are evolving rapidly, there is hope to improve current pediatric treatments by reducing the doses given to the normal tissue (NT). The aim of this thesis was to investigate the benefit of using novel radiotherapy techniques, such as magnetic resonance imaging (MRI)-guided photon and intensity-modulated proton therapy (IMPT) using a pencil beam scanning (PBS) delivery, to treat pediatric patients with abdominal cancer, more specific with Wilms' tumor (WT) or neuroblastoma (NBL).

In this chapter, the findings presented in previous sections will be shortly described and compared to other studies in literature while providing recommendations and speculations about future work. **Chapter 2** reported intra- and inter-fraction motion and patient set-up uncertainties in WT patients. Average uncertainties were found to be limited. Nevertheless, a large variability and a larger magnitude in the craniocaudal (CC) direction for the motion uncertainties were denoted among patients. In **chapter 3**, using the systematic and random errors calculated from computed tomography (CT) / cone-beam CT (CBCT) images (**chapter 2**) and from MRI data, planning target volume (PTV) margins were estimated for both CBCT- and MRI-guided workflows, respectively. *Section 6.1* will discuss uncertainties and the definition of safety margins during radiotherapy treatments in children with abdominal tumors.

Moreover, the potential dosimetric benefit of treating this patient category with recently introduced radiotherapy techniques, such as MRI-guided intensity-modulated radiation therapy ($IMRT_{MRI}$) (**chapter 3**) or robust intensity-modulated PBS (**chapter 4**), compared to the current clinical CBCT-guided volumetric modulated arc therapy (VMAT) workflow was evaluated. Results from **chapter 3** and **4** showed that both $IMRT_{MRI}$ and PBS dose distributions presented equal target coverage while sparing the NT to a higher extent compared to VMAT. *Section 6.2* will further discuss the dosimetric results of these two chapters.

In **chapter 5**, the feasibility of performing MRI-only photon and proton dose calculations using synthetic computed tomography (sCT) images was assessed. Accurate MRI-only photon and proton dose calculations were feasible with the proposed sCT generation method for children with abdominal tumors. The results of this study, the potential benefits and current challenges of using MRI-only planning will be discussed in *section 6.3*.

Additionally, *section 6.4* will focus on current needs and future work for the clinical implementation of MRI-guided proton radiotherapy treatments. Finally, in *section 6.5* the main conclusions of this thesis will be summarized.

6.1 Treatment uncertainties and safety margins estimation for abdominal tumors in childhood cancer

For an accurate safety margin estimation, a comprehensive assessment of the main radiotherapy treatment uncertainties, such as (1) delineation, (2) motion and (3) patient set-up uncertainties, is required.

6.1.1 Delineation uncertainty

Manual delineation of the target and organs at risk (OARs) is still the standard routine in most clinics, even though it is prone to intra- and inter-observer variability (Sharp et al., 2014). In addition, manual segmentation of three-dimensional (3D) abdominal images is labor-intensive and workload keeps increasing over the years as a result of having more structures to delineate and more imaging modalities to interpret (i.e CT, MRI, positron emission tomography (PET)). The estimation of the systematic delineation error for the target and / or OARs has been already presented in numerous adults studies using predominantly CT images (Vinod et al., 2016). In these studies, it was demonstrated that the delineation uncertainty contribution for the PTV margin estimation might be even bigger compared to the motion and patient set-up uncertainties (Deurloo et al., 2005; van Mourik et al., 2010; Versteijne et al., 2017). Despite CT is commonly employed in clinic for the target and OARs definition, the integration of MRI for the same purpose has been growing in the last few decades. As a result of the high soft-tissue contrast offered by MRI, the use of MR images alone, or together with CT, is expected to reduce the delineation uncertainty (Rasch et al., 2005; Khoo and Joon, 2006).

In children, delineation studies are scarce. Estimating this uncertainty for children is more difficult than for adults as a result of the small number of patients treated in each center, the broad spectrum of pediatric tumors, the lack of common guidelines and the individual patient's specific needs (Coles et al., 2003; Padovani et al., 2009). Nevertheless, (Padovani et al., 2009) has reported for WT patients that the inter-observer variability affected the target definition which resulted in deviations of the OARs dose distributions. In the last few years, auto-contouring has shown to be a promising tool to decrease both contouring time and inter-observer variability (Sharp et al., 2014). Re-

cent advances in deep learning, computational power and data availability allow for the auto-segmentation of clinical structures in a range of a few seconds (Lavdas et al., 2017; Gibson et al., 2018; Meyer et al., 2018).

6.1.2 Motion uncertainty

Motion in the abdomen is mainly caused by respiration (intra-fraction) and daily anatomical changes (inter-fraction), such as gastrointestinal filling and patient diameter differences. For both WT and NBL patients, the tumor is removed during surgery and clips are often placed at the tumor resection margins. At the radiotherapy department of the University Medical Center Utrecht (UMCU), these surgical clips are currently used as surrogates for the tumor bed (TB) motion during treatment. For the same patient category, the most relevant OARs are the kidneys, the liver, the spleen and the pancreas.

6.1.2.1 Intra-fraction

In **chapter 2**, TB and OARs intra-fraction motion uncertainty was found to be on average smaller than 3 mm (range [-3 ; 6] mm). In the last decade, several studies have already reported breathing motion uncertainties in children with abdominal tumors by using either four-dimensional (4D)-CT (Pai Panandiker et al., 2012; Kannan et al., 2017) or 4D-MR images (Uh et al., 2017).

Regarding the TB motion, the effect of respiration was estimated by using 4D-MRIs and using the whole clinical target volume (CTV) as motion surrogate (Uh et al., 2017). Larger displacements were reported by (Uh et al., 2017) compared to the results from **chapter 2** using 4D-CT images and the surgical clips as motion surrogates. Deviations in the results can be explained by the use of different imaging modalities and methodologies to estimate the TB motion.

Regarding the OARs motion, literature is available for the kidneys (Pai Panandiker et al., 2012; Kannan et al., 2017; Uh et al., 2017), spleen and liver (Kannan et al., 2017; Uh et al., 2017). An overview of the results from these studies compared to the results presented in this thesis are summarized in *Table 6.1*. In addition, (Huijskens et al., 2017) also reported the variability of the diaphragm position as a result of the intra- and inter-fraction breathing motion. As the respiratory motion of the diaphragm was not investigated in this thesis, this reference was excluded from *Table 6.1*. Deviations in the results between studies might be explained by differences in the imaging modalities used to assess the breathing motion (i.e 4D-CT, 4D-MRI) and differences in the patient cohort (i.e tumor location, patient age, number of patients, the use of general anesthesia (GA)).

6.1.2.2 Inter-fraction

In **chapter 2**, inter-fraction motion uncertainties were on average smaller than 1 mm but individual displacements measured on CBCT images ranged from -10 to 10 mm. The calculated displacements might be however overestimated due to differences between the CT and CBCT image acquisitions (i.e lower CBCT image quality, larger CBCT scanning time, no motion compensation strategies applied during CBCT acquisition) which may influence the contour baseline position and boundary visibility on the images.

In literature, the inter-fraction motion uncertainty was already reported for the TB (Nazmy et al., 2012) and OARs (Nazmy et al., 2012; Huijskens et al., 2015, 2018) using daily CBCT images as well. An overview of the results from these studies compared to the results presented in **chapter 2** are summarized in *Table 6.2.* As (Nazmy et al., 2012) only reported minimum and maximum displacements, this reference was excluded from *Table 6.2.* Compared to (Nazmy et al., 2012), (1) larger TB and (2) smaller OARs maximum displacements were found in **chapter 2**. Deviations might be explained by the choice of different methodologies: (1) the use of the whole CTV volume rather than surgical clips as surrogate for the TB motion and (2) the use of the upper and lower poles instead of the center of mass as surrogates for the OARs motion. Compared to (Huijskens et al., 2015, 2018), despite deviations were found between the mean OARs displacements, the range of motion was comparable (mostly within [-10, 10 mm]) and larger for the CC direction.

Table 6.1 Summary of the mean intra-fraction center of mass (CoM) displacements (in mm) measured for selected OARs (right kidney, left kidney, liver and spleen) for abdominal pediatric tumors in **chapter 2** and in studies from literature (Pai Panandiker et al., 2012; Kannan et al., 2017; Uh et al., 2017).

Reference	**Patient** (age range, number)		**Mean CoM displacements** (mm)			
			Kidney R	**Kidney L**	**Liver**	**Spleen**
Chapter 2	(1-8 years, n=15)	**LR**	0.0	0.0	-0.1	-1.3
Pai Panandiker et al., 2012	(1.5-10 years, n=15)		0.7	0.7		
Kannan et al., 2017	(2-18 years, n=20)		0.3	0.4	-0.8	1.0
Uh et al., 2017	(1-8 years, n=17)		0.5	0.5	0.9	1.4
Chapter 2	(1-8 years, n=15)	**AP**	0.1	0.1	1.0	0.9
Pai Panandiker et al., 2012	(1.5-10 years, n=15)		0.7	0.7		
Kannan et al., 2017	(2-18 years, n=20)		0.4	0.4	0.4	0.4
Uh et al., 2017	(1-8 years, n=17)		0.8	0.6	1.2	1.0
Chapter 2	(1-8 years, n=15)	**CC**	0.6	0.6	3.0	3.2
Pai Panandiker et al., 2012	(1.5-10 years, n=15)		1.9	1.7		
Kannan et al., 2017	(2-18 years, n=20)		-1.9	-1.4	-2.5	-3.1
Uh et al., 2017	(1-8 years, n=17)		2.3	1.6	3.2	3.0

Table 6.2 Summary of the mean inter-fraction center of mass (CoM) displacements (in mm) measured for selected OARs (right kidney, left kidney, liver and spleen) for abdominal pediatric tumors in **chapter 2** and in studies from literature (Huijskens et al. 2015, 2018).

Reference	Patient (Age range, number)		Mean CoM displacements (mm)			
			Kidney R	Kidney L	Liver	Spleen
Chapter 2	(1-8 years, n=15)	**LR**	0.1	0.1	1.2	0.5
Huijskens et al., 2015	(2-18 years, n=39)		0.6	-0.6		
Huijskens et al., 2018	(2-18 years, n=20)		-0.6	0.4	0.4	0.8
Chapter 2	(1-8 years, n=15)	**AP**	0.4	0.4	-0.1	-0.2
Huijskens et al., 2015	(2-18 years, n=39)		0.0	0.0		
Huijskens et al., 2018	(2-18 years, n=20)		-0.4	-0.4	1.0	0.0
Chapter 2	(1-8 years, n=15)	**CC**	-0.2	-0.2	-0.2	-1.0
Huijskens et al., 2015	(2-18 years, n=39)		0.5	1.5		
Huijskens et al., 2018	(2-18 years, n=20)		0.7	0.4	-0.1	0.8

6.1.2.3 Factors influencing motion

In literature, several studies have hypothesized that the use of GA and patient-specific factors (i.e age, height, weight) might influence the magnitude of the motion uncertainties (Pai Panandiker et al., 2012; Kannan et al., 2017; Huijskens et al., 2015, 2017). (Pai Panandiker et al., 2012) reported that the kidney intra-fraction motion uncertainty was significantly smaller for patients treated with GA. They also concluded that renal motion had a significant correlation with the patient age and height. Nevertheless, in this thesis and in the remaining studies (Kannan et al., 2017; Huijskens et al., 2015, 2017), no strong correlation was found between motion uncertainties and the use of GA and / or patient-specific factors (i.e age, height, weight). In addition, the relation between the motion uncertainties and the nephrectomy side for WT patients was also determined in this thesis. Results showed significant differences for the liver and spleen motion with the nephrectomy side in the CC direction.

Despite no statistical significance between motion uncertainties and the use of GA and / or patient-specific factors (i.e age, height, weight) was found in this thesis, a larger patient cohort is still needed to confirm these results. In literature, (van Dijk et al., 2017) have shown that renal and diaphragmatic motion were significantly smaller in children compared to adults. Nevertheless, they also conclude that not only age and height might influence the magnitude of the motion uncertainties but also different body physiques (i.e stature, fat, tissue elasticity). Accordingly, results from these studies (**chapter 2**, Kannan et al., 2017; Huijskens et al., 2015, 2017; van Dijk et al., 2017) suggest that motion is patient-specific. For this reason, a patient-specific internal target volume (ITV) and planning risk volumes (PRVs) are commonly employed at the UMCU to account for the effects of motion uncertainties during radiotherapy treatment. Clinically, target and OARs respiratory motion is estimated by measuring surgical clips and contour displacements on the patient 4D-CT image, respectively. In literature, the use of a single pre-treatment 4D-CT was shown to be a good indicator for the estimation of the breathing motion in children suggesting the use of this routine worldwide to treat this patient

category (Huijskens et al., 2019). In addition, the impact of motion uncertainties on the planned dose distributions for photon and proton irradiation techniques (**chapter 4**) will be further discussed in *section 6.2*.

6.1.3 Set-up uncertainty

The use of daily imaging for patient position verification can minimize or even eliminate set-up uncertainties during treatment. In **chapter 2**, these uncertainties were found to be negligible when using online CBCT images and the bony anatomy as surrogate for the patient position. Moreover, patients were immobilized supine in a vacuum mattress and GA was administrated for patients younger than 5 years to assure patient position stability and reproducibility during treatment delivery. Similar observations were found by (Beltran et al., 2010).

As the target is not clearly visible on the CBCT images due to their poor soft-tissue contrast, at the UMCU online patient position verification for children is performed using the bony anatomy. To better quantify the target position variations induced by deformations, target-based position verification using the surgical clips as surrogates should be investigated. Nevertheless, in order to match the clips position between the planning-CT and CBCTs, high image quality for the CBCT images would be required. This is more critical for pediatric patients as the imaging dose is often reduced for radiation protection. However, the use of fiducial markers for patient positioning corrections was shown to be feasible in abdominal cancer adults patients (Nederveen et al., 2000; van der Heide et al., 2007; Greer et al., 2008). Additionally, future treatments on MRI-guided systems are expected to eliminate uncertainties related to patient set-up due to the better soft-tissue contrast and the performance of online re-planning with fast re-optimization methods (Kontaxis et al., 2015a,b, 2017a,b).

6.1.4 Safety margins estimation

Independent of the irradiation technique, the use of safety margins to compensate for error sources during both treatment preparation and delivery is standardly employed in clinic. Nevertheless, the selected target and OARs margins are greatly dependent on the planning strategy, image-guidance used during treatment and institutional / individual experience (Alcorn et al., 2014).

Current protocols for pediatric abdominal tumors recommend the use of an isotropic margin around the CTV ranging from 5 mm, for NBL, to 10 mm, for WT patients (de Kraker et al., 2001; SKION, 2015). Despite the availability of these protocols, for both WT and NBL photon radiotherapy treatments at the UMCU, a PTV margin of 5 mm is employed around a patient-specific ITV. ITV expansions are individualized for each orthogonal direction and determined by estimating the TB breathing motion on the patient 4D-CT image. Clinical ITV expansions can go up to 2 mm in the CC direction and up to 1 mm in the left-right (LR) and anterior-posterior (AP) directions, depending on the patient.

In **chapter 3**, imaging data of WT patients demonstrated that the ITV-PTV margin can be reduced down to half, compared to the SIOP-2001 protocol, when using an online CBCT-guided workflow. It is worth to mention that the SIOP-2001 protocol was developed long before IGRT was widely available (de Kraker et al., 2001). The estimated 5 mm ITV-PTV margin in **chapter 3** is in line with the current standard clinical practice at the UMCU for these patients. Moreover, an isotropic reduction of the ITV-PTV margin by 2 mm was calculated when using an MRI-guided compared to a CBCT-guided workflow. For both workflows, margins were determined accounting for the overall treatment chain geometric accuracy, inter-fraction motion and patient set-up uncertainties. To be able to clinically validate the estimated expansions in this thesis, an assessment of the delineation uncertainty and a larger patient cohort would still be required (Biau et al., 2008). Having a reasonably large set of imaging data is particularly difficult for children due to the small number of patients treated in each center and the large variability in cancer types. In addition, for a more accurate estimation of the safety margins to use in an MRI-guided workflow, patient data obtained from clinical MRI-guided treatments would be required. Nevertheless, pediatric cases have not yet been treated in current clinical MRI-linear accelerator (MRI-linac) systems (Mutic and Dempsey, 2014; Raaymakers et al., 2017). In this thesis, for the MRI-guided workflow null inter-fraction uncertainties were assumed as a result of the possibility of performing online daily re-planning on the MRI-linac systems (Kontaxis et al., 2015a,b). Nonetheless, residual errors resulting from the daily plan re-optimization and estimation of the Hounsfield units (HUs) from the MR images might still occur. The dosimetric accuracy of performing MRI-only dose calculations (**chapter 5**) will be further discussed in *section 6.3*. Additionally, the potential dosimetric benefit of treating children with abdominal tumors with MRI-guided instead of CBCT-guided photon radiotherapy (**chapter 3**) will be discussed in *section 6.2*.

Moreover, current pediatric protocols do not give recommendations on the use of PRV margins. In literature, (McKenzie et al., 2002) showed that the use of PRV margins can enable a better OARs sparing as motion information is taken into account during RT plan optimization. In this thesis, the magnitude of the PRV expansions for this patient group were not estimated. Nevertheless, at the radiotherapy department of UMCU, PRV margins to compensate for the respiratory motion are currently determined for this patient category using the patient 4D-CT image. Clinical PRV expansions can go up to 3 mm in the CC direction and up to 2 mm in the LR and AP directions, depending on the patient and organ.

Due to the wide distribution of motion uncertainties found between patients during image-guided radiation therapy (IGRT) treatments (**chapter 2**), the use of patient-specific and anisotropic safety margins can be recommended for both target and OARs. Furthermore, the large variability of patient-specific factors (i.e age, height, weight) in pediatric cohorts and their lack of correlation with treatment uncertainties makes the generalization of margins currently not feasible (Huijskens et al., 2015).

6.2 Dosimetric comparison of novel radiotherapy techniques for abdominal tumors in children

WT and NBL patients are currently treated at the radiotherapy department of UMCU with a CBCT-guided VMAT workflow. With novel techniques such as $IMRT_{MRI}$ (**chapter 3**) and robust intensity-modulated PBS (**chapter 4**), a better dosimetric sparing of the OARs and NT can be potentially achieved.

6.2.1 MRI-guided photon treatments ($IMRT_{MRI}$)

Compared to VMAT, $IMRT_{MRI}$ treatments provided the reduction of the PTV margin (*section 6.1.4*) and consequently the significant decrease of both OARs doses and NT volume receiving dose values comparable to the target dose ($V_{95\%}$). For the best-case scenario of $IMRT_{MRI}$ treatments (using a 1 mm PTV margin), the average reduction of the mean dose (D_{mean}) to the OARs was down to 11% (range [-2 ; 22] %) compared to VMAT (using a clinical 5 mm PTV margin).

Besides the PTV margin, the beam energy and configuration and the chosen delivery technique might also impact the quality of the final dose distribution. Currently, only an IMRT delivery is available in the MRI-linac devices (Raaymakers et al., 2017). In this thesis, it was shown that NT doses were significantly affected by the delivery technique (VMAT vs. IMRT). As VMAT requires less monitor units (MUs) and shorter treatment delivery times than IMRT, a similar or even better NT sparing is expected with VMAT (Otto, 2008). When using the same PTV expansion, a reduction of the NT integral dose down to 3% was found with VMAT compared to IMRT. Thus, improvements on the NT dosimetric sparing might still be possible by implementing a VMAT delivery on the MRI-linac systems. At the UMCU, the benefits introduced by this functionality are currently being investigated by (Kontaxis et al., 2018). To the author's knowledge, no other studies in literature evaluating the dosimetric impact of treating pediatric patients with MRI-linacs exist. Despite that the $IMRT_{MRI}$ workflow is shown to be dosimetrically more favorable for these patients than the current clinical VMAT workflow, MRI-linac devices are not yet widely available for clinical use which might be considered a limitation.

6.2.2 Robust intensity-modulated PBS

Both 3D ITV-based robustly optimized VMAT and intensity-modulated PBS dose distributions presented comparable target coverage while a significantly better OARs and NT dosimetric sparing was achieved with PBS. The average reduction of the OARs D_{mean} was down to 23% (range [2 ; 40] %) with PBS compared to VMAT.

For this patient group, several studies in literature have already reported the dosimetric benefits of PBS against conventional radiotherapy with anteriorposterior-posterioranterior (AP-PA) irradiation (Hillbrand et al., 2008; Vogel et al., 2017), 3D conformal radiotherapy (Kristensen et al., 2015) and IMRT (Hillbrand et al., 2008; Hattangadi et al., 2011). A

common limitation of these publications is the use of a PTV-based optimization instead of a robust optimization to account for the effect of both set-up and range uncertainties on the planned PBS dose distributions. In literature, a PTV-based approach was already proven to be insufficient for this purpose (Lomax, 2008a,b; Albertini et al., 2011; Liu et al., 2012, 2013). In proton therapy, range uncertainties can generate severe effects on the delivered dose as proton path length changes result in displacements of the Bragg peak dose fall-off (Unkelbach et al., 2007; Lomax, 2008a,b). During proton delivery, deviations introduced by (1) inter-fraction patient anatomical changes (i.e gastrointestinal filling), (2) intra-fraction patient anatomical changes (i.e breathing motion), (3) inter-play effects (i.e time dependence on the delivery of each pencil beam) and (4) machine errors (i.e influencing spot position, delivered MUs per spot, spot energy), can particularly compromise the robustness of PBS dose distributions (Lomax, 2016). In this thesis, the effects of (1) and (2 - 4) on the planned VMAT (1) and PBS (1 - 4) dose distributions were evaluated separately. Moreover, being aware that VMAT plan optimization is clinically done with a PTV approach, differences between PTV-based and ITV-based robustly optimized VMAT dose distributions were also calculated. No significant differences were found for the majority of the evaluated dose-volume histogram (DVH) parameters.

6.2.2.1 Impact of inter-fraction anatomical changes

To assess the effect of inter-fraction anatomical changes on the planned 3D VMAT and PBS dose distributions (1), fractional doses were re-calculated using CBCT images. For the estimation of the HUs from the CBCTs, the planning-CT was deformably registered to each CBCT (de Senneville et al., 2016). Similar methodologies have already been proposed in literature (Veiga et al., 2014, 2015; Kurz et al., 2015, 2016). Although the deformed CTs offer high HUs accuracy for the dose re-calculations, deformable image registration methods might yield incorrect contours due to more pronounced deformations and reduced CBCT soft-tissue contrast (Kurz et al., 2016). As a result of reducing the imaging dose for radiation protection in pediatric treatments, the CBCT image quality is even more limited in children compared to adults patients. Thus, a voxel-by-voxel accuracy cannot be assured when performing deformable image registration with the available CBCTs. For this reason, a rigid accumulation of the fractional doses was performed in this thesis. Despite neglecting daily deformations, the largest inter-fraction anatomical changes, such as patient diameter and gastrointestinal gas volume variations, were still accounted for.

Results from **chapter 4** showed ITV mean DVH parameters differences between planned and CBCT accumulated dose distributions smaller than 0.5% for both VMAT and PBS. Nevertheless, the ITV coverage was reduced in the accumulated VMAT dose distribution below the target prescription objective ($V_{95\%}$>99%) for one patient. Smaller differences were denoted for the PBS dose distributions as a result of the selected beam configuration / angles. With the use of patient-specific posterior-oblique radiation fields, the influence of inter-fraction anatomical changes can be avoided as the proton beams stop before reaching the anterior part of the abdomen.

At the UMCU, VMAT plans for pediatric abdominal tumors are currently optimized using a full-arc delivery to achieve both an acceptable target coverage and a homogeneous dose distribution for the vertebra volume adjacent to the target (Hoeben et al., 2019). Thus, planning strategies such as performing a CT density override of the gastrointestinal gas volumes or using online daily re-planning might be necessary to avoid large differences between planned and delivered VMAT doses for this patient category. For this goal, a method enabling fast CT synthesis directly from CBCT images without requiring the performance of manual adaptations of the patient anatomy (i.e corrections of the gastrointestinal gas pockets and body contours) is required. In the last few years, deep learning has become a promising solution for fast image-to-image translation. Methods enabling the translation of CBCT to CT images by means of deep learning were already successfully published for adult cancer indications (Kida et al., 2018; Kurz et al., 2018; Liang et al., 2018). Nevertheless, the performance of CBCT-based dose calculations using deep learning methods for pediatric patients still remains uncertain. As mentioned before, current limitations are the variability in age, height and weight within the pediatric cohorts and the lack of reasonably large amounts of imaging data for training the network. In the future, imaging data with appropriate image quality (i.e MRI) should be used to better estimate *in-silico* the target and OARs fractional doses while accounting for daily deformations

6.2.2.2 Impact of remaining disturbing effects

In literature, several studies have reported the robustness of PBS dose distributions in the presence of anatomical, set-up and / or range uncertainties for non-moving (Kraan et al., 2013; Park et al., 2013; McGowan et al., 2015; Malyapa et al., 2016) and moving targets (Chang et al., 2014; Lin et al., 2015; Liu et al., 2015, 2016; Zeng et al., 2015, 2016; Inoue et al., 2016). Mostly due to breathing motion, 3D robust optimization approaches tend to be less effective in mitigating the impact of treatment uncertainties (Liu et al., 2015). Therefore, the added value of using 4D robust optimization and evaluation approaches was already established for moving targets (i.e lungs) (Chang et al., 2014; Lin et al., 2015; Liu et al., 2015, 2016).

The impact of disturbing effects (2 - 4) on the planned PBS dose distributions was evaluated in this thesis using a 4D robustness evaluation method (4DREM) (Ribeiro et al., 2019). Results from **chapter 4** showed that 3D robust PBS dose distributions were not only feasible to account for inter-fraction anatomical changes (1) but also for disturbing effects (2 - 4) for this patient category. Due to the target posterior location, the beam configuration chosen and the limited breathing motion seen for this patient group (**chapter 2**), the use of 3D robust optimized and evaluated PBS dose distributions is considered clinically suitable. Since 4D robust optimization and evaluation methods imply more manual work and optimization time, the avoidance of the clinical use of these routines to achieve robust PBS dose distributions presents an additional advantage of using intensity-modulated PBS to treat these patients.

6.2.3 VMAT vs. $IMRT_{MRI}$ vs. PBS

When compared to VMAT, both $IMRT_{MRI}$ and robust intensity-modulated PBS dose distributions presented equal target coverage while sparing the OARs and NT to a higher extent (*Figure 6.1* and *Figure 6.2*). Nevertheless, PBS dose distributions, using current clinical robustness settings (5 mm / ± 3%), proved to be more dosimetrically favorable to treat abdominal pediatric patients compared to the best-case scenario for photon irradiation, using $IMRT_{MRI}$ with a 1 mm PTV margin (*Figure 6.1* and *Figure 6.2*). For the WT patients (n=9), the average reduction of the OARs D_{mean} was down to 19% (range [-3 ; 34] %) with PBS compared to $IMRT_{MRI}$ (*Figure 6.2*). In addition, PBS dose distributions delivered by posterior-oblique radiation fields proved to be more robust against inter-fraction anatomical changes (≤ 2 cm, ≤ 455 ml) compared to photon radiotherapy treatments.

The results from this thesis provide substantial dosimetric information to help assessing the optimal referral patterns for children with abdominal tumors. From a dosimetric perspective, intensity-modulated PBS was shown to be currently the best available radiotherapy technique to treat this patient category. Nevertheless, whether the reported *in-silico* dosimetric gain and robustness against inter-fraction anatomical changes of PBS dose distributions is translated into any clinical benefit is uncertain at present time. Thus, long-term follow-up of a large cohort is mandatory to estimate the real clinical benefit of treating pediatric patients with intensity-modulated PBS.

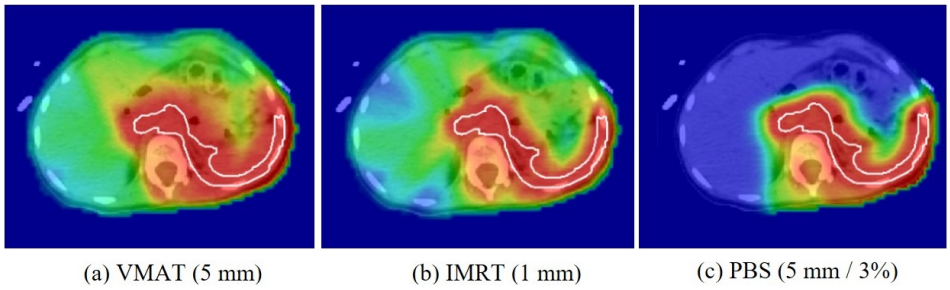

Figure 6.1 Transversal slice of a (a) VMAT (optimized with a ITV-PTV margin of 5 mm) (b) $IMRT_{MRI}$ (optimized with a ITV-PTV margin of 1 mm) and (c) PBS (ITV-based robustly optimized using 5 mm / 3% uncertainties) dose distributions for one WT patient (prescribed dose = 14.4 Gy, 95% isodose showed in red). The ITV is shown in white.

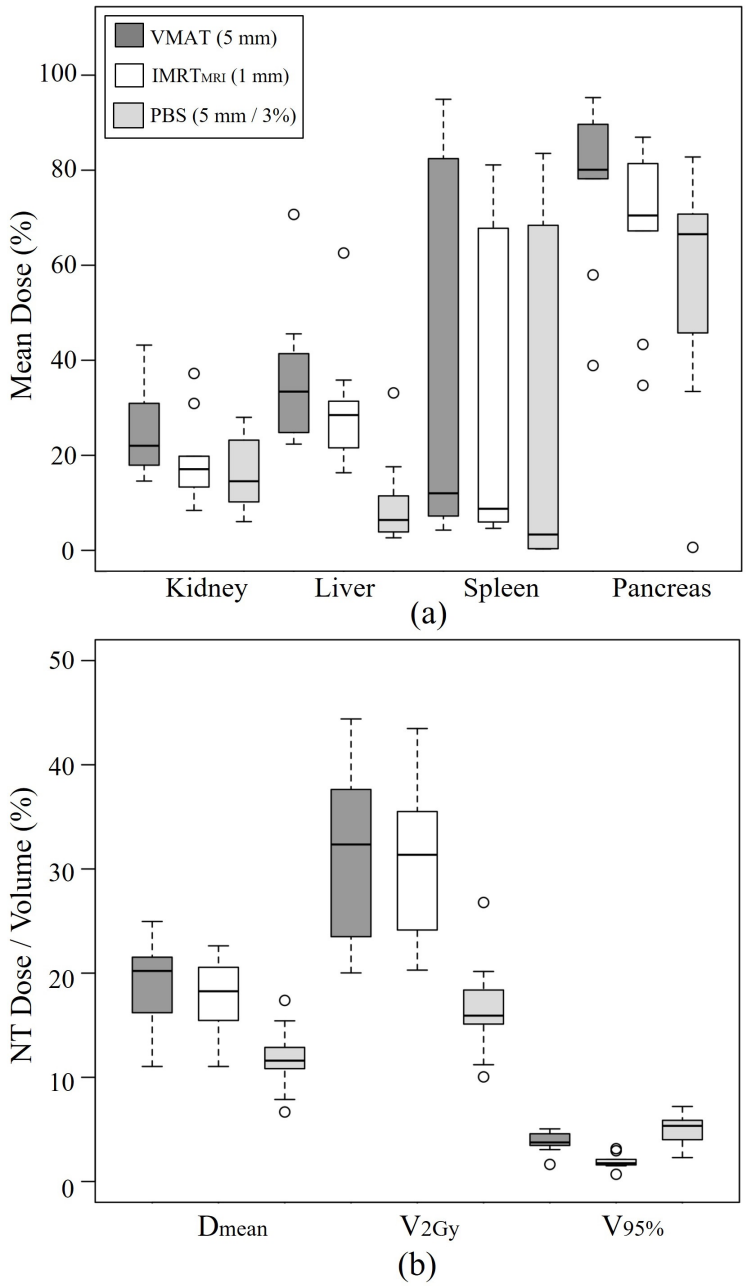

Figure 6.2 Boxplots denoting (a) the mean dose given to selected OARs and (b) the dose given to the NT by VMAT (optimized with a ITV-PTV margin of 5 mm, in dark grey), $IMRT_{MRI}$ (optimized with a ITV-PTV margin of 1 mm, in white) and PBS (ITV-based robustly optimized using 5 mm / 3% uncertainties, in light grey) dose distributions for WT patients (n=9).

6.3 MRI-only dose calculations

In the last decade, MRI-only radiotherapy treatment planning has been introduced into the clinic (Edmund and Nyholm, 2017; Tenhunen et al., 2018) promising to avoid systematic uncertainties arising from the CT - MR image registration and to decrease the patient radiation burden by skipping the acquisition of the planning-CT. Synthetic CT (sCT) images are currently used to perform dose calculations in an MRI-only planning situation (Edmund and Nyholm, 2017; Johnstone et al., 2018).

In **chapter 5**, a sCT generation method using standard T2w-MR images and relying on an automatic atlas-based segmentation of tissue classes followed by a voxel-based MRI intensity to HU values conversion was presented. According to the author's knowledge, this study was the first evaluating the feasibility of generating sCTs for pediatric patients aged from 2 to 7 years and treated for abdominal cancer. For this reason, results will be discussed and compared to available literature in prostate cancer adult patients. Several studies addressing the feasibility of performing photon dose calculations with sCT images exist (Eilertsen et al., 2008; Jonsson et al., 2010; Dowling et al., 2012, 2015; Siversson et al., 2015; Andreasen et al., 2016; Guerreiro et al., 2017; Koivula et al., 2017; Maspero et al., 2017a). Nevertheless, studies reporting the dosimetric accuracy of proton dose calculations with these images are still rare (Koivula et al., 2016; Maspero et al., 2017b).

6.3.1 Photon radiotherapy

Regarding the photon dose calculation accuracy, **chapter 5** reported average differences between the planning-CT and sCT doses smaller than 0.8% for the target (range [-1 ; 5] %) and smaller than 0.2% for the OARs (range [-1 ; 3] %). Larger dosimetric differences for the ITV were justified by gastrointestinal filling differences between the planning-CT and sCT images since air pockets were classified automatically as muscle by the sCT generation method. Thus, the correct representation of the air pockets was found crucial as a full-arc irradiation delivery, which shoots through the bowel, is clinically employed for the VMAT plans. Similar observations were done by (Maspero et al., 2017a). During MRI-only planning for this patient category, an automatic air pockets segmentation tool might be necessary for the sCT generation method to be able to fully reproduce the patient's anatomy. This is particularly difficult to implement while using standard MRI sequences as cortical bone and air have no signal on MRI due to their short T2 relaxation time (Tyler et al., 2007). In literature, studies have already shown that ultrashort echo time (UTE) sequences can improve the contrast between bone, air and soft-tissue enabling a rough separation between these three tissue classes (Johansson et al., 2011; Jonsson et al., 2013; Edmund et al., 2014; Paradis et al., 2015). Nevertheless, the use of UTE sequences for the generation of sCT images has so far not been tested for abdominal pediatric patients (Johnstone et al., 2018).

Furthermore, when including the air contour delineated from the planning-CT on the sCT dose re-calculations, average ITV dosimetric differences were reduced to 0.6% (range [-1 ; 2] %). These results are in line with what was presented in literature for prostate patients using different sCT generation approaches (i.e bulk, atlas, voxel-based) (Eilertsen et al., 2008; Jonsson et al., 2010; Dowling et al., 2012, 2015; Siversson et al., 2015; Andreasen et al., 2016; Guerreiro et al., 2017; Koivula et al., 2017; Maspero et al., 2017a). At the radiotherapy department of UMCU, a vendor solution for the generation of sCT images tailored for prostate patients (MRCAT, prototype rev. 257, Philips Healthcare, Vantaa, Finland) is currently available for clinical use. Despite several commercial sCT generation solutions exist for the pelvic area (Siversson et al., 2015; Maspero et al., 2017a; Persson et al., 2017), nothing yet was proposed for any pediatric cancer indication.

6.3.2 Proton radiotherapy

Regarding the proton dose calculation accuracy, results from this thesis showed average differences between the planning-CT and sCT doses smaller than 0.3% for the target (range [-1 ; 1] %) and smaller than 0.2% for the OARs (range [-4 ; 5] %). Gamma pass-rates were on average 87% for a 2 mm and 2% criterion using a 10% dose threshold. For the same criterion, both (Koivula et al., 2016) and (Maspero et al., 2017b) reported a mean gamma pass-rate of 98%. The lower average gamma pass-rate found for this patient category might be explained by (1) the large abdominal target size (mean 100 cc) compared to the prostate and (2) the use of PBS dose distributions non-robust to range uncertainty. For both WT and NBL patients, the target commonly extends throughout the whole abdomen in the CC direction. Thus, sCT dose re-calculations were subjected to larger HU discrepancies detected between the planning-CT and MR images (i.e lungs volume). In addition, robustness against range uncertainty was not accounted for during the PBS plan optimization in order to assess the dosimetric differences in a setting more susceptible to density changes between the planning-CT and sCT images. Thus, the CT - sCT dose differences might be further reduced by: (1) minimizing anatomic differences between the planning-CT and the generated sCTs (i.e motion compensation strategies for the MRI acquisition) and (2) using robustness against both set-up and range uncertainties during PBS plan optimization for a more realistic dosimetric comparison. So far, no commercial sCT generation solutions have been proposed for MRI-only proton planning. Nonetheless, (Maspero et al., 2017b) showed that MRI-only proton dose calculations were feasible for adult patients with prostate cancer when using MRCAT, originally designated for photon radiotherapy.

6.3.3 Clinical perspective

Nowadays, guidelines for defining acceptable dosimetric tolerances while commissioning an MRI-only workflow are limited (Edmund and Nyholm, 2017). The majority of the publications in literature consider suitable a 2% dosimetric agreement between the planning-CT and sCT doses (Korsholm et al., 2014). Results from **chapter 5** showed that both MRI-only photon and proton dose calculations using the proposed sCT generation

method were feasible and mainly below this 2% dosimetric agreement. Nevertheless, the improvement of the current sCT dosimetric accuracy is still required for the proton dose calculations. As mentioned in *section 6.3.2*, this can potentially be achieved by (1) developing dedicated MRI sequences for the sCT generation and (2) using robust treatment planning strategies. Children with abdominal cancer are one of the most challenging patient populations as a result of the large field of view (FOV), including the whole abdomen, and highly individual anatomies among patients. Nonetheless, the results from **chapter 5** proved the added dosimetric benefit when using the generated sCTs compared to a simple homogeneous water bulk density assignment for both photon and proton dose re-calculations.

Besides the absence of the electron density (for photon radiotherapy) and the stopping power (for proton radiotherapy) information, the clinical implementation of an MRI-only workflow still presents a few of additional challenges. First, the staff needs to be trained and gain experience with using only MR images during treatment planning (Rai et al., 2017). Second, quality control of the MRI scanners should be performed on a regular basis to assess the MRI geometric integrity and image quality for either patient positioning (by means of sCT - CBCT registrations) and / or target and organs delineation (Rai et al., 2017). Depending on the treatment site, different demands on the sCT geometric accuracy exist (Nyholm and Jonsson, et al. 2014). When patient positioning is performed using the patient bony anatomy as reference, the demands for accurate sCT geometric fidelity are higher compared to when positioning is performed using internal fiducial markers (i.e prostate cancer). As suggested in *section 6.1.3*, target-based position verification, using surgical clips as surrogates, should be investigated for children treated for abdominal tumors. Additionally, publications have shown that the most dominant source of MRI distortions are gradient non-linearity distortions which are commonly more noticeable away from the scanner isocenter (Wang et al., 2004; Baldwin et al., 2007). At the UMCU, (Tijssen et al., 2017) reported that geometric distortions were less than 1 mm for a spherical volume with similar dimensions to a child's abdomen (~ 30 cm diameter). Analyzing the geometric accuracy of the generated sCTs was out of the scope of this thesis. However, the results from (Tijssen et al., 2017) showed that sCT images for children will be less prone to MRI distortions compared to adults which presents an advantage of performing MRI-only dose calculations for this patient category.

Another relevant application of MRI-only dose calculations is the use of sCTs not only during the planning stage but also during the treatment delivery. With MRI-guided radiotherapy, intra- and inter-fraction treatment uncertainties can be compensated by performing a real-time RT plan adaptation while acquiring MR images of the patient (Kontaxis et al., 2015a,b; Stemkens et al., 2016). One important hurdle to reach such a goal is the fast sCT generation to perform online dose calculations with the acquired MR images. Despite providing acceptable dose calculation accuracy, the current sCT methods present generation times mainly under 5 min for voxel-wise approaches and from a couple of minutes to over an hour for atlas-based routines (Johnstone et al., 2018). More recently, techniques for fast sCT generation (< 1 min) are being explored by deep learning methods (Han, 2017; Arabi et al., 2018; Chen et al., 2018; Dinkla et al., 2018;

Emami et al., 2018; Maspero et al., 2018). To date, the performance of deep learning methods for sCT generation using pediatric MR images remains unknown mainly due to the lack of reasonably large amounts of data to train the network.

6.4 Towards MRI-guided proton therapy

As suggested by (Raaymakers et al., 2008), there should exist a similar need for high-quality soft-tissue imaging for proton therapy as there is for current MRI-guided photon treatments. As a result of the high proton beam sensitivity to treatment uncertainties (i.e anatomical changes), the clinical implementation of MRI-guided proton therapy is expected to be even more beneficial than for photon therapy. This approach is not available yet, however efforts to prove the hardware and software feasibility of MRI-guided proton treatments have been carried out in the last decade (Oborn et al., 2017). Currently, two of the most relevant challenges for this workflow are the compensation of the influence of the magnetic field on the proton beam trajectory and consequently on the planned proton dose distribution.

In the presence of a magnetic field, the proton beam experiences both an energy loss and an energy-dependent electromagnetic deflection from its otherwise straight trajectory. As a result, the Bragg peak is expected to be displaced by a few up to several millimeters, depending on the initial beam energy and the strength of the magnetic field (Fuchs et al., 2017). In literature, several studies have already reported the proton beam deflection by uniform magnetic fields (range [0.35 ; 3] T) inside a water phantom using either Monte Carlo (MC) simulations (Raaymakers et al., 2008; Moteabbed et al., 2014) or analytical models (Wolf and Bortfeld, 2012; Schellhammer and Hoffmann, 2017). For a 90 MV proton beam, (Raaymakers et al 2008) reported that a 0.5 T and a 3 T magnetic fields produced a beam deflection of 1 mm and 5 mm, respectively. For the same field strength, the maximum deflection of a 200 MV beam was calculated to be 10 times larger than that of a 90 MV proton beam (Wolf and Bortfeld, 2012; Moteabbed et al., 2014; Schellhammer and Hoffmann, 2017). More recently, (Schellhammer et al., 2018a) measured proton beam trajectories experimentally using a homogeneous phantom placed inside a 0.95 T magnetic field and compared them to MC simulations. They concluded that the proton beam trajectory in a magnetic field can be both measured and accurately predicted by using MC.

The range of the Bragg peak displacements estimated in these studies (0 - 107 mm, using 60 - 250 MV proton energies and 0.35 - 3 T magnetic field strengths) cannot be neglected during treatment planning. In literature, (Moteabbed et al., 2014) showed that for magnetic fields up to 0.5 T, neither the target coverage or the OARs doses were affected during PBS dose calculation in several tumor sites (i.e prostate, lung, liver, spine, brain, skull-base). Nevertheless, the PBS dose distortions were more pronounced and of clinical concern (i.e target underdosage) for dose calculations in a presence of a 1.5 T magnetic field. In addition, the feasibility of optimizing patient-based PBS dose distributions in the presence of a 1.5 T magnetic field compared to those at 0 T has already been

studied using MC simulations by (Hartman et al., 2015). (Hartman et al., 2015) found that the impact of a 1.5 T magnetic field on intensity-modulated PBS dose distributions was negligible when accounting for the magnetic field during the optimization stage. Nevertheless, this evaluation was performed for small artificial targets and the patient body was assigned to have a water equivalent density. To confirm these results, a more realistic body anatomy should be used as the presence of bone and air can influence the proton beam energy loss.

Moreover, a common limitation of these two publications is the assumption of a static external magnetic field (i.e without fringe field effects). In literature, (Oborn et al., 2015) has shown that the fringe field of an MRI scanner (25 – 100 cm from the isocenter) can cause additional complex deviations of the proton beam trajectory. As a result, special requirements exist regarding the magnet design on MRI-guided proton systems in order to minimize the magnitude of fringe field effects on the proton beam deflection (Oborn et al., 2017). In literature, (Oborn et al., 2015) reported that a split-bore would be the ideal magnet design after modeling proton beam trajectories to the treatment isocenter using MC simulations. This configuration would allow for the proton beam to reach the patient from many angles without obstructions. More recently, (Schellhammer et al., 2018b) performed the first experimental set-up of a low-field open MRI scanner with a static research proton beam line. Results showed that simultaneous irradiation and beam-on MR imaging was technically feasible.

In summary, the results from these studies showed the dosimetric and technical feasibility of delivering acceptable proton dose distributions within the presence of magnetic fields (up to 1.5 T) serving as encouragement for future research towards the clinical implementation of MRI-guided proton systems. For children with abdominal cancer, future work should include evaluating the feasibility of performing clinical proton dose calculations in the presence of a magnetic field (*Figure 6.3*) and assessing the potential benefits of treating this patient category with MRI-guided proton therapy (i.e safety margins reduction, dosimetric sparing).

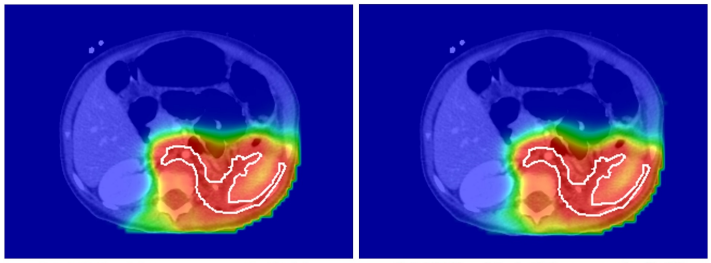

(a) PBS without magnetic field (b) PBS with 1.5T magnetic field

Figure 6.3 Example of intensity-modulated PBS dose distributions optimized robustly (a) without and (b) with a 1.5 T transverse magnetic field using a MC engine in RayStation treatment planning system for a WT patient (prescribed dose = 14.4 Gy, 95% isodose showed in red). The ITV is shown in white.

6.5 Conclusions

This thesis presented an *in-silico* investigation of the available radiotherapy techniques to treat pediatric patients with abdominal tumors (WT and NBL). In light of the work shown throughout **chapter 2** to **5**, the main conclusions are:

1. Average motion and patient set-up uncertainties during radiotherapy treatment were found to be limited. Nevertheless, the motion uncertainties were larger for the CC direction and a large variability of the measured displacements among patients was denoted. Thus, patient-specific and anisotropic safety margins for both target and OARs should be used during IGRT treatments.

2. When compared to clinical VMAT treatments, $IMRT_{MRI}$ and robust intensity-modulated PBS dose distributions presented equal target coverage while sparing the OARs and NT to a higher extent. Nevertheless PBS, using current clinical robustness settings (5 mm / ± 3%), was shown to be dosimetrically more favorable compared to the best-case scenario for $IMRT_{MRI}$, using a 1 mm PTV margin.

3. PBS dose distributions delivered by posterior-oblique radiation fields proved to be highly robust against inter-fraction anatomical variations (abdominal diameter changes $\leq$ 2 cm, gastrointestinal gas volume changes $\leq$ 455 ml). Compared to PBS, daily anatomical changes proved to affect more the target coverage of clinical VMAT dose distributions, using a full-arc delivery.

4. Accurate MRI-only photon and proton dose calculations were feasible with the proposed sCT generation method. The presented method was the first evaluating the feasibility of generating high-quality sCTs for children with a large FOV, including the whole abdomen of the patient, and for any other body parts than pelvis, head & neck and / or brain.

Finally, the work presented in this thesis contributed to build the rationale for introducing MRI-guided proton radiotherapy treatments for children with abdominal tumors by showing (1) the dosimetric benefit of current intensity-modulated PBS over available CBCT- and MRI-guided photon techniques and (2) the feasibility of performing MRI-only proton dose calculations. With MRI-guided proton therapy, further OARs and NT dose reductions might be foreseen compared to the currently available radiotherapy techniques. This technique seems to be particularly promising for the pediatric population, for whom there is a special concern for NT sparing to minimize the risk of radiation-induced complications after treatment.

CHAPTER 7

Summary

Wilms' tumor (WT) and neuroblastoma (NBL) belong to the most frequent abdominal tumors in children. Over the past few years, the survival rates of these patients have increased specially due to the use of a multimodality treatment including surgery, chemotherapy and radiotherapy. Despite radiotherapy treatments are reported to be beneficial for cancer survival, they are associated with an increased risk of toxicity to the normal tissue (NT). At the radiotherapy department of the University Medical Center Utrecht (UMCU), WT and NBL patients are currently treated using a volumetric modulated arc therapy (VMAT) technique. The main goal of this thesis was to investigate the benefit of using novel radiotherapy techniques, such as magnetic resonance imaging (MRI)-guided photon therapy and intensity-modulated proton therapy (IMPT), to treat this patient category.

To take advantage of the state-of-the-art radiotherapy techniques, a comprehensive assessment of the treatment uncertainties of abdominal target volumes is required. Despite image-guided radiation therapy (IGRT) is currently employed for several indications in pediatric patients, international guidelines on its optimal use are lacking. For WT patients undergoing flank irradiation, the current International Society of Paediatric Oncology (SIOP)-2001 protocol suggests a planning target volume (PTV) margin of 10 mm without image guidance. Thus, in **chapter 2** intra- and inter-fraction motion of the target and organs at risk (OARs) and patient set-up uncertainties during IGRT treatments were quantified. Four-dimensional computed tomography (4D-CT) and daily pre- and post-treatment cone-beam CT (CBCT) images of 15 WT patients were analyzed. Target (tumor bed marked by four surgical clips) and OARs (1) intra- and (2) inter-fraction motion uncertainties were estimated by calculating the center of mass displacements between (1) the maximum expiration and inspiration phases of the 4D-CT and (2) the planning-CT and the daily pre-treatment CBCTs, respectively. Moreover, translational and rotational bone off-sets between the planning-CT and the (1) post- and (2) pre-treatment CBCTs were recorded for the assessment of the patient set-up (1) intra- and (2) inter-fraction uncertainties, respectively. Average target and OARs intra- and inter-fraction motion ($\leq$ 3 mm) and patient set-up ($\leq$ 0.1 mm / 0.9°) uncertainties were found to be limited (*Table 2.1*).

Nevertheless, motion uncertainties had a wide distribution among patients and a larger magnitude for the craniocaudal direction (*Figure 2.3*). As a result, the use of patient-specific and anisotropic safety margins can be recommended for both target and OARs during IGRT.

Furthermore, the potential dosimetric benefit of treating abdominal pediatric tumors with novel IGRT techniques compared to the current clinical CBCT-guided VMAT workflow was determined: MRI-guided photon therapy using an intensity-modulated radiation therapy (IMRT) delivery (**chapter 3**) and robust CBCT-guided IMPT using a pencil beam scanning (PBS) delivery (**chapter 4**).

In **chapter 3**, the potential reduction of the PTV margin and its dosimetric impact when using the MRI-guided IMRT ($IMRT_{MRI}$) compared to the CBCT-guided VMAT workflow were assessed for a group of 15 WT patients. 4D-CT, MR and CBCT images acquired during treatment were used to estimate (1) geometric, (2) motion and (3) patient set-up systematic and random errors for both $IMRT_{MRI}$ and VMAT techniques. The PTV margin was calculated using the van Herk formula. Treatment plans were generated using five margin scenarios (PTV ± 0, 1 and 2 mm). In addition, to realistically model an MRI-guided treatment, $IMRT_{MRI}$ plans were optimized including the presence of a 1.5 T transverse magnetic field. The analysis of systematic and random errors resulted in a PTV margin reduction of 2 mm in each direction for the MRI- compared to the CBCT-guided workflow. For the estimated PTV margin, the target coverage was unaffected by the margin decrease and the average reduction of the OARs mean dose (D_{mean}) was down to 5% with $IMRT_{MRI}$ (*Table 3.3*). Between the clinical VMAT (using a PTV margin of 5 mm) and the best-case scenario of $IMRT_{MRI}$ (using a PTV margin of 1 mm), the maximum reduction of the OARs D_{mean} was 22%.

In **chapter 4**, the dosimetric sparing and robustness against inter-fraction anatomical changes between intensity-modulated PBS and VMAT dose distributions were evaluated for 20 pediatric patients treated for either WT or NBL. Clinical VMAT plans were based on a full-arc while PBS plans were based on 2 - 3 posterior-oblique radiation fields. Plans were robustly optimized on a patient-specific internal target volume (ITV) using a uniform 5 mm set-up and a ± 3% range (only for PBS) uncertainties. Significant better OARs sparing, with a maximum reduction of the D_{mean} of 40%, was achieved with PBS (*Figure 4.2*). To assess the PBS and VMAT robustness against daily anatomical changes, fractional dose re-calculations were performed using CBCT images. For the estimation of the Hounsfield units (HUs) from the CBCTs, the planning-CT was deformably registered to the CBCT images. Fractional doses were accumulated rigidly. Average ITV dose differences between the planned and accumulated dose distributions were smaller than 0.5% for both VMAT and PBS (*Table 4.2*). However, the ITV coverage ($V_{95\%} > 99\%$) was not reached for one patient for the accumulated VMAT dose distribution (*Figure 4.3*). In addition, larger OARs individual dose differences were found for VMAT compared to PBS (*Table 4.2*). PBS delivered by posterior-oblique radiation fields demonstrated to be more robust against anatomical inter-fraction changes compared to VMAT.

Results from **chapter 3** and **4** showed that both $IMRT_{MRI}$ and robust intensity-modulated PBS dose distributions presented equal target coverage while sparing the OARs and NT to a higher extent compared to VMAT. Nevertheless, PBS dose distributions proved to be dosimetrically more favorable to treat children with abdominal tumors. Compared to the best-case scenario of $IMRT_{MRI}$ treatments (using a PTV margin of 1 mm), an average reduction down to 19% of the OARs D_{mean} was estimated with PBS (using clinical robustness settings: 5 mm / ± 3%).

In **chapter 5**, the feasibility of performing MRI-only photon and proton dose calculations using synthetic CT images (sCT) was evaluated for 20 WT and NBL patients. The proposed sCT generation method relied on an automatic atlas-based segmentation of bone and lungs followed by an MRI intensity to HU values conversion using standard T2-weighted MR images. ITV-based VMAT and PBS dose distributions robustly optimized against a 5 mm set-up uncertainty were used to evaluate the sCT dose calculation accuracy. Average differences between planning-CT and sCT dose calculations for the ITV were ≤ 0.8% (maximum 5%) for VMAT and ≤ 0.3% (maximum 1%) for PBS. Average gamma pass-rates using a 2 mm / 2% criterion (10% dose threshold) were 98% for VMAT and 87% for PBS. The results from **chapter 5** showed that accurate MRI-only photon and proton dose calculations were feasible with the proposed sCT generation method. For MRI-only photon calculations, the larger dosimetric differences found on the ITV can be justified by bowel filling variations between the planning-CT and sCTs. For MRI-only proton calculations, future research should focus in reducing CT - sCT anatomic differences and using robustness against range uncertainty during treatment planning. Nonetheless, the proposed method was able to generate sCTs using standard T2-weigthed MR images for a challenging population (children aged from 2 to 7 years) and for a large field of view (from the lungs until the lower abdomen), which is essential for radiotherapy treatment planning.

The work presented in this thesis contributed to build the rationale for introducing MRI-guided proton radiotherapy treatments for pediatric patients with abdominal tumors by showing (1) the dosimetric benefit of current intensity-modulated PBS over available CBCT- and MRI-guided photon techniques and (2) the feasibility of performing MRI-only proton dose calculations. MRI-guided proton therapy is clinically not available yet, but shows promise for children for whom there is a special concern for NT sparing. Future work should include evaluating the feasibility of performing clinical proton dose calculations in the presence of a magnetic field and quantifying the potential dosimetric sparing with MRI-guided proton therapy treatments for this patient category.

CHAPTER 8

Samenvatting

Wilmstumoren (WT) en neuroblastoma's (NBL) behoren tot de meest voorkomende abdominale tumoren onder kinderen. Over de afgelopen jaren is de overlevingskans van deze patiënten toegenomen, wat voornamelijk te wijten is aan het gebruik van multimodale behandelingen met chirurgie, chemotherapie en radiotherapie. Hoewel studies laten zien dat radiotherapiebehandelingen van positieve invloed zijn op de overlevingskans, worden ze ook in verband gebracht met een verhoogd risico op toxiciteit van gezond weefsel (NT). Op de radiotherapie-afdeling van het Universitair Medisch Ventrum Utrecht (UMCU) worden WT en NBL patiënten momenteel behandeld met volumetric modulated arc therapy (VMAT). Het hoofddoel van dit proefschrift was te onderzoeken welk voordeel nieuwe radiotherapietechnieken zoals magnetic resonance imaging (MRI)-geleide fotontherapie en intensity-modulated protontherapie (IMPT) kunnen hebben voor de behandeling van deze patiënten.

Om deze state-of-the-art radiotherapietechnieken zo effectief mogelijk in te kunnen zetten, is een goede karakterisatie van onzekerheden bij behandelingen van abdominale doelvolumes nodig. Ondanks dat beeld-geleide radiotherapie (IGRT) momenteel gebruikt wordt voor verschillende inicaties bij pediatrische patiënten, is er nog een gebrek aan internationale richtlijnen die voorschrijven hoe IGRT het best kan worden toegepast. Voor WT patiënten die flankbestraling ondergaan zonder beeld-geleiding, schrijft het International Society of Paediatric Oncology (SIOP)-2001 protocol momenteel een planning target volume (PTV) voor met een 10 mm marge. Om die reden zijn in **hoofdstuk 2** intra- en interfractie beweging tijdens IGRT behandelingen gekwantificeerd en zijn de onzekerheden in de positionering van de patiënt bepaald. Hiervoor zijn vierdimensionale computed tomography (4D-CT) beelden en dagelijkse pre- en postbehandeling cone-beam CT (CBCT) beelden van 15 WT patiënten geanalyseerd. Intrafractie onzekerheden van het doelgebied (tumorbed gemarkeerd door vier chirurgische clips) en van de OARs zijn bepaald door op de 4D-CT het verschil in verplaatsing van het zwaartepunt tussen de maximale expiratie- en maximale inspiratiefase te berekenen. Interfractie onzekerheden zijn bepaald uit het verschil in zwaartepunt tussen de planning-CT en de dagelijkse CBCTs voor de behandeling. Verder zijn translatie- en rotatieverschillen van de botstructuur tussen de planning-CT en de CBCT voor en de CBCT na behandeling bepaald. Op die manier zijn respectievelijk intra- en interfractie onzekerheden in de

positionering van de patiënten bepaald. De gemiddelde intra- en interfractie beweging van het doelgebied en OARs (≤ 3 mm) en onzekerheden in de positionering (≤ 0.1 mm / ≤ 0.9^o) waren beperkt, zie *Tabel 2.1.* Desondanks was er veel variatie in onzekerheden door beweging tussen de patiënten en een grotere amplitude in de craniocaudale richting, zie *Figuur 2.3.* Daarom kan het gebruik van patiënt specifieke en anisotropische veiligheidsmarges worden aangeraden voor IGRT bij zowel het doelgebied als de OARs.

Vervolgens is onderzocht of nieuwe IGRT technieken een dosimetrisch voordeel kunnen hebben voor de behandeling van abdominale pediatrische tumoren ten opzichte van de huidige CBCT-geleide VMAT workflow. Hiervoor is gekeken naar MRI-geleide fotontherapie (**hoofdstuk 3**) en robuste CBCT-geleide IMPT waarbij de dosis wordt afgegeven met behulp van de pencil beam scanning (PBS) techniek (**hoofdstuk 4**).

In **hoofdstuk 3** is voor 15 WT patiënten de potentiële reductie van PTV marges en de bijbehorende dosimetrische impact onderzocht van MRI-geleide IMRT ($IMRT_{MRI}$) vergeleken met de huidige CBCT-geleide VMAT workflow. 4D-CT, MRI en CBCT scans zijn gebruikt om de systematische en toevallige fouten veroorzaakt door afwijkende geometrie, beweging en patiënt positionering te bepalen voor zowel $IMRT_{MRI}$ als VMAT. De PTV marges zijn berekend volgens de van Herk formule. Vervolgens zijn bestralingsplannen gemaakt voor vijf verschillende marge-scenario's: PTV ± 0, 1 and 2 mm. Om een MRI-geleide behandeling zo goed mogelijk te modelleren is rekening gehouden met een 1.5 T transversaal magnetisch veld in de optimalisatie van de $IMRT_{MRI}$ bestralingsplannen. De analyse van de systematische en toevallige fouten resulteerde in een PTV margereductie van 2 mm in alle richtingen voor de MRI-geleide workflow vergeleken met de CBCT-geleide workflow. Voor $IMRT_{MRI}$ bleef de dosisafgifte in het doelgebied onveranderd door de margereductie van het PTV terwijl de gemiddelde dosis (D_{mean}) in de OARs gereduceerd kon worden met 5%, zie *Tabel 3.3.* Tussen de klinische VMAT behandeling (met een PTV van 5 mm) en het best-case $IMRT_{MRI}$ scenario (met een PTV van 1 mm) was de maximale D_{mean} reductie 22%.

In **hoofdstuk 4** is de dosimetrische sparing en robuustheid voor interfractionele anatomische veranderingen onderzocht voor intensiteit-gemoduleerde PBS en VMAT dosisverdelingen bij 20 pediatrische patiënten die behandeld werden voor WT of NBL. De klinische VMAT plannen waren gebaseerd op een volledige boog terwijl de PBS plannen gebaseerd waren op 2 - 3 posterior-oblique bestralingsvelden. De plannen waren robuust geoptimaliseerd op een patiënt-specifiek intern doelvolume (ITV) met een uniforme onzekerheid in positionering van 5 mm en, voor PBS, een ± 3% onzekerheid in bereik. PBS leverde een significant betere sparing op van de OARs, met een maximale D_{mean} reductie van 40%, zie *Figuur 4.2.* Om de robuustheid van PBS en VMAT voor dagelijkse anatomieveranderingen te bepalen, waren fractionele herberekeningen van de dosis uitgevoerd op basis van de CBCT beelden. De Hounsfield waardes (HUs) voor de CBCTs waren verkregen door de planning-CT deformeerbaar te registreren op de CBCT beelden. De fractionele doses waren vervolgens rigide geaccumuleerd. Het gemiddelde dosisverschil tussen de geplande en geeaccumuleerde dosisverdeling was kleiner dan 0.5% voor zowel VMAT als PBS, zie *Tabel 4.2.* Voor een patiënt echter was het ITV niet volledig ($V_{95\%}$)

gedekt voor de geaccumuleerde VMAT dosisverdeling, zie *Figuur 4.3*. Bovendien waren grotere individuele dosisverschillen in de OARs gevonden voor VMAT in vergelijking met PBS (*Tabel 4.2*). PBS met posterior-oblique bestralingsvelden bleek robuster te zijn voor interfractionele anatomische veranderingen vergeleken met VMAT.

De resultaten van **hoofdstukken 3** en **4** laten zien dat de dosisverdelingen van $IMRT_{MRI}$ en intensiteit-gemoduleerde PBS een gelijke dosis geven in het doelgebied terwijl ze een grotere sparing opleveren van de OARs en NT vergeleken met de dosisverdelingen van VMAT. Dosimetrisch bleek PBS beter voor de behandeling van abdominale tumoren in kinderen. Vergeleken met het best-case scenario van $IMRT_{MRI}$ (met een PTV van 1 mm), kon een gemiddelde D_{mean} reductie van 19% in de OARs behaald worden met PBS, gebruik makend van de klinische robuustheid parameters: 5 mm / ± 3%.

In **hoofdstuk 5** is de haalbaarheid van MRI-only foton en proton dosiscalculatie door middel van synthetische CT (sCT) beelden geëvalueerd voor 20 WT en NBL patiënten. De voorgestelde methode om sCT beelden te genereren is gebaseerd op een automatische atlas segmentatie van de botstructuur en longen, gevolgd door een omzetting van MRI intensiteit naar HU met behulp van standaard T2-gewogen MR beelden. ITV-geaseerde VMAT en PBS dosisverdelingen die robuust geoptimaliseerd waren voor een 5 mm positioneringsonzekerheid, waren gebruikt om te evalueren hoe accuraat de op sCT gebaseerde dosiscalculaties zijn. De gemiddelde verschillen voor het ITV tussen dosiscalculaties op basis van de planning-CT en de sCT waren ≤ 0.8% (maximaal 5%) voor VMAT en ≤ 0.3% (maximaal 1%) voor PBS. De gemiddelde gamma pass-rates voor een 2 mm / 2% criterium (10% drempeldosis) waren 98% voor VMAT en 87% voor PBS. De resultaten van **hoofdstuk 5** hebben laten zien dat accurate MRI-only foton en proton dosiscalculaties mogelijk zijn met de voorgestelde sCT methode. Voor MRI-only foton calculaties zijn de grotere dosimetrische verschillen in het ITV te verklaren door variaties in darmvulling tussen de planning-CT en de sCTs. Voor MRI-only proton calculaties moeten in verder onderzoek de anatomische verschillen tussen CT en sCT geminimaliseerd worden en moet robuustheid voor bereikonzerheid worden meegenomen in de planningsfase. Desondanks was de voorgestelde methode in staat sCTs te genereren met standaard T2-gewogen MR beelden voor een ingewikkelde patiëntengroep (kinderen tussen twee en zeven jaar) en voor een groot field of view (longen tot onderaan het abdomen), wat essentieel is voor de planning van de behandeling.

De inhoud van dit proefschrift draagt bij aan de rationale van MRI-geleide radiotherapie behandelingen met protonen voor pediatrische patiënten met abdominale tumoren. Er is laten zien dat huidige intensiteit-gemoduleerde PBS een dosimetrisch voordeel heeft ten opzichte van beschikbare foton technieken en er is laten zien dat MRI-only dosiscalculaties voor protonen haalbaar zijn. MRI-geleide protontherapie is nog niet klinisch beschikbaar, maar belooft gunstig te zijn voor de behandeling van kinderen waarbij NT zoveel mogelijk gespaard moet blijven. Verder onderzoek moet gedaan worden naar de haalbaarheid van klinische dosiscalculaties voor protonen in de aanwezigheid van een magnetisch veld. Verder moet gekwantificeerd worden wat de potentiële dosimetrische besparingen zijn van MRI-geleide protontherapie voor deze patiëntengroep.

Bibliography

Acharya S, Fischer-Valuck BW, Kashani R, Parikh P, Yang D, Zhao T, Green O, Wooten O, Li HH, Hu Y, Rodriguez V, Olsen L, Robinson C, Michalski J, Mutic S and Olsen J 2016 Online Magnetic Resonance Image Guided Adaptive Radiation Therapy: First Clinical Applications. *Int. J. Radiat. Oncol. Biol. Phys.* 94(2):394-403.

Albertini F, Hug EB and Lomax AJ 2011 Is it necessary to plan with safety margins for actively scanned proton therapy? *Phys. Med. Biol.* 56(14):4399-413.

Alcorn SR, Chen MJ, Claude L, Dieckmann K, Ermoian RP, Ford EC, Malet C, MacDonald SM, Nechesnyuk AV, Nilsson K, Villar RC, Winey BA, Tryggestad EJ and Terezakis SA 2014 Practice patterns of photon and proton pediatric image guided radiation treatment: results from an International Pediatric Research consortium. *Pract. Radiat. Oncol.* 4(5):336-41.

Andreasen D, Van Leemput K and Edmund JM 2016 A patch-based pseudo-CT approach for MRI-only radiotherapy in the pelvis. *Med. Phys.* 43(8):4742.

Arabi H, Dowling JA, Burgos N, Han X, Greer PB, Koutsouvelis N and Zaidi H 2018 Comparative study of algorithms for synthetic CT generation from MRI: Consequences for MRI-guided radiation planning in the pelvic region. *Med. Phy.* 45(11):5218-33.

Baldwin LN, Wachowicz K, Thomas SD, Rivest R and Fallone BG 2007 Characterization, prediction, and correction of geometric distortion in 3 T MR images. *Med. Phys.* 34:388-99.

Beltran C, Pai Panandiker AS, Krasin MJ and Merchant TE 2010 Daily image-guided localization for neuroblastoma. *J. Appl. Clin. Med. Phys.* 11(4):162-9.

Bethe H 1930 Zur Theorie des Durchgangs schneller Korpuskularstrahlen durch Materie. *Annalen der Physik* 397(3):325-400.

Biau DJ, Kernéis S and Porcher R 2008 Statistics in Brief: The Importance of Sample Size in the Planning and Interpretation of Medical Research. *Clin. Orthop. Relat. Res.* 466(9):2282-8.

Bloch F 1933 Zur Bremsung rasch bewegter Teilchen beim Durchgang durch Materie. *Annalen der Physik* 408(3):285-320.

Bol GH, Kotte AN, van der Heide UA and Lagendijk JJ 2009 Simultaneous multimodality ROI delineation in clinical practice. *Comput. Methods Programs Biomed.* 96(2):133-40.

Borgefors G 1988 Hierarchical chamfer matching: a parametric edge matching algorithm. *IEEE Trans. Pattern Anal. Machine Intell.* 10:849-65.

Bortfeld T 2006 IMRT: a review and preview. *Phys. Med. Biol.* 51(13):363-79.

Bosarge CL, Ewing MM, DesRosiers CM and Buchsbaum JC 2016 A dosimetric comparison of whole-lung treatment techniques in the pediatric population. *Medical Dosimetry* 41(2):126-30.

Breslow NE, Lange JM, Friedman DL, Green DM, Hawkins MM, Murphy MF, Neglia JP, Olsen JH, Peterson SM, Stiller CA and Robison LL 2010 Secondary malignant neoplasms after Wilms' tumor: an international collaborative study. *Int. J. Cancer* 127(3):657-66.

Brok J, Treger TD, Gooskens SL, van den Heuvel-Eibrink MM and Pritchard-Jones K 2016 Biology and treatment of renal tumours in childhood. *Eur. J. Cancer* 68:179-95.

Brown RW, Norman Cheng YC, Haacke EM, Thompson MR and Venkatesan R 2014 Magnetic Resonance Imaging: Physical Principles and Sequence Design. Wiley (2nd Ed).

Chang JY, Li H, Zhu XR, Liao Z, Zhao L, Liu A, Li Y, Sahoo N, Poenisch F, Gomez DR, Wu R, Gillin M and Zhang X 2014 Clinical implementation of intensity modulated proton therapy for thoracic malignancies. *Int. J. Radiat. Oncol. Biol. Phys.* 90(4):809-18.

Chen S, Qin A, Zhou D and Yan D 2018 U-net-generated synthetic CT images for magnetic resonance imaging-only prostate intensity-modulated radiation therapy treatment planning. *Med. Phys.* 45(12):5659-65.

Chernak ES, Rodriguez-Antunez A, Jelden GL, Dhaliwal RS and Lavik PS 1975 The use of computed tomography for radiation therapy treatment planning. *Radiology* 117(3 Pt 1):613-4.

Coles CE, Hoole ACF, Harden SV, Burnet NG, Twyman N, Taylor RE, Kortmann RD and Williams MV 2003 Quantitative assessment of inter-clinician variability of target volume delineation for medulloblastoma: quality assurance for the SIOP PNET 4 trial protocol. *Radiother. Oncol.* 69:189-94.

D' Souza WD and Rosen II 2003 Nontumor integral dose variation in conventional radiotherapy treatment planning. *Med. Phys.* 30(8):2065-71.

de Kraker J, Graf N, Pritchard-Jones K and Pein F 2001 Nephroblastoma clinical trial and study SIOP 2001, Protocol. SIOP RTSG.

de Kraker J, Graf N, van Tinteren H, Pein F, Sandstedt B, Godzinski J, Tournade MF and SIOP 2004 Reduction of postoperative chemotherapy in children with stage I intermediate-risk and anaplastic Wilms' tumour (SIOP 93-01 trial): a randomised controlled trial. *Lancet* 364(9441):1229-35.

de Senneville BD, Zachiu C, Ries M and Moonen CTW 2016 EVolution: an edge-based variational method for non-rigid multi-modal image registration. *Phys. Med. Biol.* 61(20):7377-96.

Deurloo KE, Steenbakkers RJ, Zijp LJ, de Bois JA, Nowak PJ, Rasch CR and van Herk M 2005 Quantification of shape variation of prostate and seminal vesicles during external beam radiotherapy. *Int. J. Radiat. Oncol. Biol. Phys.* 61(1):228-38.

Dinkla AM, Wolterink JM, Maspero M, Savenije M, Verhoeff JJC, Seravalli E, Isgum I, Seevinck PR and van den Berg CAT 2018 MR-only brain radiotherapy: dosimetric evaluation of synthetic CTs generated by a dilated convolutional neural network. *Int. J. Radiat. Oncol. Biol. Phys.* 102(4):801-12.

Dowling JA, Lambert J, Parker J, Salvado O, Fripp J, Capp A, Wratten C, Denham JW and Greer PB 2012 An atlas-based electron density mapping method for magnetic resonance imaging (MRI)-alone treatment planning and adaptive MRI-based prostate radiation therapy. *Int. J. Radiat. Oncol. Biol. Phys.* 83(1):5-11.

Dowling JA, Sun J, Pichler P, Rivest-Hénault D, Ghose S, Richardson H, Wratten C, Martin J, Arm J, Best L, Chandra SS, Fripp J, Menk FW and Greer PB 2015 Automatic Substitute Computed Tomography Generation and Contouring for Magnetic Resonance Imaging (MRI)-Alone External Beam Radiation Therapy From Standard MRI Sequences. *Int. J. Radiat. Oncol. Biol. Phys.* 93(5):1144-53.

Edmund JM, Kjer HM, Van Leemput K, Hansen RH, Andersen JA and Andreasen D 2014 A voxel-based investigation for MRI-only radiotherapy of the brain using ultra short echo times. *Phys. Med. Biol.* 59(23):7501-19.

Edmund JM and Nyholm T 2017 A review of substitute CT generation for MRI-only radiation therapy. *Radiat. Oncol.* 12:28.

Eilertsen K, Vestad LN, Geier O and Skretting A 2008 A simulation of MRI based dose calculations on the basis of radiotherapy planning CT images. *Acta Oncol.* 47(7):1294-302.

Emami H, Dong M, Nejad-Davarani SP and Glide-Hurst C 2018 Generating Synthetic CTs from Magnetic Resonance Images using Generative Adversarial Networks. *Med. Phys. in press* doi: 10.1002/mp.13047.

Evans P and Chisholm D 2008 Anaesthesia and paediatric oncology. *Curr. Anaesth. Crit. Care* 19(2):50-8.

Fallone BG 2014 The rotating biplanar linac-magnetic resonance imaging system. *Semin. Radiat. Oncol.* 24(3):200-2.

Fischer-Valuck BW, Henke L, Green O, Kashani R, Acharya S, Bradley JD, Robinson CG, Thomas M, Zoberi I, Thorstad W, Gay H, Huang J, Roach M, Rodriguez V, Santanam L, Li H, Li H, Contreras J, Mazur T, Hallahan D, Olsen JR, Parikh P, Mutic S and Michalski J 2017 Two-and-a-half-year clinical experience with the world's first magnetic resonance image guided radiation therapy system. *Advances in Radiation Oncology* 2(3):485-93.

Flanz J and Smith A 2009 Technology for proton therapy. *Cancer J.* 15:292-7.

Fortney JT, Halperin EC, Hertz CM and Schulman SR 1999 Anesthesia for pediatric external beam radiation therapy. *Int. J. Radiat. Oncol. Biol. Phys.* 44(3):587-91.

Fotina I, Hopfgartner J, Stock M, Steininger T, Lütgendorf-Caucig C and Georg D 2012 Feasibility of CBCT-based dose calculation: Comparative analysis of HU adjustment techniques. *Radiother. Oncol.* 104(2):249-56.

Fredriksson A, Forsgren A and Hårdemark B 2011 Minimax optimization for handling range and setup uncertainties in proton therapy. *Med. Phys.* 38(3):1672-84.

Fuchs H, Moser P, Gröschl M and Georg D 2017 Magnetic field effects on particle beams and their implications for dose calculation in MR guided particle therapy. *Med. Phys.* 44(3):1149-56.

Gibbs IC, Tuamokumo N and Yock TI 2006 Role of radiation therapy in pediatric cancer. *Hematol. Oncol. Clin. North. Am.* 20:455-70.

Gibson E, Giganti F, Hu Y, Bonmati E, Bandula S, Gurusamy K, Davidson B, Pereira SP, Clarkson MJ and Barratt DC 2018 Automatic Multi-organ Segmentation on Abdominal CT with Dense V-networks. *IEEE Trans. Med. Imaging.* 37(8):1822-34.

Gillis AM, Sutton E, DeWitt KD, Matthay KK, Weinberg V, Fisch BM, Chan A, Gooding C, Daldrup-Link H, Wara WM, Farmer DL, Harrison MR and Haas-Kogan D 2007 Long-term outcome and toxicities of intraoperative radiotherapy for high-risk neuroblastoma. *Int. J. Radiat. Oncol. Biol. Phys.* 69(3):858-64.

Glitzner M, de Senneville BD, Lagendijk JJ, Raaymakers BW and Crijns SP 2015a On-line 3D motion estimation using low resolution MRI. *Phys. Med. Biol.* 60(16):301-10.

Glitzner M, Crijns SP, de Senneville BD, Lagendijk JJ and Raaymakers BW 2015b On the suitability of Elekta's Agility 160 MLC for tracked radiation delivery: closed-loop machine performance. *Phys. Med. Biol.* 60(5):2005-17.

Greer PB, Dahl K, Ebert MA, Wratten C, White M and Denham JW 2008 Comparison of prostate set-up accuracy and margins with off-line bony anatomy corrections and online implanted fiducial-based corrections. *J. Med. Imaging Radiat. Oncol.* 52(5):511-6.

Gross RE and Neuhauser EBD 1950 Treatment of mixed tumors of the kidney in childhood. *Pediatrics* 6:843-52.

Guerreiro F, Burgos N, Dunlop A, Wong K, Petkar I, Nutting C, Harrington K, Bhide S, Newbold K, Dearnaley D, deSouza NM, Morgan VA, McClelland J, Nill S, Cardoso MJ, Ourselin S, Oelfke U and Knopf AC 2017 Evaluation of a multi-atlas CT synthesis approach for MRI-only radiotherapy treatment planning. *Phys. Med.* 35:7-17.

Gustafsson C, Nordstrom F, Persson E, Brynolfsson J and Olsson LE 2017 Assessment of dosimetric impact of system specific geometric distortion in an MRI only based radiotherapy workflow for prostate. *Phys. Med. Biol.* 62(8):2976-89.

Hall EJ and Phil D 2006 Intensity-modulated radiation therapy, protons, and the risk of second cancers. *Int. J. Radiat. Oncol. Biol. Phys.* 65(1):1-7.

Han X 2017 MR-based synthetic CT generation using a deep convolutional neural network method. *Med. Phys.* 44(4):1408-19.

Hansen DC, Seco J, Sørensen TS, Petersen JB, Wildberger JE, Verhaegen F and Laundry G 2015 A simulation study on proton computed tomography (CT) stopping power accuracy using dual energy CT scans as benchmark. *Acta Oncol.* 54(9):1638-42.

Hartman J, Kontaxis C, Bol GH, Frank SJ, Lagendijk JJ, van Vulpen M and Raaymakers BW 2015 Dosimetric feasibility of intensity modulated proton therapy in a transverse magnetic field of 1.5 T. *Phys. Med. Biol.* 60(15):5955-69.

Hattangadi JA, Rombi B, Yock TI, Broussard G, Friedmann AM, Huang M, Chen YL, Lu HM, Kooy H and MacDonald SM 2011 Proton radiotherapy for high-risk pediatric neuroblastoma: Early outcomes and dose comparison. *Int. J. Radiat. Oncol. Biol. Phys.* 83(3):1015-22.

Hess CB, Thompson HM, Benedict SH, Seibert JA, Wong K, Vaughan AT and Chen AM 2016 Exposure risks among children undergoing radiation therapy: considerations in the era of image guided radiation therapy. *Int. J. Radiat. Oncol. Biol. Phys.* 94:978-92.

Hill-Kayser C, Tochner Z, Yimei L, Kurtz G, Lustig RA, James P, Balamuth N, Womer R, Mattei P, Grupp S, Mosse YP, Maris JM and Bagatell R 2019 Outcomes After Proton Therapy for Treatment of Pediatric High-Risk Neuroblastoma. *Int. J. Radiat. Oncol. Biol. Phys.* 104(2):401-8.

Hillbrand M, Georg D, Gadner H, Potter R and Dieckmann K 2008 Abdominal cancer during early childhood: A dosimetric comparison of proton beams to standard and advanced photon radiotherapy. *Radiother. Oncol.* 89(2):141-9.

Hoeben BA, Carrie C, Timmermann B, Mandeville HC, Gandola L, Dieckmann K, Albiac MR, Magelssen H, Lassen-Ramshad Y, Ondrová B, Ajithkumar T, Alapetite C, Balgobind BV, Bolle S, Cameron AL, Fajardo RD, Dietzsch S, Lecomte DD, van den Heuvel-Eibrink MM, Kortmann RD, Laprie A, Melchior P, Padovani L, Rombi B, Scarzello G, Schwarz R, Seiersen K, Seravalli E, Thorp N, Whitfield GA, Boterberg T and Janssens GO 2019 Management of vertebral radiotherapy dose in paediatric patients with cancer: consensus recommendations from the SIOPE radiotherapy working group. *Lancet* 20(3):155-66.

Hsieh J and Society of photo-optical instrumentation engineers 2015 Computed tomography: principles, design, artifacts and recent advances. SPIE Press monograph (3rd Ed).

Hsu HS, Cao Y, Huang K, Feng M and Balter JM 2013 Investigation of a method for generating synthetic CT models from MRI scans of the head and neck for radiation therapy. *Phys. Med. Biol.* 58(23):8419-35.

Huijskens SC, van Dijk IW, de Jong R, Visser J, Fajardo RD, Ronckers CM, Janssens GO, Maduro JH, Rasch CR, Alderliesten T and Bel A 2015 Quantification of renal and diaphragmatic interfractional motion in pediatric image-guided radiation therapy: a multicenter study. *Radiother. Oncol.* 117(3):425-31.

Huijskens SC, van Dijk IWEM, Visser J, Rasch CRN, Alderliesten T and Bel A 2017 Magnitude and variability of respiratory-induced diaphragm motion in children during image-guided radiotherapy. *Radiother. Oncol.* 123(2):263-9.

Huijskens SC, van Dijk IWEM, Visser J, Balgobind BV, te Lindert D, Rasch CRN, Alderliesten T and Bel A 2018 Abdominal organ position variation in children during image-guided radiotherapy. *Rad. Oncol.* 13(1):173.

Huijskens SC, van Dijk IWEM, Visser J, Balgobind BV, Rasch CRN, Alderliesten T and Bel A 2019 The effectiveness of 4DCT in children and adults: A pooled analysis. *J. Appl. Clin. Med. Phys.* 20(1):276-83.

Inoue T, Widder J, van Dijk LV, Takegawa H, Koizumi M, Takashina M, Usui K, Kurokawa C, Sugimoto S, Saito AI, Sasai K, Van't Veld AA, Langendijk JA and Korevaar EW 2016 Limited impact of setup and range uncertainties, breathing motion, and interplay effects in robustly optimized intensity modulated proton therapy for stage III non-small cell lung cancer. *Int. J. Radiat. Oncol. Biol. Phys.* 96(3):661-9.

Jaffray DA, Siewerdsen JH, Wong JW and Martinez AA 2002 Flat-panel cone-beam computed tomography for image-guided radiation therapy. *Int. J. Radiat. Oncol. Biol. Phys.* 53(5):1337-49.

Jereb B, Burgers JM, Tournade MF, Lemerle J, Bey P, Delemarre J, Habrand JL and Voúte PA 1994 Radiotherapy in the SIOP (International Society of Pediatric Oncology) nephroblastoma studies: a review. *Med. Pediatr. Oncol.* 22(4):221-7.

Johansson A, Karlsson M and Nyholm T 2011 CT substitute derived from MRI sequences with ultrashort echo time. *Med. Phys.* 38(5):2708-14.

Johnstone E, Wyatt JJ, Henry AM, Short SC, Sebag-Montefiore D, Murray L, Kelly CG, McCallum HM and Speight R 2018 Systematic review of synthetic computed tomography generation methodologies for use in magnetic resonance imaging-only radiation therapy. *Int. J. Radiat. Oncol. Biol. Phys.* 100(1):199–217.

Jonsson JH, Karlsson MG, Karlsson M and Nyholm T 2010 Treatment planning using MRI data: an analysis of the dose calculation accuracy for different treatment regions. *Radiat. Oncol.* 30(5):62.

Jonsson JH, Johansson A, Söderström K, Asklund T and Nyholm T 2013 Treatment planning of intracranial targets on MRI derived substitute CT data. *Radiother. Oncol.* 108(1):118-22.

Jonsson JH, Akhtari MM, Karlsson MG, Johansson A, Asklund T and Nyholm T 2015 Accuracy of inverse treatment planning on substitute CT images derived from MR data for brain lesions. *Radiat. Oncol.* 10:13.

Journy N, Indelicato DJ, Withrow DR, Akimoto T, Alapetite C, Araya M, Chang A, Chang JH, Chon B, Confer ME, Demizu Y, Dendale R, Doyen J, Ermoian R, Gurtner K, Hill-Kayser C, Iwata H, Kim JY, Kwok Y, Laack NN, Lee C Lim DH, Loredo L, Mangona VS, Mansur DB, Murakami M, Murayama S, Ogino T, Ondrová B, Parikh RR, Paulino AC, Perkins S, Ramakrishna NR, Richter R, Rombi B, Shibata S, Shimizu S, Timmermann B, Vern-Gross T, Wang CJ, Weber DC, Wilkinson JB, Witt Nyström P, Yock TI, Kleinerman RA and Berrington de Gonzalez A 2019 Patterns of proton therapy use in pediatric cancer management in 2016: An international survey. *Radiother. Oncol.* 132:155-61.

Kannan S, Teo BK, Solberg T and Hill-Kayser C 2017 Organ motion in pediatric high-risk neuroblastoma patients using four-dimensional computed tomography. *J. Appl. Clin. Med. Phys.* 18(1):107-14.

Keall PJ, Barton M, Crozier S and Australian MRI-Linac Program, including contributors from Ingham Institute, Illawarra Cancer Care Centre, Liverpool Hospital, Stanford University, Universities of Newcastle, Queensland, Sydney, Western Sydney, and Wollongong 2014 The Australian magnetic resonance imaging-linac program. *Semin. Radiat. Oncol.* 24(3):203-6.

Khan FM and Gibbons JP 2014 The physics of radiation therapy. Lippincott Williams & Wilkins (5th Ed).

Khoo VS and Joon DL 2006 New developments in MRI for target volume delineation in radiotherapy. *Br. J. Radiol.* 79(Spec No 1):2-15.

Kida S, Nakamoto T, Nakano M, Nawa K, Haga A, Kotoku JI, Yamashita H and Nakagawa K 2018 Cone tomography image quality improvement using a deep convolutional neural network. *Cureus* 10(4):2548.

Koivula L J, Wee L and Korhonen J 2016 Feasibility of MRI-only treatment planning for proton therapy in brain and prostate cancers: dose calculation accuracy in substitute CT images. *Med. Phys.* 43(8):4634.

Koivula LJ, Kapanen M, Seppälä T, Collan J, Dowling JA, Greer PB, Gustafsson C, Gunnlaugsson A, Olsson LE, Wee L and Korhonen J 2017 Intensity-based dual model method for generation of synthetic CT images from standard T2-weighted MR images generalized technique for four different MR scanners. *Radiother. Oncol.* 125(3):411-9.

Kontaxis C, Bol GH, Lagendijk JJW and Raaymakers BW 2015a A new methodology for inter- and intrafraction plan adaptation for the MR-linac. *Phys. Med. Biol.* 60(19):7485-97.

Kontaxis C, Bol GH, Lagendijk JJW and Raaymakers BW 2015b Towards adaptive IMRT sequencing for the MR-linac. *Phys. Med. Biol.* 60(6):2493-509.

Kontaxis C, Bol GH, Kerkmeijer LGW, Lagendijk JJW and Raaymakers BW 2017a Fast online replanning for interfraction rotation correction in prostate radiotherapy. *Med. Phys.* 44(10):5034-42.

Kontaxis C, Bol GH, Stemkens B, Glitzner M, Prins FM, Kerkmeijer LGW, Lagendijk JJW and Raaymakers BW 2017b Towards fast online intrafraction replanning for free-breathing stereotactic body radiation therapy with the MR-linac. *Phys. Med. Biol.* 62(18):7233-48.

Kontaxis C, Bol GH, Lagendijk JJW and Raaymakers BW 2018 Towards online adaptive VMAT sequencing for multi-fraction radiotherapy on the MRI-linac. *Med. Phys.* 45(6):663.

Korevaar EW, van Dijk LV, Kierkels RG, Sijtsema NM, Bijl HP, Langendijk JA and van't Veld AA 2016 Evaluation of robustness of target coverage: transition from the PTV concept to multi-scenario CTV evaluation. *Proceedings of the 55th Annual Meeting for the Particle Therapy Cooperative Group* (PTCOG).

Korhonen J, Kapanen M, Keyrilainen J, Seppala T and Tenhunen M 2014 A dual model HU conversion from MRI intensity values within and outside of bone segment for MRI-based radiotherapy treatment planning of prostate cancer. *Med. Phys.* 41(1):011704.

Korsholm ME, Waring LW and Edmund JM 2014 A criterion for the reliable use of MRI-only radiotherapy. *Radiat Oncol.* 9:16.

Kraan AC, van de Water S, Teguh DN, Al-Mamgani A, Madden T, Kooy HM, Heijmen BJ and Hoogeman MS 2013 Dose uncertainties in IMPT for oropharyngeal cancer in the presence of anatomical, range, and setup errors. *Int. J. Radiat. Oncol. Biol. Phys.* 87(5):888-96.

Kristensen I, Nilsson K and Nilsson P 2015 Comparative proton and photon treatment planning in pediatric patients with various diagnoses. *Int. J. Particle Ther.* 2(2):367-75.

Kurz C, Dedes G, Resch A, Reiner M, Ganswindt U, Nijhuis R, Thieke C, Belka C, Parodi K and Landry G 2015 Comparing cone-beam CT intensity correction methods for dose recalculation in adaptive intensity-modulated photon and proton therapy for head and neck cancer. *Acta Oncol.* 54(9):1651-7.

Kurz C, Kamp F, Park YK, Zollner C, Rit S, Hansen D, Podesta M7, Sharp GC, Li M, Reiner M, Hofmaier J, Neppl S, Thieke C, Nijhuis R, Ganswindt U, Belka C, Winey BA, Parodi K and Landry G 2016 Investigating deformable image registration and scatter correction for CBCT-based dose calculation in adaptive IMPT. *Med. Phys.* 43(10):5635-46.

Kurz C, Hansen DC, Savenije MH, Landry G, Maspero M, Kamp F, Parodi K, Belka C and van den Berg C 2018 Cone-beam CT intensity correction for adaptive radiotherapy of the prostate using deep learning. *Phys. Med.* 52(1):48.

Ladenstein R, Pötschger U, Pearson ADJ, Brock P, Luksch R, Castel V, Yaniv I, Papadakis V, Laureys G, Malis J, Balwierz W, Ruud E, Kogner P, Schroeder H, de Lacerda AF, Beck-Popovic M, Bician P, Garami M, Trahair T, Canete A, Ambros PF, Holmes K, Gaze M, Schreier G, Garaventa A, Vassal G, Michon J, Valteau-Couanet D and SIOP Europe Neuroblastoma Group (SIOPEN) 2017 Busulfan and melphalan versus carboplatin, etoposide, and melphalan as high-dose chemotherapy for high-risk neuroblastoma (HR-NBL1/SIOPEN): an international, randomised, multi-arm, open-label, phase 3 trial. *Lancet* 18(4):500-14.

Lagendijk JJW and Bakker CJG 2000 MRI guided radiotherapy: a MRI based linear accelerator. *Radiother. Oncol.* 1:1-255.

Lagendijk JJ, Raaymakers BW, Raaijmakers AJ, Overweg J, Brown KJ, Kerkhof EM, van der Put RW, Hårdemark B, van Vulpen M and van der Heide UA 2008 MRI/linac integration. *Radiother. Oncol.* 86(1):25-9.

Lagendijk JJW, Raaymakers BW, Van den Berg CAT, Moerland MA, Philippens ME and van Vulpen M 2014 MR guidance in radiotherapy. *Phys. Med. Biol.* 59(21):349-69.

Lagendijk JJ, van Vulpen M and Raaymakers BW 2016 The development of the MRI linac system for online MRI-guided radiotherapy: a clinical update. *J. Intern. Med.* 280(2):203-8.

Langendijk JA, Lambin P, De Ruysscher D, Widder J, Bos M and Verheij M 2013 Selection of patients for radiotherapy with protons aiming at reduction of side effects: the model-based approach. *Radiother. Oncol.* 107(3):267-73.

Lavdas I, Glocker B, Kamnitsas K, Rueckert D, Mair H, Sandhu A, Taylor SA, Aboagye EO and Rockall AG 2017 Fully automatic, multiorgan segmentation in normal whole body magnetic resonance imaging (MRI), using classification forests (CFs), convolutional neural networks (CNNs), and a multi-atlas (MA) approach. *Med. Phys.* 44(10):5210-20.

Lee YK, Bollet M, Charles-Edwards G, Flower MA, Leach MO, McNair H, Moore E, Rowbottom C and Webb S 2003 Radiotherapy treatment planning of prostate cancer using magnetic resonance imaging alone. *Radiother. Oncol.* 66(2):203-16.

Leeman JE, Romesser PB, Zhou Y, McBride S, Riaz N, Sherman E, Cohen MA, Cahlon O and Lee N 2017 Proton therapy for head and neck cancer: expanding the therapeutic window. *Lancet* 18(5):254-65.

Liang X, Chen L, Nguyen D, Zhou Z, Gu X, Yang M, Wang J and Jiang S 2018 Generating synthesized computed tomography (CT) from cone-beam computed tomography (CBCT) using CycleGAN for adaptive radiation therapy. *Phys. Med. Biol.* 64(12):125002.

Lin L, Kang M, Huang S, Mayer R, Thomas A, Solberg TD, McDonough JE and Simone CB 2015 Beam-specific planning target volumes incorporating 4D CT for pencil beam scanning proton therapy of thoracic tumors. *J. Appl. Clin. Med. Phys.* 16(6):281-92.

Liu W, Zhang X, Li Y and Mohan R 2012 Robust optimization of intensity modulated proton therapy. *Med. Phys.* 39(2):179-91.

Liu W, Frank SJ, Li X, Zhu RX and Mohan R 2013 PTV-based IMPT optimization incorporating planning risk volumes vs robust optimization. *Med. Phys.* 40(2):021709.

Liu W, Liao Z, Schild SE, Liu Z, Li H, Li Y, Park PC, Li X, Stoker J, Shen J, Keole S, Anand A, Fatyga M, Dong L, Sahoo N, Vora S, Wong W, Zhu XR, Bues M and Mohan R 2015 Impact of respiratory motion on worst-case scenario optimized intensity-modulated proton therapy for lung cancers. *Pract. Radiat. Oncol.* 5(2):77-86.

Liu W, Schild SE, Chang JY, Liao Z, Chang YH, Wen Z, Shen J, Stoker JB, Ding X, Hu Y, Sahoo N, Herman MG, Vargas C, Keole S, Wong W and Bues M 2016 Exploratory study of 4D versus 3D robust optimization in intensity modulated proton therapy for lung cancer. *Int. J. Radiat. Oncol. Biol. Phys.* 95(1):523-33.

Lomax AJ 1999 Intensity modulation methods for proton radiotherapy. *Phys. Med. Biol.* 44(1):185-205.

Lomax AJ, Boehringer T, Coray A, Egger E, Goitein G, Grossmann M, Juelke P, Lin S, Pedroni E, Rohrer B, Roser W, Rossi B, Siegenthaler B, Stadelmann O, Stauble H, Vetter C and Wisser L 2001 Intensity modulated proton therapy: A clinical example. *Med. Phys.* 28(3):317-24.

Lomax AJ, Bohringer T, Bolsi A, Coray D, Emert F, Gotein G, Jermann M, Lin S, Pedroni E, Rutz H, Stadelmann O, Timmermann B, Verwey J and Weber DC 2004 Treatment planning and verification of proton therapy using spot scanning: initial experiences. *Med. Phys.* 31(11):3150-7.

Lomax AJ 2008a Intensity modulated proton therapy and its sensitivity to treatment uncertainties 1: the potential effects of calculational uncertainties. *Phys. Med. Biol.* 53(4):1027-42.

Lomax AJ 2008b Intensity modulated proton therapy and its sensitivity to treatment uncertainties 2: the potential effects of inter-fraction and inter-field motions. *Phys. Med. Biol.* 53(4):1043-56.

Lomax AJ 2009 Charged Particle Therapy: The Physics of Interaction. *Cancer J.* 15(4):285-91.

Lomax A 2016 SFUD, IMPT, and plan robustness. In: Rath A., Sahoo N. (eds) Particle Radiotherapy. Springer, p.169-94.

Malyapa R, Lowe M, Bolsi A, Lomax AJ, Weber DC and Albertini F 2016 Evaluation of robustness to setup and range uncertainties for head and neck patients treated with pencil beam scanning proton therapy. *Int. J. Radiat. Oncol. Biol. Phys.* 95(1):154-62.

Maris JM, Hogarty MD, Bagatell R and Cohn SL 2007 Neuroblastoma. *Lancet* 369(9579):2106-20.

Maspero M, Seevinck PR, Schubert G, Hoesl MA, van Asselen B, Viergever MA, Lagendijk JJ, Meijer GJ and van den Berg CA 2017a Quantification of confounding factors in MRI-based dose calculations as applied to prostate IMRT. *Phys. Med. Biol.* 62(3):948-65.

Maspero M, van den Berg CAT, Landry G, Belka C, Parodi K, Seevinck PR, Raaymakers BW and Kurz C 2017b Feasibility of MR-only proton dose calculations for prostate cancer radiotherapy using a commercial pseudo-CT generation method. *Phys. Med. Biol.* 62(24):9159-76.

Maspero M, Savenije MHF, Dinkla AM, Seevinck P, Intven MPW, Jurgenliemk-Schulz IM, Kerkmeijer LGW and van den Berg CAT 2018 Dose evaluation of fast synthetic-CT generation using a generative adversarial network for general pelvis MR-only radiotherapy. *Phys. Med. Biol.* 63(18):185001.

McGowan SE, Albertini F, Thomas SJ and Lomax AJ 2015 Defining robustness protocols: a method to include and evaluate robustness in clinical plans. *Phys. Med. Biol.* 60(7):2671-84.

McKenzie A, van Herk M and Mijnheer B 2002 Margins for geometric uncertainty around organs at risk in radiotherapy. *Radiother. Oncol.* 62(3):299-307.

Meyer P, Noblet V, Mazzara C and Lallement A 2018 Survey on deep learning for radiotherapy. *Comput. Biol. Med.* 98:126-46.

Mohan R and Grosshans D 2017 Proton therapy: present and future. *Adv. Drug. Deliv. Rev.* 109:26-44.

Moteabbed M, Schuemann J and Paganetti H 2014 Dosimetric feasibility of real-time MRI-guided proton therapy. *Med. Phys.* 41(11):111713.

Moyers MF, Sardesai M, Sun S and Miller DW 2009 Ion stopping powers and CT numbers. *Med. Dosim.* 35(3):179-94.

Mutic S and Dempsey JF 2014 The ViewRay system: magnetic resonance guided and controlled radiotherapy. *Semin. Radiat. Oncol.* 24(3):196-9.

Nazmy M, Khafaga Y, Mousa A and Khalil E 2012 Cone beam CT for organs motion evaluation in pediatric abdominal neuroblastoma. *Radiother. Oncol.* 102(3):388-92.

Nederveen A, Lagendijk J and Hofman P 2000 Detection of fiducial gold markers for automatic on-line megavoltage position verification using a marker extraction kernel (MEK). *Int. J. Radiat. Oncol. Biol. Phys.* 47(5):1435-42.

Newhauser WD and Zhang R 2015 The physics of proton therapy. *Phys. Med. Biol.* 60(8):155-209.

Nickoloff JA 2015 Photon, light ion, and heavy ion cancer radiotherapy: paths from physics and biology to clinical practice. *Ann. Transl. Med.* 3(21):336.

Nyholm T, Nyberg M, Karlsson MG and Karlsson M 2009 Systematisation of spatial uncertainties for comparison between a MR and a CT-based radiotherapy workflow for prostate treatments. *Radiat. Oncol.* 4:54.

Nyholm T and Jonsson J 2014 Counterpoint: Opportunities and challenges of a magnetic resonance imaging-only radiotherapy work flow. *Semin. Radiat. Oncol.* 24(3):175-80.

Oborn BM, Dowdell S, Metcalfe PE, Crozier S, Mohan R and Keall PJ 2015 Proton beam deflection in MRI fields: Implications for MRI-guided proton therapy. *Med. Phys.* 42(5):2113-24.

Oborn BM, Dowdell S, Metcalfe PE, Crozier S, Mohan R and Keall PJ 2017 Future of medical physics: Real-time MRI-guided proton therapy. *Med. Phys.* 44(8):77-90.

Oeffinger KC, Mertens AC, Sklar CA, Kawashima TA, Hudson MM, Meadows AT, Friedman DL, Marina N, Hobbie W, Kadan-Lottick NS, Schwartz CL, Leisenring W and Robison LL 2006 Chronic Health Conditions in Adult Survivors of Childhood Cancer. *N. Engl. J. Med.* 355(15):1572-82.

O'Leary M, Krailo M, Anderson JR and Reaman GH 2008 Progress in childhood cancer: 50 years of research collaboration, a report from the children's oncology group. *Semin. Oncol.* 35(5):484-93.

Otto K 2008 Volumetric modulated arc therapy: IMRT in a single gantry arc. *Med. Phys.* 35(1):310-7.

Padovani L, Huchet A, Claude L, Bernier V, Quetin P, Mahe M, Laprie A, Kerr C, Bondiau PY, Delarue A, Coze C, Gibon D, Barteau C, Maire JP, Carrie C and Muracciole X 2009 Inter-clinician variability in making decisions in pediatric treatment: A balance between efficacy and late effects. *Radiother. Oncol.* 93:372–6.

Paganetti H 2012 Proton Therapy Physics. Series in Medical Physics and Biomedical Engineering. CRC Press.

Paganetti H 2014 Relative biological effectiveness (RBE) values for proton beam therapy. Variations as a function of biological endpoint, dose, and linear energy transfer. *Phys. Med. Biol.* 59(22):419-72.

Pai Panandiker AS, Sharma S, Naik MH, Wu S, Hua C, Beltran B, Krasin MJ and Merchant TE 2012 Novel assessment of renal motion in children as measured via four-dimensional computed tomography. *Int. J. Radiat. Oncol. Biol. Phys.* 82(5):1771-6.

Paradis E, Cao Y, Lawrence TS, Tsien C, Feng M, Vineberg K and Balter JM 2015 Assessing the dosimetric accuracy of magnetic resonance-generated synthetic CT images for focal brain VMAT radiation therapy. *Int. J. Radiat. Oncol. Biol. Phys.* 93(5):1154-61.

Park S, Cho M and Kim H 2009 On-board CBCT/CBDT for Image-guided Proton Therapy: Initial Performance Evaluation. *Int. J. Radiat. Oncol. Biol. Phys.* 75(3):595-6.

Park PC, Cheung JP, Zhu XR, Lee AK, Sahoo N, Tucker SL, Liu W, Li H, Mohan R, Court LE and Dong L 2013 Statistical assessment of proton treatment plans under setup and range uncertainties. *Int. J. Radiat. Oncol. Biol. Phys.* 86(5):1007-13.

Pastore G, Znaor A, Spreafico F, Graf N, Pritchard-Jones K and Steliarova-Foucher E 2006 Malignant renal tumours incidence and survival in European children (1978–1997): report from the Automated Childhood Cancer Information System project. *Eur. J. Cancer* 42(13):2103-14.

Persson E, Gustafsson C, Nordström F, Sohlin M, Gunnlaugsson A, Petruson K, Rintelä N, Hed K, Blomqvist L, Zackrisson B, Nyholm T, Olsson LE, Siversson C and Jonsson J 2017 MR-OPERA: A Multicenter/Multivendor Validation of Magnetic Resonance Imaging-Only Prostate Treatment Planning Using Synthetic Computed Tomography Images. *Int. J. Radiat. Oncol. Biol. Phys.* 99(3):692-700.

Pham D, Kron T, Foroudi F, Schneider M and Siva S 2014 A review of kidney motion under free, deep and forced-shallow breathing conditions: implications for stereotactic ablative body radiotherapy treatment. *Technol. Cancer Res. Treat.* 13(4):315-23.

Prior P, Chen X, Botros M, Paulson ES, Lawton C, Erickson B and Li XA 2016 MRI-based IMRT planning for MR-linac: comparison between CT- and MRI-based plans for pancreatic and prostate cancers. *Phys. Med. Biol.* 61(10):3819-42.

Pritchard-Jones K, Bergeron C, de Camargo B, van den Heuvel-Eibrink MM, Acha T, Godzinski J, Oldenburger F, Boccon-Gibod L, Leuschner I, Vujanic G, Sandstedt B, de Kraker J, van Tinteren H, Graf N and SIOP Renal Tumours Study Group 2015 Omission of doxorubicin from the treatment of stage II–III, intermediate-risk Wilms' tumour (SIOP WT 2011): an open-label, non-inferiority, randomised controlled trial. *Lancet* 386(9999):1156-64.

Podgorsak EB 2005 Radiation Oncology Physics: A Handbook for Teachers and Students. International Atomic Energy Agency.

Quan EM, Liu W, Wu R, Li Y, Frank SJ, Zhang X, Zhu XR and Mohan R 2013 Preliminary evaluation of multifield and single-field optimization for the treatment planning of spot-scanning proton therapy of head and neck cancer. *Med. Phys.* 40(8):081709.

Raaijmakers AJ, Raaymakers BW and Lagendijk JJ 2005 Integrating a MRI scanner with a 6 MV radiotherapy accelerator: dose increase at tissue-air interfaces in a lateral magnetic field due to returning electrons. *Phys. Med. Biol.* 50(7):1363-76.

Raaijmakers AJ, Hårdemark B, Raaymakers BW, Raaijmakers CP and Lagendijk JJ 2007a Dose optimization for the MRI-accelerator: IMRT in the presence of a magnetic field. *Phys. Med. Biol.* 52(23):7045-54.

Raaijmakers AJ, Raaymakers BW, van der Meer S and Lagendijk JJ 2007b Integrating a MRI scanner with a 6 MV radiotherapy accelerator: impact of the surface orientation on the entrance and exit dose due to the transverse magnetic field. *Phys. Med. Biol.* 52(4):929-39.

Raaymakers BW, Raaijmakers AJ and Lagendijk JJ 2008 Feasibility of MRI guided proton therapy: magnetic field dose effects. *Phys. Med. Biol.* 53(20):5615-22.

Raaymakers BW, Lagendijk JJ, Overweg J, Kok JG, Raaijmakers AJ, Kerkhof EM, van der Put RW, Meijsing I, Crijns SP, Benedosso F, van Vulpen M, de Graaff CH, Allen J and Brown KJ 2009 Integrating a 1.5 T MRI scanner with a 6 MV accelerator: proof of concept. *Phys. Med. Biol.* 54(12):229-37.

Raaymakers BW, Jurgenliemk-Schulz IM, Bol GH, Glitzner M, Kotte ANTJ, van Asselen B, de Boer JCJ, Bluemink JJ, Hackett SL, Moerland MA, Woodings SJ, Wolthaus JWH, van Zijp HM, Philippens MEP, Tijssen R, Kok JGM, de Groot-van Breugel EN, Kiekebosch I, Meijers LTC, Nomden CN, Sikkes GG, Doornaert PAH, Eppinga WSC, Kasperts N, Kerkmeijer LGW, Tersteeg JHA, Brown KJ, Pais B, Woodhead P and Lagendijk JJW 2017 First patients treated with a 1.5T MRI-Linac: clinical proof of concept of a high-precision, high-field MRI guided radiotherapy treatment. *Phys. Med. Biol.* 62(23):41-50.

Rai R, Kumar S, Batumalai V, Elwadia D, Ohanessian L, Juresic E, Cassapi L, Vinod SK, Holloway L, Keall PJ and Liney GP 2017 The integration of MRI in radiation therapy: collaboration of radiographers and radiation therapists. *J. Med. Radiat. Sci.* 64(1):61-8.

Rasch C, Steenbakkers R and van Herk M 2005 Target Definition in Prostate, Head, and Neck. *Semin. Radiat. Oncol.* 15:136-45.

Rate WR, Butler MS, Robertson WW and D'Angio GJ 1991 Late orthopedic effects in children with Wilms' tumor treated with abdominal irradiation. *Med. Pediatr. Oncol.* 19(4):265-8.

Ribeiro CO, Meijers A, Korevaar EW, Muijs CT, Both S, Langendijk JA and Knopf A 2019 Comprehensive 4D robustness evaluation for pencil beam scanned proton plans. *Radiother. Oncol.* 136:185-9.

Ritchey ML, Green DM, Thomas PRM, Smith GR, Haase G, Shochat S, Moksness J and Breslow NE 1996 Renal failure in Wilms' tumor patients: a report from the National Wilms' Tumor Study Group. *Med. Pediatr. Oncol.* 26(2):75-80.

Robinson LL and Hudson MM 2014 Survivors of childhood and adolescent cancer: life-long risks and responsibilities. *Nat. Rev. Cancer* 14(1):61-70.

Sasso G, Greco N, Murino P and Sasso FS 2010 Late toxicity in Wilms tumor patients treated with radiotherapy at 15 years of median follow-up. *J. Pediatr. Hematol. Oncol.* 32(7):264-7.

Schaffer R, Vollans E, Vellani R, Welsh M, Moiseenko V and Goddard K 2011 A Radiotherapy Planning Study of RapidArc, Intensity Modulated Radiotherapy, Three-Dimensional Conformal Radiotherapy, and Parallel Opposed Beams in the Treatment of Pediatric Retroperitoneal Tumors. *Pediatric Blood & Cancer* 56(1):16-23.

Schellhammer SM and Hoffmann AL 2017 Prediction and compensation of magnetic beam deflection in MR-integrated proton therapy: a method optimized regarding accuracy, versatility and speed. *Phys. Med. Biol.* 62(4):1548-64.

Schellhammer SM, Gantz S, Lühr A, Oborn BM, Bussmann M and Hoffmann AL 2018a Technical Note: Experimental verification of magnetic field-induced beam deflection and Bragg peak displacement for MR-integrated proton therapy. *Med. Phys.* 45(7):3429-34.

Schellhammer SM, Hoffmann AL, Gantz S, Smeets J, van der Kraaij E, Quets S, Pieck S, Karsch L and Pawelke J 2018b Integrating a low-field open MR scanner with a static proton research beam line: proof of concept. *Phys. Med. Biol.* 63(23):23LT01.

Schillo M, Geisler A, Hobl A, Klein HU, Krischel D, Meyer-Reumers M, Piel C, Blosser H, Kim JW, Marti F, Vincent J, Brandenburg S and Beijers JPM 2001 Compact superconducting 250 MeV proton cyclotron for the PSI PROSCAN proton therapy project. *AIP Conference Proceedings* 600:37-9.

Schneider U, Pedroni E and Lomax A 1996 The calibration of CT Hounsfield units for radiotherapy treatment planning. *Phys. Med. Biol.* 41:111-24.

Schneider U and Hälg R 2015 The Impact of Neutrons in Clinical Proton Therapy. *Front. Oncol.* 5:235.

Sharp G, Fritscher KD, Pekar V, Peroni M, Shusharina N, Veeraraghavan H and Yang J 2014 Vision 20/20: perspectives on automated image segmentation for radiotherapy. *Med. Phys.* 41(5):050902.

Siversson C, Nordström F, Nilsson T, Nyholm T, Jonsson J, Gunnlaugsson A and Olsson LE 2015 Technical Note: MRI only prostate radiotherapy planning using the statistical decomposition algorithm. *Med. Phys.* 42(10):6090-7.

Sjolund J, Forsberg D, Andersson M and Knutsson H 2015 Generating patient specific pseudo-CT of the head from MR using atlas-based regression. *Phys. Med. Biol.* 60:825-39.

SKION 2015 DCOG NBL 2009 Treatment Protocol for Risk Adapted Treatment of Children with Neurblastoma.

Smith A, Gillin M, Bues M, Zhu XR, Suzuki K, Mohan R, Woo S, Lee A, Komaki R, Cox J, Hiramoto K, Akiyama H, Ishida T, Sasaki T and Matsuda K 2009 The M. D. Anderson proton therapy system. *Med. Phys.* 36(9):4068-83.

Spector LG, Pankratz N and Marcotte EL 2015 Genetic and nongenetic risk factors for childhood cancer. *Cancer Pediatr. Clin. North Am.* 62(1):11-25.

Stanescu T, Jans H S, Pervez N, Stavrev P and Fallone BG 2008 A study on the magnetic resonance imaging (MRI)-based radiation treatment planning of intracranial lesions. *Phys. Med. Biol.* 53(13):3579-93.

Steliarova-Foucher E, Colombet M, Ries LAG, Moreno F, Dolya A, Bray F, Hessing P, Shin HY, Stiller CA and IICC-3 contributors 2017 International incidence of childhood cancer, 2001-10: a population-based registry study. *Lancet* 18(6):719-31.

Stemkens B, Tijssen RH, de Senneville BD, Heerkens HD, van Vulpen M, Lagendijk JJ and van den Berg CA 2015 Optimizing 4-dimensional magnetic resonance imaging data sampling for respiratory motion analysis of pancreatic tumors. *Int. J. Radiat. Oncol. Biol. Phys.* 91(3):571-8.

Stemkens B, Tijssen RH, de Senneville BD, Lagendijk JJ and van den Berg CA 2016 Image-driven, model-based 3D abdominal motion estimation for MR-guided radiotherapy. *Phys. Med. Biol.* 61(14):5335-55.

Stock M, Pasler M, Birkfellner W, Homolka P, Poetter R and Georg D 2009 Image quality and stability of image-guided radiotherapy (IGRT) devices: A comparative study. *Radiother. Oncol.* 93(1):1-7.

Stuschke M, Kaiser A, Pöttgen C, Lubcke W and Farr J 2012 Potentials of robust intensity modulated scanning proton plans for locally advanced lung cancer in comparison to intensity modulated photon plans. *Radiother. Oncol.* 104(1):45-51.

Stuschke M, Kaiser A, Abu-Jawad J, Pöttgen C, Levegrün S and Farr J 2013 Multi-scenario based robust intensity-modulated proton therapy (IMPT) plans can account for set-up errors more effectively in terms of normal tissue sparing than planning target volume (PTV) based intensity-modulated photon plans in the head and neck region. *Radiat. Oncol.* 8(1):145.

Taasti VT, Bäumer C, Dahlgren CV, Deisher AJ, Ellerbrock M, Free J, Gora J, Kozera A, Lomax AJ, De Marzi L, Molinelli S, Teo BKK, Wohlfahrt P, Petersen JBB, Muren LP, Hansen DC and Richter C 2018 Inter-centre variability of CT-based stopping-power prediction in particle therapy: Survey-based evaluation. *Physics and Imaging in Radiation Oncology* 6:25-30.

Taylor AJ, Winter DL, Pritchard-Jones K, Stiller CA, Frobisher C, Lancashire ER, Reulen RC, Hawkins MM and British Childhood Cancer Survivor Study 2008 Second primary neoplasms in survivors of Wilms' tumour – a population-based cohort study from the British Childhood Cancer Survivor Study. *Int. J. Cancer* 122(9):2085-93.

Taylor PA, Kry SF and Followill DS 2017 Pencil Beam Algorithms Are Unsuitable for Proton Dose Calculations in Lung. *Int. J. Radiat. Oncol.* 99(3):750-6.

Tenhunen M, Korhonen J, Kapanen M, Seppala T, Koivula L, Collan J, Saarilahti K and Visapaa H 2018 MRI-only based radiation therapy of prostate cancer: workflow and early clinical experience. *Acta Oncol.* 57(7):902-7.

Thwaites DI and Tuohy JB 2006 Back to the future: the story and development of the clinical linear accelerator. *Phys. Med. Biol.* 51(13):343-62.

Tijssen RHN, Crijns SPM, Bluemink SS, Hacket SS, de Vries JHW, Kruiskamp MJ, Philippens MEP, Lagendijk JJW and Raaymakers BW 2017 Comprehensive MRI acceptance testing & commissioning of a 1.5T MR-linac: guidelines and initial results. *Radiother. Oncol.* 123:130-1.

Trofimov A and Bortfeld T 2003 Optimization of Beam Parameters and Treatment Planning for Intensity Modulated Proton Therapy. *Technology in Cancer Research & Treatment* 2(5):437-44.

Tustison NJ, Avants BB, Cook PA, Zheng Y, Egan A, Yushkevich PA and Gee JC 2010 N4ITK: improved N3 bias correction. *IEEE Trans. Med. Imaging* 29:1310-20.

Tyler DJ, Robson MD, Henkelman RM, Young IR and Bydder GM 2007 Magnetic Resonance Imaging with Ultrashort TE (UTE) PULSE sequences: Technical considerations. *J. Magn. Reson. Imaging* 25(2):279-89.

Uh J, Merchant TE, Li Y, Li X and Hua C 2014 MRI-based treatment planning with pseudo CT generated through atlas registration. *Med. Phys.* 41(5):051711.

Uh J, Krasin MJ, Li Y, Li X, Tinkle C, Lucas JT, Merchant TE and Hua C 2017 Quantification of pediatric abdominal organ motion with 4-dimensional magnetic resonance imaging method. *Int. J. Radiat. Oncol. Biol. Phys.* 99(1):227-37.

Unkelbach J, Chan TCY and Bortfeld T 2007 Accounting for range uncertainties in the optimization of intensity modulated proton therapy. *Phys. Med. Biol.* 52(10):2755-73.

Unkelbach J and Paganetti H 2018 Robust Proton Treatment Planning: Physical and Biological Optimization. *Semin. Radiat. Oncol.* 28(2):88-96.

van den Heuvel-Eibrink MM, Hol JA, Pritchard-Jones K, van Tinteren H, Furtwängler R, Verschuur AC, Vujanic GM, Leuschner I, Brok J, Rübe C, Smets AM, Janssens GO, Godzinski J, Ramírez-Villar GL, de Camargo B, Segers H, Collini P, Gessler M, Bergeron C, Spreafico F, Graf N and International Society of Paediatric Oncology Renal Tumour Study Group (SIOP–RTSG) 2017 Position paper: rationale for the treatment of Wilms tumour in the UMBRELLA SIOP-RTSG 2016 protocol. *Nat. Rev. Urol.* 14(12):743-52.

van der Heide UA, Kotte AN, Dehnad H, Hofman P, Lagenijk JJ and van Vulpen M 2007 Analysis of fiducial marker-based position verification in the external beam radiotherapy of patients with prostate cancer. *Radiother. Oncol.* 82(1):38-45.

van der Horst A, Wognum D, Dávila Fajardo R, de Jong R, van Hooft JE, Fockens P, van Tienhoven G and Bel A 2013 Interfractional position variation of pancreatic tumors quantified using intratumoral fiducial markers and daily cone beam computed tomography. *Int. J. Radiat. Oncol. Biol. Phys.* 87(1):202-8.

van Dijk IWEM, Huijskens SC, de Jong R, Visser J, Fajardo RD, Rasch CRN, Alderliesten T and Bel A 2017 Interfractional renal and diaphragmatic position variation during radiotherapy in children and adults: is there a difference? *Acta Oncol.* 56(8):1065-71.

van Herk M, Remeijer P, Rasch C and Lebesque JV 2000 The probability of correct target dosage: dose-population histograms for deriving treatment margins in radiotherapy. *Int. J. Radiat. Oncol. Biol. Phys.* 47(4):1121-35.

van Herk M, Witte M, van der Geer J, Schneider C and Lebesque JV 2003 Biologic and physical fractionation effects of random geometric errors. *Int. J. Radiat. Oncol. Biol. Phys.* 57(5):1460-71.

van Herk M 2004 Errors and margins in radiotherapy. *Semin. Radiat. Oncol.* 14(1):52-64.

van Mourik AM, Elkhuizen PH, Minkema D, Duppen JC, Dutch Young Boost Study Group and van Vliet-Vroegindeweij C 2010 Multiinstitutional study on target volume delineation variation in breast radiotherapy in the presence of guidelines. *Radiother. Oncol.* 94(3):286-91.

van Waas M, Neggers S, Raat H, van Rij CM, Pieters R and van den Heuvel-Eibrink MM 2012 Abdominal Radiotherapy: a major determinant of metabolic syndrome in nephroblastoma and neuroblastoma survivors. *PLoS One* 7(12):e52237.

Veiga C, McClelland J, Moinuddin S, Loureno A, Ricketts K, Annkah J, Modat M, Ourselin S, D'Souza D and Royle G 2014 Towards adaptive radiotherapy for head and neck patients: feasibility study on using CT-to-CBCT deformable registration for 'dose of the day' calculations. *Med. Phys.* 41(3):031703.

Veiga C, Lourenço AM, Mouinuddin S, van Herk M, Modat M, Ourselin S, Royle G and McClelland JR 2015 Toward adaptive radiotherapy for head and neck patients: uncertainties in dose warping due to the choice of deformable registration algorithm. *Med. Phys.* 42(2):760-9.

Versteijne E, Gurney-Champion OJ, van der Horst A, Lens E, Kolff MW, Buijsen J, Ebrahimi G, Neelis KJ, Rasch CRN, Stoker J, van Herk M, Bel A and van Tienhoven G 2017 Considerable interobserver variation in delineation of pancreatic cancer on 3DCT and 4DCT: a multi-institutional study. *Radiat. Oncol.* 12:58.

Vinod SK, Jameson MG, Min M and Holloway LC 2016 Uncertainties in volume delineation in radiation oncology: A systematic review and recommendations for future studies. *Radiother. Oncol.* 121(2):169-79.

Vogel J, Lin H, Both S, Tochner Z, Balis F and Hill-Kayser C 2017 Pencil beam scanning proton therapy for treatment of retroperitoneum after nephrectomy for Wilms tumor: A dosimetric comparison study. *Pediatr. Blood Cancer* 64:39-45.

Wall V, Marignol L and ElBeltagi N 2018 Image-Guided Radiotherapy in Paediatrics: A Survey of International Patterns of Practice. *Journal of Medical Imaging and Radiation Sciences* 49(3):265-9.

Wang D, Strugnell W, Cowin G, Doddrell DM and Slaughter R 2004 Geometric distortion in clinical MRI systems part I: evaluation using a 3D phantom. *Magn. Reson. Imaging* 22:1211-21.

Widder J, van der Schaaf A, Lambin P, Marijnen CA, Pignol JP, Rasch CR, Slotman BJ, Verheij M and Langendijk JA 2016 The Quest for Evidence for Proton Therapy: Model-Based Approach and Precision Medicine. *Int. J. Radiat. Oncol. Biol. Phys.* 95(1):30-6.

Wilson RR 1946 Radiological use of fast protons. *Radiology* 47(5):487-91.

Wolf R and Bortfeld T 2012 An analytical solution to proton Bragg peak deflection in a magnetic field. *Phys. Med. Biol.* 57(17):329-37.

Woodings SJ, Bluemink JJ, Wilfred de Vries JH, Niatsetski Y, van Veelen B, Schillings J, Kok JGM, Wolthaus JWH, Hackett SL, van Asselen B, van Zijp HM, Pencea S, Roberts DA, Lagendijk JJW and Raaymakers BW 2018 Beam characterisation of the 1.5T MRI-linac. *Phys. Med. Biol.* 63(8):085015.

Wopereis A, Ishakoglu I, Seravalli E and Wolthaus J 2015 A cost-effective and fast end-to-end test for treatment accuracy evaluation. *Radiother. Oncol.* 119(1):910-1.

Wysocka B, Kassam Z, Lockwood G, Brierley J, Dawson LA, Buckley CA, Jaffray D, Cummings B, Kim J, Wong R and Ringash J 2010 Interfraction and respiratory organ motion during conformal radiotherapy in gastric cancer. *Int. J. Radiat. Oncol. Biol. Phys.* 77(1):53-9.

Yang M, Virshup G, Clayton J, Zhu XR, Mohan R and Dong L 2010 Theoretical variance analysis of single- and dual-energy computed tomography methods for calculating proton stopping power ratios of biological tissues. *Phys. Med. Biol.* 55:1343-62.

Zachiu C, de Senneville BD, Tijssen RHN, Kotte ANTJ, Houweling AC, Kerkmeijer LGW, Lagendijk JJW, Moonen CTW and Ries M 2017 Non-rigid CT/CBCT to CBCT registration for online external beam radiotherapy guidance. *Phys. Med. Biol.* 63(1):015027.

Zelefskya MJ, Leibel SA, Kutchera GJ and Fuk Z 1998 Three-dimensional conformal radiotherapy and dose escalation: Where do we stand? *Semin. Radiat. Oncol.* 8(2):107-14.

Zeng C, Plastaras JP, Tochner ZA, White BM, Hill-Kayser CE, Hahn SM and Both S 2015 Proton pencil beam scanning for mediastinal lymphoma: the impact of interplay between target motion and beam scanning. *Phys. Med. Biol.* 60(7):3013-29.

Zeng C, Plastaras JP, James P, Tochner ZA, Hill-Kayser CE, Hahn SM and Both S 2016 Proton pencil beam scanning for mediastinal lymphoma: treatment planning and robustness assessment. *Acta Oncol.* 55(9-10):1132-8.

Ziegenhein P, Pirner S, Kamerling CPH and Oelfke U 2015 Fast CPU-based Monte Carlo simulation for radiotherapy dose calculation. *Phys. Med. Biol.* 60(15):6097-111.

Publications

Journal articles

Guerreiro F, Burgos N, Dunlop A, Wong K, Petkar I, Nutting C, Harrington K, Bhide S, Newbold K, Dearnaley D, deSouza NM, Morgan VA, McClelland J, Nill S, Cardoso MJ, Ourselin S, Oelfke U and Knopf AC 2017 Evaluation of a multi-atlas CT synthesis approach for MRI-only radiotherapy treatment planning. *Phys. Med.* 35:7-17.

Guerreiro F, Seravalli E, Janssens GO, van de Ven CP, van den Heuvel-Eibrink MM and Raaymakers BW 2018 Intra- and inter-fraction uncertainties during IGRT for Wilms' tumor. *Acta Oncol.* 57(7):941-9.

Guerreiro F, Seravalli E, Janssens GO, van den Heuvel-Eibrink MM, Lagendijk JJW and Raaymakers BW 2019 Potential benefit of MRI-guided IMRT for flank irradiation in pediatric patients with Wilms' tumor. *Acta Oncol.* 58(2):243-50.

Guerreiro F, Koivula L, Seravalli E, Janssens GO, Maduro JH, Brouwer CL, Korevaar EW, Knopf AC, Korhonen J and Raaymakers BW 2019 Feasibility of MRI-only photon and proton dose calculations for pediatric patients with abdominal tumors. *Phys. Med. Biol.* 64(5):055010.

Guerreiro F, Zachiu C, Seravalli E, Oraboni Ribeiro C, Janssens GO, Ries M, Denis de Senneville B, Maduro JH, Brouwer CL, Korevaar EW, Knopf AC and Raaymakers BW 2019 Evaluating the benefit of PBS vs. VMAT dose distributions in terms of dosimetric sparing and robustness against inter-fraction anatomical changes for pediatric abdominal tumors. *Radiother. Oncol.* 138:158-65.

Conference proceedings

Guerreiro F, Janssens GO, Seravalli E and Raaymakers BW 2016 SU-F-J-63: Abdominal diameter changes in children during volumetric modulated arc therapy (VMAT): Is replanning needed? *58th AAPM Proceedings, Medical Physics* 43:3420.

Guerreiro F, Seravalli E, Jansses GO, Heuvel-Eibrink MM and Raaymakers BW 2017 PO-0873: Inter- and intra-fraction motion of the tumor bed and organs at risk during IGRT for Wilms' tumor. *Estro 36 Proceedings, Radiotherapy and Oncology* 123:476.

Guerreiro F, Seravalli E, Janssens GO, Maduro JH, Brouwer CL, Korevaar EW, Knopf AC and Raaymakers BW 2017 PTC17-0100: Dosimetric comparison of volumetric modulated arc therapy versus pencil beam scanning proton therapy for children treated for Wilms' tumor. *56th PTCOG Proceedings.*

Guerreiro F, Janssens GO, Seravalli E and Raaymakers BW 2017 SU-I-GPD-J-32: Inter- and intra-fraction motion uncertainties during IGRT for kidney tumor in pediatrics. *59th AAPM Proceedings.*

Guerreiro F, Janssens GO, Seravalli E, Lagendijk JJW and Raaymakers BW 2018 EP-1644: Potential gain of MRI-guided IMRT planning versus current clinical CBCT-guided VMAT for Wilms' tumor. *Estro 37 Proceedings, Radiotherapy and Oncology* 127:884-5.

Guerreiro F, Seravalli E, Janssens GO, Maduro JH, Brouwer CL, Korevaar EW, Knopf AC and Raaymakers BW 2018 EP-1645: Dosimetric comparison of VMAT and pencil beam scanning proton therapy for abdominal pediatric tumors. *Estro 37 Proceedings, Radiotherapy and Oncology* 127:885-6.

Koivula L, **Guerreiro F**, Raaymakers BW and Korhonen J 2018 EP-2086: Synthetic CT generation from standard T2-weighted MR image - lung, vertebrae, and liver targets. *Estro 37 Proceedings, Radiotherapy and Oncology* 127:1145-6.

Guerreiro F, Koivula L, Seravalli E, Janssens GO, Maduro JH, Brouwer CL, Korevaar EW, Knopf AC, Korhonen J and Raaymakers BW 2018 Feasibility of MRI-only photon and proton dose calculations for abdominal pediatric patients. *6th MR in RT Proceedings.*

Guerreiro F, Seravalli E, Janssens GO, Maduro JH, Brouwer CL, Korevaar EW, Knopf AC and Raaymakers BW 2018 TU-E115-GePD-F7-05: Potential dosimetric benefit of PBS-PT and MRI-guided IMRT compared to clinical VMAT used to treat children. *60th AAPM Proceedings.*

Guerreiro F, Koivula L, Seravalli E, Janssens GO, Maduro JH, Brouwer CL, Korevaar EW, Knopf AC, Korhonen J and Raaymakers BW 2018 TH-EF-KDBRB1-04: Feasibility of MRI-only photon and proton dose calculations for abdominal pediatric patients. *60th AAPM Proceedings.*

Guerreiro F, Seravalli E, Janssens GO, Maduro JH, Brouwer CL, Korevaar EW, Knopf AC and Raaymakers BW 2019 PO-0986: Inter-fraction anatomical changes in pediatric abdominal tumors during photon and proton therapy. *Estro 38 Proceedings, Radiotherapy and Oncology* 133:540-1.

Invited Talks

Guerreiro F, Koivula L, Seravalli E, Janssens GO, Maduro JH, Brouwer CL, Korevaar EW, Knopf AC, Korhonen J and Raaymakers BW MRI-only photon and proton RT using synthetic CT images for children: Dosimetric accuracy and planning strategies. TU-GH-207 AAPM-COG Joint Session, *60th AAPM Proceedings.*

Awards

Galileo Galilei Award in Medical Physics 2017. *Phys. Med.* 53(2018):153 with 'Evaluation of a multi-atlas CT synthesis approach for MRI-only radiotherapy treatment planning' *Phys. Med.* 35(2017):7-17.

Acknowledgements

I could have never done this PhD without the support and collaboration of many persons, to whom I am deeply grateful. Coming to the Netherlands to do a PhD was a great journey / adventure in my life and I am happy that you were all part of it.

I would like to thank first my promotor and always positive supervisor Bas Raaymakers. Thank you for all the discussions, "you can do it!" moments, "I do not have a lot of corrections" friendly faces and "if protons are better you should state that" encouragements. It was a pleasure to work with you as even during more difficult times you always had a smile and a wise advice to give! Also, my gratitude goes out to my daily supervisor and co-promotor Enrica Seravalli for always guiding me from a close and personal point of view. Thank you for our regular meetings, for the countless quick revisions to all my papers, abstracts and presentations and especially for being always available to help me with any matter. Bas and Enrica, I really appreciated the time we spent together during these last four years, I could not ask for a better supervision. You both gave me a lot of confidence in my research and also in myself. So a big thanks goes to you both!

I also would like to acknowledge my second co-promotor Geert Janssens. Thank you for all the clinical knowledge you gave me and for all the extensive discussions which were very fruitful for the development of this thesis.

Finishing this thesis would have not been possible without the collaboration and support of the University Medical Center Groningen (UMCG) and everybody working at Terracota, in particular Antje Knopf, Erik Korevaar, Charlotte Brouwer and John Maduro. Thank you for receiving me so well during my internship at the UMCG and for all the positive feedback and discussions during these last years. I am really glad that we were able to collaborate on these projects and I hope we can still work together in the future. A special thanks goes to Antje Knopf. You were my supervisor during my master thesis and I am so happy that we could continue working together also for my PhD. You are the reason that I decided to do a PhD after such a positive experience in research with you. So thank you very much for all your kindness and support throughout these years, from London to the Netherlands.

Also I would like to thank all my co-authors for all the help and feedback during the development of these manuscripts. A special thanks goes to Lauri Koivula and Juha Korhonen which kindly made a useful research collaboration with us. Thank you Lauri for all your availability to discuss things related to the sCT project even during conferences barbecues! I would also like to thank Cornel Zachiu, Baudouin Senneville and Mario Ries for letting me use Evolution. Thank you Cornel for all the time spent in registering my nightmare quality CBCTs.

I would like to express my sincere gratitude to the thesis assessment committee members for the evaluation of this thesis: Prof.dr. Marc Wijnen, Prof.dr. Pim de Jong, Prof.dr. Mischa Hoogeman, Prof.dr. Stefan Both and Dr. Max van Noesel.

A big thanks goes to the fellow past, present and future PhD students, PostDocs and 'something'- experts that in one way or another made these last four years really pleasant: Anna, Bjorn, Charis, Christopher, Cornel, Daan, Dennis, Ellis, Federico, Hans, Jean-Paul, Joris, Jorine, Laura, Maarten, Mark, Markus, Matteo, Maureen, Maxence, Mick, Michaela, Mike, Osman, Pim, Robin (thank you for all the kickboxing and pump hours), Sanam, Simon, Sophie, Soraya, Stefan, Stefano, Tim, Tom, Tristan, Yulia and possibly others that I am forgetting. Thank you for all the OIO uitjes, coffee breaks, dinners, night outs, conferences and runs. I had a lot of fun!

For all the help provided to finish this book, I would especially like to say thanks to Charis, Pim and Stefan. Charis, the most amazing line dancer that I know, thank you for all the help you gave with the LaTeXtemplate (even when you knew that it was not going to be short). Pim, the Dr. one day earlier than me, thank you for translating my summary and also thank you for all the coffee breaks stressing about not having yet a committee, a cover, a party location etc. It was fun! Finally, Stefan thank you for creating the most useful script and for letting me use it to convert all my endless word files into LaTeXcode.

A special thanks goes to the ladies in our room in Q2: Anna, Ellis and Maureen. Thank you for being such good roommates and for all the time spent talking about being eaten by bears, the Dutch royal family, yellow and green shoes, amazing holidays and 'how much is raining right now' instead of working! Your company, our coffee breaks and mostly your support made the office such a nice environment to work.

A huge thanks goes to all my Portuguese friends that were as crazy as me to come to the Netherlands (the country where the weather is total madness) to do a master and / or PhD: Joana Carvalho (Jo), Cássia, Iva (Binha), João (Guimas), Joana Boita, Francisco, Bruno (o meu excelente fotógrafo, obrigada por este mega favor), Inês, Iara, Zé Nuno and André. You guys always made me feel a bit less homesick. Obrigada por todas as festas de aniversário, jantares, barbecues, concertos, cafés, copos e weekend getaways. Muito boa sorte com os vossos PhDs! Espero poder estar cá para vos ver a todos serem awesome Drs. Um obrigado especial vai para a Cássia por teres tido a paciência para ouvir os meus "proton stresses" e pela ajuda que me deste no meu último paper. Espero irmos juntas a muitas PTCOG's no futuro. Outro big thanks vai para o talentoso Francisco Fernandes que aceitou o desafio de desenhar a capa desta tese (e mudá-la vezes sem conta). De tão fantástica que ficou prometo que não gozo mais contigo na vida!! Sem dúvida que devias apostar mais nesse talento!

Outro agradecimento vai para os meus amigos em Portugal ou a fazer PhDs noutros cantos do mundo que sempre me fizeram sentir bem-vinda ao voltar a casa ou como se nada tivesse mudado. Por todos os jantares de natal, lanchinhos e jantarinhos, PDAs, brunchs, rooftop drinks, mensagens de whatsapp e telefonemas de aniversário, um grande obrigada em especial vai para: Tatiana (Tati), Sara Ferreira, Sara Silveira (das quais eu gosto muito de igual maneira, sim?), Francisco (Chico), Célia, Marciano (Marci Papi), Liane, Carlos e Filipa (a famosa Filipa 2, fico à espera de uma próxima Estro ou AAPM para mais momentos de stress e diversão) .

Another huge thanks goes to my two paranymphs: Joana Boita and Markus Glitzner. Boitinha do meu coração, fico mesmo contente que tenhas aceite o convite. Escolheste-me para ser tua madrinha na faculdade, escolho-te eu agora para esta tarefa. Em recompensa, prometo ir mais vezes à terrinha ter contigo!! Espero que saibas que és one of a kind e que eu gosto muito de ti mesmo quando és 100% "esquecida". Markus I am so happy that you could be here for my defense. I know you're dying because you left your cats for a second but I hope in the end it will be worth it! Thank you for all the nice concerts, swims, runs (yes even the ones you convinced me to do and in the end you quit), lasertag and party's in the last few years. I hope you find another colleague that tells you to shut up at every second. Just in case: shut up, shut up, shut up, shut up! I hope this is enough for now.

Quero também agradecer ao the most patient guy on earth - João. Obrigada por teres embarcado comigo nesta aventura, nunca conseguiria tê-la feito sem ti. Obrigada por toda a paciência a ouvir as minhas reclamações diárias (vá bi- ou tri-diárias) e mesmo sendo um homem de poucas palavras (ahah tinhas de ouvir esta) sei que estás lá sempre mas sempre para mim! Foste e continuas a ser a minha grande companhia! Um grande obrigado pelo apoio incondicional! Não vou dizer que és o Mr. perfect (que é só suuuper bimbo e lamechas) mas digo que gosto muito de ti e que estou ansiosa pelo que estará para vir (Humm, Disney?, ainda fomos tão poucas vezes).

Um grande agradecimento vai também para a minha incrível família, mãe, pai, irmãos, avós, tios, tias e primos. Sair de Portugal e não ter a vossa companhia diária foi sem dúvida o mais difícil que tive de fazer. Eternos "putos" da família, meus manos, obrigada por todos os momentos de brincadeira, espero que tudo vos corra bem no futuro (tudo menos o vosso benfica continuar a ganhar campionatos, era uma chatice!). Pai e mãe obrigada por todo o apoio, ajuda e carinho, vocês são fantásticos! Quando é que é a próxima family trip? Mãe a ti dou-te um beijinho especial porque apesar de seres a Miss mummy galinha sei que estás lá sempre para mim, não podia ter uma mãe melhor! Obrigada por tudo!

Por fim, um agradecimento especial vai para os meus avós Careca e Bábá (que estarão sempre presentes comigo em pensamento) aos quais dedico esta tese. O vosso carinho incondicional fez de mim a pessoa que sou hoje e só posso agradecer por tudo, pela educação, pelo carinho, pelas brincadeiras, por todos os abraços e beijinhos. É com a maior tristeza que sei que não vão poder estar cá para ler esta dedicatória mas espero que saibam que gosto e gostarei sempre sempre muito dos dois. Sinto tanto a vossa falta, mas sei que apesar de terem partido isto não é um adeus é um até já. Avô, vai tudo correr bem, prometo carequinha!
Muito obrigada Mãe 2 ☆! Muito obrigada Pai 2 ☆! Vocês foram e são o melhor que a vida me deu!

Filipa

In memoriam

Maria Manuela de Moura Rodrigues Borges Ferreira
21 June 1929 - 09 August 2016

Adolfo Botelho Borges Ferreira
18 January 1923 - 28 September 2019

Curriculum Vitae

Filipa Guerreiro was born in June 23, 1992 in Lisbon, Portugal. After receiving her high school diploma from the Escola Secundária do Restelo, Lisbon, Portugal in 2010, she started the bachelor and master program in Biomedical Engineering and Biophysics at the University of Lisbon, Portugal. As part of her bachelor education, she carried out during 3 months her graduation research project entitle 'Modeling doses of secondary particles from a proton beam with Geant4' at University College London (UCL), London, UK, under the supervision of Prof.dr. Adam Gibson and Prof.dr. Luis Peralta. She obtained her master's degree with specialization in Radiation Therapy in 2015. For her master graduation, she performed a project entitled 'Calibration of MR images for accurate dose calculations' during 7 months at the Institute of Cancer Research (ICR), London, UK, under the supervision of Prof.dr. Uwe Oelfke and Dr. Antje Knopf. In the same year, she started her PhD research project at the radiotherapy department of the University Medical Center Utrecht (UMCU), The Netherlands, under the supervision of Prof.dr. Bas Raaymakers and Dr. Enrica Seravalli. This thesis presents the work developed during 4 years on her research project focused on MRI-guided radiotherapy techniques to treat pediatric patients with abdominal cancer. Currently, Filipa is continuing her research as a postdoctoral researcher at the radiotherapy deparment of UMCU.